universität
wien

DISSERTATION / DOCTORAL THESIS

Titel der Dissertation / Title of the Doctoral Thesis

Understanding 2D Materials with 4D Scanning Transmission Electron Microscopy

verfasst von / submitted by

Giacomo Argentero

angestrebter akademischer Grad / in partial fulfillment of the requirements for the degree of

Doktor der Naturwissenschaften (Dr. rer. nat.)

Wien, 2017

Studienkennzahl lt. Studienblatt / degree programme code as it appears on the student record sheet:	A 796 605 411
Dissertationsgebiet lt. Studienblatt / field of study as it appears on the student record sheet:	Physik
Betreut von / Supervisor:	Univ.-Prof. Dipl.-Phys. Dr. Jannik C. Meyer

Zusammenfassung

Zehn Jahre nach der Entdeckung von Graphen ist die wissenschaftliche Forschung auf dem Gebiet der zweidimensionalen (2D)-Materialien aktiver denn je. Die enorme Begeisterung, welche die ersten experimentellen Studien über Graphen angefacht haben, hat sich nun auf viele andere Schichtkristalle mit einzigartigen Eigenschaften ausgeweitet. Da sie nur wenige Atomlagen dünn sind, können 2D-Materialien einfach durch Transmissionselektronenmikroskopie (TEM) untersucht werden. Diese Technik ist zu einer der leistungsstärksten und weitverbreitetsten in diesem Forschungsgebiet geworden. Die im Ångstrom-Bereich liegende Auflösung der modernen TEMs erlaubt die Charakterisierung von 2D-Materialien auf atomarer Skala. Dies ermöglicht ein tiefes Verständnis ihrer strukturellen Eigenschaften.

In dieser Arbeit erforsche ich die Möglichkeiten von Rastertransmissionselektronenmikroskopie (STEM), jenseits der traditionellen Bildgebung, mit Hilfe eines vierdimensionalen (4D)-Mikroskopie-Ansatzes. Hierbei wird die Intensität des gestreuten Elektronenstrahls auf einem 2D Detektor an jedem Punkt des gescannten 2D Bildes aufgezeichnet. Diese Technik wird verwendet, um Informationen aus 2D-Materialien zu gewinnen, die durch konventionelle Bildgebung nicht zugänglich sind. Insbesondere charakterisiere ich die dreidimensionale Atomstruktur eines van der Waals-Kristalls, bestehend aus einer freistehenden Doppelschicht aus Graphen und Bornitrid. Dabei zeige ich, dass die Heterostruktur in der Richtung außerhalb der Ebene aufgrund einer periodischen Modulation der Wechselwirkungsstärke zwischen den beiden Schichten verzerrt ist. Weiters diskutiere ich die Möglichkeit, die Kohlenstoff-Isotope ^{12}C und ^{13}C in einer ^{13}C-angereicherten Graphenprobe auf atomarer Skala zu identifizieren. Für diese Arbeit habe ich den Energieverlust für in große Winkel gestreute Elektronen für beide Isotope simuliert. Hierbei zeige ich, dass ein kleiner Unterschied im Signal eine eindeutige Identifikation der Isotope erlauben sollte. Darüber hinaus zeige ich die ersten experimentellen Schritte in diese Richtung. Ebenfalls erforsche ich einen weiteren Ansatz zur Unterscheidung verschiedener Isotope: strahlinduzierter “knock-on damage” wird für Graphenproben bestehend aus ^{12}C- oder ^{13}C-Atomen quantifiziert. Dieser kann dann zur Bestimmung der lokalen Isotopenkonzentration in einer gemischten Probe verwendet werden.

Abschließend zeigt diese Arbeit, wie neue Detektionsgeometrien und unkonventionelle Techniken im STEM erfolgreich zur Forschung an 2D-Materialien beitragen können.

Abstract

One decade after the discovery of graphene, scientific research on two-dimensional (2D) materials is far from being exhausted. The enthusiasm that accompanied the first experimental studies on graphene, has now spread to many other layered crystals, which show unique properties. Because of their inherent atomic thickness, 2D materials can be conveniently studied by transmission electron microscopy (TEM), which has become one of the most powerful and widely employed tools in this field of research. The Ångstrom-level resolution of modern TEMs allows the characterization of 2D materials on the atomic scale, enabling profound understanding of their structural properties.

In this thesis, I explore the possibilities of scanning transmission electron microscopy (STEM) beyond traditional imaging based on a four-dimensional (4D) microscopy approach in which the intensity of the scattered electron beam is recorded on a 2D detector at each point of the 2D scanned image. This technique is employed to extract information from 2D materials that could not be accessed by conventional imaging. In particular, I study the three-dimensional atomic structure of a van der Waals crystal consisting of a suspended bilayer of graphene and hexagonal boron nitride, showing that this heterostructure distorts in the out-of-plane direction due to a periodical modulation of the interaction strength between the two layers. Next, I discuss theoretically the possibility of identifying ^{12}C and ^{13}C carbon isotopes on the atomic scale in a ^{13}C-enriched graphene sample. For this work, I simulated the energy loss of electrons elastically scattered to high angles for both isotopes, showing that a tiny difference in the signal should indeed allow unambiguous isotope identification, and I show the first experimental steps in this direction. Finally, I explore a different approach for discerning between isotopes: beam induced knock-on damage is quantified for graphene samples consisting of either ^{12}C or ^{13}C atoms, and it is then employed for probing the local isotope concentration in a mixed sample.

In conclusion, this work shows how new detection geometries and unconventional techniques in the STEM can successfully contribute to the research on 2D materials.

Ringraziamenti

Innanzitutto vorrei esprimere la mia profonda gratitudine al mio relatore e direttore del gruppo di ricerca “Physics of Nanostructured Materials”, il prof. Jannik C. Meyer. Il suo costante sostegno e la sua attenta supervisione mi hanno guidato con successo durante tutto il corso del dottorato, permettendomi con generositá di presentare la mia ricerca in occasione di varie conferenze internazionali. Il suo entusiasmo e la sua competenza straordinaria nel campo della microscopia elettronica sono stati per me molto stimolanti e incoraggianti, aiutandomi anche a superare momenti di grossa frustrazione dopo alcune notti infruttuose passate al microscopio. Vorrei anche ringraziare il prof. Jani Kotakoski, il cui input e i cui pareri esperti sono stati di grandissima importanza. Grazie a lui non ho soltanto ampliato le mie conoscenze nell’ambito della fisica, ma ho migliorato molto le mie abilità nella programmazione al computer e nella scrittura scientifica. Sono inoltre molto grato al dott. Clemens Mangler per il suo costante impegno volto ad assicurare performance ottimali dello STEM, per avermi aiutato a risolvere i tanti problemi quotidiani durante gli esperimenti e per avermi introdotto al mondo magico di Linux. Vorrei anche ringraziare la dott.ssa Viera Skakalova con la quale, in varie occasioni, ho piacevolmente discusso di scienza al di là della microscopia elettronica e con cui ho sviluppato un profondo rapporto di amicizia. Inoltre, desidero ringraziare i miei due “compagni di dottorato” più vicini, Franz Eder e Andreas Mittelberger, che negli anni sono diventati molto di più che semplici colleghi. Senza di voi il mio dottorato non sarebbe stato lo stesso. Un ringraziamento speciale va a tutti gli altri membri del gruppo: dott. Bernhard Bayer, dott. Christian Kramberger, dott. Kimmo Mustonen, dott. Mohammad Monazam, dott. Timothy Pennycook, dott. Toma Susi, Kenan Elibol, Christoph Hofer, Stefan Hummel, Ursula Ludacka, Rasim Mirzayev e Mukesh Tripathi. Vorrei esprimere il mio apprezzamento per tutti gli altri miei più stretti collaboratori, in particolare per i Prof.ri Christian Retenberger e Thomas Waitz, e per Filippo Fedi, Christian Ebner e Andreas Berger. Desidero anche ringraziare Regina Pinter per le sue inestimabili doti nell’adempiere le tante faccende amministrative e per la sua grande gentilezza. Ringrazio tutti i membri della Vienna Doctoral School, inclusi tutti i dottorandi, i professori e gli organizzatori. Ho davvero apprezzato i momenti passati insieme durante i tanti incontri, sia quelli scientifici che quelli molto poco scientifici. Il completamento del mio dottorato non sarebbe mai stato possibile senza l’appoggio di alcune persone molto speciali al di fuori della mia vita professionale. Sono profondamente grato a mia madre Francesca, a mio padre Oscar e a mia sorella Margherita, che mi hanno sempre sostenuto silenziosamente e che non hanno mai messo in discussione le mie scelte di vita, nonostante queste mi abbiano portato lontano da loro per molto tempo. Vi ringrazio tanto per questo. Infine, e soprattutto, voglio ringraziare la mia amata Elisabeth. Il suo sostegno, la sua fiducia in me e il suo amore sono stati la vera energia che mi ha spinto serenamente attraverso questi anni, e che ha contribuito a rendere questo periodo della mia vita un’esperienza così fantastica. Siamo una squadra formidabile!

Acknowledgements

First of all, I would like to express my deep gratitude to my Ph.D. supervisor and head of the “Physics of Nanostructured Materials” group, Prof. Jannik C. Meyer. His constant support and attentive supervision successfully guided me throughout the course of my Ph.D., generously allowing me to present my research at various international conferences. His enthusiasm and outstanding expertise in the field of electron microscopy have been really motivating and encouraging, also helping to overcome frustration after the unsuccessful nights spent at the microscope. I would also like to thank Prof. Jani Kotakoski, whose input to my research and expert advice have been invaluable and inspiring. Thanks to him I did not only broaden my scientific knowledge but I also improved other skills, including programming and academic writing. I am indebted to Dr. Clemens Mangler for his continuous dedication to ensure optimal performance of the STEM machine, for helping to solve every-day problems in the experiments and for introducing me to the magic world of Linux I also would like to thank Dr. Viera Skakalova, with whom I often enjoyed interesting scientific discussion beyond electron microscopy and who always had a friendly word for me. Furthermore, I would like to thank my former and my current closest Ph.D. mates, Franz Eder and Andreas Mittelberger, who became in the years much more than simple colleagues. Without you my Ph.D. experience would not have been the same. A special thanks goes to all other members of the group: Dr. Bernhard Bayer, Dr. Christian Kramberger, Dr. Kimmo Mustonen, Dr. Mohammad Monazam, Dr. Timothy Pennycook, Dr. Toma Susi, Kenan Elibol, Christoph Hofer, Stefan Hummel, Ursula Ludacka, Rasim Mirzayev and Mukesh Tripathi. I would like to express my appreciation to all other close colleagues, in particular Prof. Christian Retenberger, Prof. Thomas Waitz, Filippo Fedi, Christian Ebner and Andreas Berger. I would like to thank Mrs. Regina Pinter for her invaluable administrative skills and friendliness. I acknowledge all members of the Vienna Doctoral School, including all students, professors and the organizing team. I really enjoyed the time spent with all of you during the many scientific and not-so-scientific events. The completion of my Ph.D. would have never been possible without the support of very special people from outside my professional life. I am deeply grateful to my mother Francesca, to my father Oscar and to my sister Margherita, who silently supported me and never questioned the importance of my life choices, although they brought me away from them for a long time. Thank you for this. Finally, and most importantly, I would like to thank my beloved Elisabeth, who became my wife halfway through my Ph.D. Her support, trust and love have been the real resources which happily pushed me through these years, and which contributed to make this period of my life such an amazing time. We are the best team ever!

Contents

List of acronyms

2D	two-dimensional	1
3D	three-dimensional	1
4D	four-dimensional	33
a-C	amorphous carbon	97
ACOM	annular center of mass	34
ADF	annular dark field	15
AFM	atomic force microscopy	45
BF	bright field	13
CBED	convergent beam electron diffraction	33
C_c	chromatic aberrations	12
CCD	charge-coupled device	37
CFEG	cold field emission gun	15
C_s	spherical aberrations	12
CVD	chemical vapor deposition	19
DF	dark field	10
DFT	density functional theory	53
EACS	electron-atom Compton scattering	62
EDX	energy-dispersive X-ray	13
EELS	electron energy loss spectroscopy	10
FOV	field of view	79
FT	Fourier transform	16
HAADF	high angle annular dark field	15
hBN	hexagonal boron nitride	2
HRTEM	high-resolution transmission electron microscope	86
IPA	isopropyl alcohol	27
MAADF	medium angle annular dark field	15
PADF	pixelated annular dark field	33
PMMA	Poly(methyl 2-methylpropenoate)	29
QF	Quantifoil®	27
rms	root mean square	65
SEM	scanning electron microscopy	29
STEM	scanning transmission electron microscopy	6

STM	scanning tunneling microscopy	1
TEM	transmission electron microscopy	6
TMDC	transition metal dichalcogenides	2
UHV	ultra-high vacuum	15
vdW	van der Waals	2
ZLP	zero-loss peak	73

Chapter 1

Introduction

1.1 2D materials

The world we live in is three-dimensional (3D). All objects surrounding us that we can see and touch have a width, a height and a depth. Even the pages of this thesis, which appear to have only two dimensions, have a measurable thickness which makes them just as 3D as everything else. One might then wonder about the existence of two-dimensional (2D) objects. Matter as we know it consists of objects that have a volume and occupy the 3D space. Therefore, from a strict, mathematical point of view, 2D materials cannot exist. From a less strict, physical perspective, a 2D object can be imagined as a material where the third dimension is reduced to the smallest stable constituent of matter: the atom. Scientists have speculated for a long time about the existence of atomically thin materials and 80 years ago they concluded that strictly 2D materials could not exist because of thermodynamical reasons [1–3]. This was commonly accepted until one Friday night in 2003. On that occasion, during a session of the "Friday Night Experiments"[1], the two physicists André Geim and Konstantin Novoselov were attempting to produce thin carbon films by peeling off a few layers of material from a graphite crystal using the common Scotch tape. Mechanical cleavage of crystals by Scotch tape was not new: this technique was routinely used to produce cleaner and flatter graphite samples to be imaged by scanning tunneling microscopy (STM) and the used tape was then discarded. Geim and Novoselov "simply picked it up from the trash bin and used it" [5]. After several attempts they were able to isolate graphene, a single atomic layer of graphite: 2D materials were proven to exist. Graphene immediately appeared to be an extraordinary material: an electrically conductive, atomically thin layer of carbon atoms arranged in an hexagonal lattice. They then submitted a paper summarizing their findings

---

[1] Throughout his career, Geim has devoted about 10% of his lab time to work on "crazy things that probably won't pan out at all, but if they do, it would be really surprising" [4]. This parallel, unfunded research evolved into what he calls the "Friday Night Experiments".

to *Nature* which rejected it twice before it was finally accepted in *Science* [6]. According to one of the referees their work did “not constitute a sufficient scientific advance” [7]. Six years later, in 2010, Geim and Novoselov were awarded the Nobel Prize in Physics “for groundbreaking experiments regarding the two-dimensional material graphene” [8].

Since its discovery, graphene has attracted enormous scientific interest because of its unique properties (see section 1.1.1) and within a few years hundreds of groups around the world had started research on this novel material in a number of different fields. Shortly after, scientists already showed experimentally that other 2D crystals can exist [9]. In graphite, the atoms in each layer are strongly bound by in-plane covalent bonds, while the out-of-plane interlayer interaction is due to weak van der Waals (vdW) forces. In fact, this was the primary reason why graphene could be so easily produced from its layered bulk counterpart. The “Scotch tape method” proved to be very useful as researchers started to employ it for the exfoliation of other layered crystals. In the last decade, the family of 2D materials has been constantly growing and now includes a large number of members, many of which are chemically stable under ambient conditions. The most famous “sibling” of graphene is hexagonal boron nitride (hBN). hBN is a binary compound that features a hexagonal atomic structure similar to the one of graphene (where alternating B and N atoms replace C atoms) and almost identical lattice constant but, unlike graphene, it is an insulator. Besides graphene and hBN, a rich contribution to the 2D family is represented by the group of transition metal dichalcogenides (TMDC). These materials are of the type MX_2, where M is a transition metal atom (Mo, W, ...) and X is a chalcogen atom (S, Se or Te). Similar to graphene and hBN, the top view atomic structure of TMDC is hexagonal. However, the metal atoms are sandwiched between two layers of chalcogen atoms. Interestingly, many of the TMDC monolayers are direct gap semiconductors and can therefore find applications as light emitters or detectors in optoelectronics. “Heavier” analogues of graphene have also been explored and experimental evidence of the existence of monolayers of silicon (silicene [10]), germanium (germanene [11]) and black phosphorus (phosphorene [12]) have been reported. Other classes of 2D materials include the so-called MXenes (layered transition metal carbides and nitrides), layered oxides and perovskite-like crystals [13]. In conclusion, graphene turned out to be only the tip of a submerged iceberg, the most accessible example within the broad class of 2D materials. Currently, the search for novel 2D materials is far from being completed and the isolation and characterization of atomically thin materials is keeping many research groups busy all around the world.

1.1.1 Graphene

At the time of writing, graphene has just celebrated its thirteenth birthday. During these few years, graphene has traveled a long journey, from being a completely new, unexplored material to the point where much of the rich physics behind it has been extensively studied and understood. Nevertheless, graphene continues to attract enormous attention because of its unique properties that stimulate both fundamental research and development of technological applications. In this section I will introduce this material and give an overview of its most relevant physical properties.

Graphene is an atomically thin 2D crystal of carbon atoms arranged in a honeycomb-like lattice. As Geim put it himself: "graphene is a single atomic plane of graphite, which – and this is essential – is sufficiently isolated from its environment to be considered free-standing" [14]. The atomic structure of graphene is presented in fig. 1.1a, where the two sublattices are marked by red and blue circles. The lattice constant a is 2.46 Å. The primitive lattice vectors are

$$\vec{a}_1 = \frac{3d}{2}\left(\hat{x} + \frac{1}{\sqrt{3}}\hat{y}\right); \qquad \vec{a}_2 = \frac{3d}{2}\left(\hat{x} - \frac{1}{\sqrt{3}}\hat{y}\right)$$

where $d = 1.42$ Å is the interatomic distance and $\hat{x}$ and $\hat{y}$ are the unit vectors of the reference system as drawn in fig. 1.1a. The unit cell is highlighted in yellow and contains two atoms. The primitive vectors of the reciprocal space are shown in fig. 1.1b and are written as

$$\vec{b}_1 = \frac{2\pi}{3d}\left(\hat{k_x} + \sqrt{3}\hat{k_y}\right); \qquad \vec{b}_2 = \frac{2\pi}{3d}\left(\hat{k_x} - \sqrt{3}\hat{k_y}\right)$$

The first Brillouin zone is also hexagonal and it is rotated by 30° with respect to the lattice orientation. Each carbon atom has six electrons, two of which are arranged in the inner $1s$ orbital and four in the outer shell. The outer four electrons are, in turn, arranged in the $2s$ and $2p$ orbitals and are available for chemical bonding. However, since each C atom has only three nearest neighbors in graphene, the orbitals with principal quantum number 2 combine to form three sp^2 hybrid orbitals and leave one electron in a $2p$ orbital. The three sp^2 orbitals are separated by 120° and lay on a plane. They are used to make covalent bonds with the neighbors, while the remaining $2p$ orbital extends in the third dimension orthogonal to the plane (for this reason it is often referred to as the $2p_z$ orbital). The electronic band structure of graphene was first derived by Wallace based on a tight-binding approach [15] (see also review by C. Neto et al. [16]). The energy bands have the form

$$E_\pm(\mathbf{k}) = \pm t\sqrt{3 + f(\mathbf{k})} - t' f(\mathbf{k}),$$

$$f(\mathbf{k}) = 2\cos\left(\sqrt{3}k_y d\right) + 4\cos\left(\frac{\sqrt{3}}{2}k_y d\right)\cos\left(\frac{3}{2}k_x d\right), \tag{1.1}$$

where t and t' are the nearest-neighbor and next nearest-neighbor hopping energies, respectively. The plus sign in equation 1.1 applies to the upper

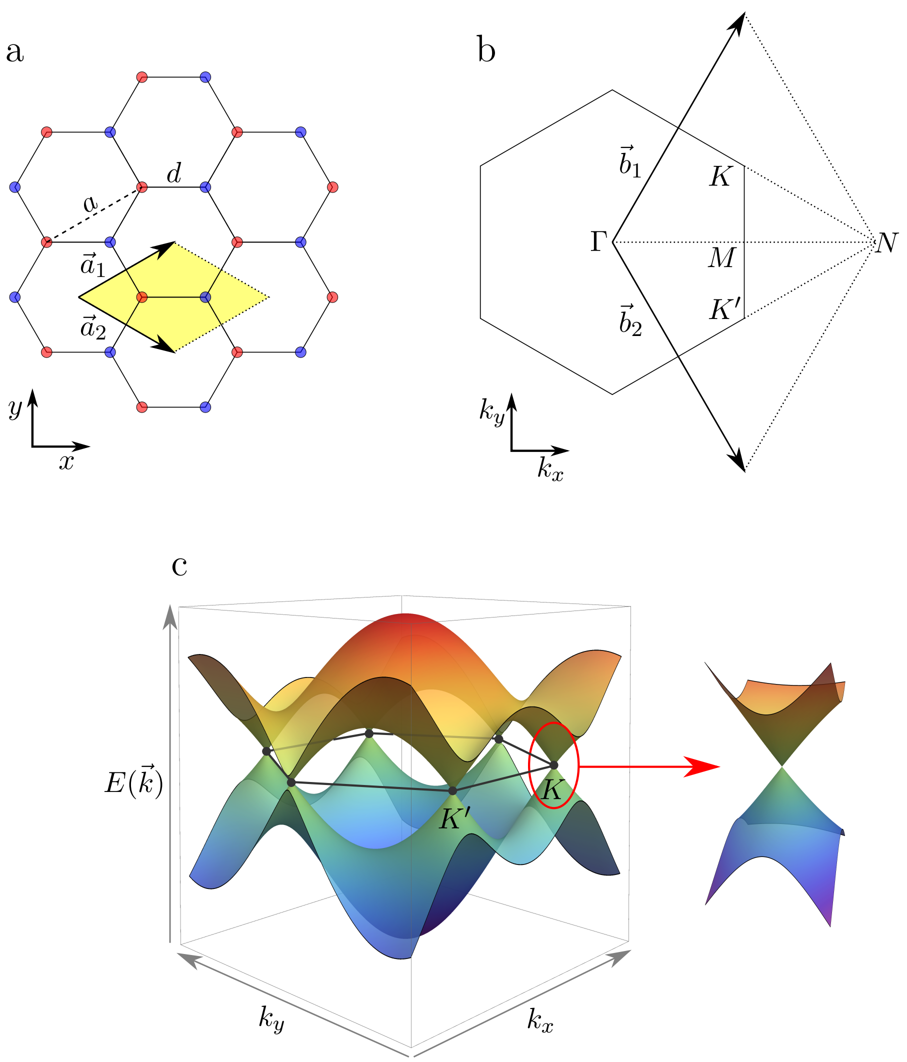

Figure 1.1: (a) The atomic structure of graphene: the red and the blue dots represent the two inequivalent lattice positions. The unit cell, identified by the primitive vectors $\vec{a}_1$ and $\vec{a}_2$, is highlighted in yellow. The lattice constant a is 2.46 Å. The interatomic distance d is 1.42 Å. (b) The first Brillouin zone of the graphene lattice. The K and the K' points are also called Dirac points. (c) The electronic band structure of graphene. The dispersion relation is linear in the vicinity of the Dirac points.

conduction band (π) and the minus sign to the lower valence band (π^*). The band structure, plotted using the equations above, is shown in fig. 1.1c. The valence and the conductance bands touch without overlap at the edges of the Brillouin zone, that is, at the K (or K') points. Importantly, the Fermi-level is exactly where the bands touch. For this reason, graphene is often referred to as a zero-gap semiconductor.

In the vicinity of the K points, also called Dirac points, the dispersion relation is linear, unlike most other materials that have a parabolic dispersion. This peculiar band structure has very important implications on the electronic properties of graphene. In the vicinity of the Dirac point the energy dispersion can be approximated as [16]

$$E_{\pm}(\mathbf{q}) \approx \pm v_f |\mathbf{q}| \tag{1.2}$$

where $\mathbf{q}$ is the wave vector relative to the Dirac point and v_f is the Fermi velocity ($v_f \sim 10^6\,\mathrm{m\,s^{-1}}$ for graphene). This expression resembles the characteristic energy dispersion for massless relativistic particles as photons. For these particles the relativistic relation

$$E^2 = (pc)^2 + (m_0 c^2)^2$$

simplifies to

$$E = pc = \hbar k c$$

in strong analogy with eq. 1.2, where the Fermi velocity replaces the speed of light. Because of this striking similarity, electrons in graphene are often referred to as “massless” particles and their behavior can be described by the relativistic Dirac equation (hence the name Dirac point).

Charge transport in graphene relies on the electrons in the $2p_z$ orbitals that are highly delocalized and form the π molecular orbital. Electron mobility in graphene has been measured to be as high as $200\,000\,\mathrm{cm\,V^{-1}\,s^{-1}}$ in suspended graphene at $\sim 5\,\mathrm{K}$ [17] and $15\,000\,\mathrm{cm\,V^{-1}\,s^{-1}}$ for supported graphene at room temperature [18]. The record electron mobility makes graphene the best known conductor at room temperature, with a conductivity that is almost twice that of copper.

The extraordinary properties of graphene are not limited to its peculiar electrical features. Its thermal conductivity is $\sim 5000\,\mathrm{W\,m^{-1}\,K^{-1}}$ [19], about 10–20 times larger than the best thermally conductive metals. Concerning mechanical properties, graphene’s tensile strength is the largest known, corresponding to a Young’s modulus of $\sim 1\,\mathrm{TPa}$ [20], about 100 times larger than steel. Despite being so strong, graphene is only one atom thick and it is extremely flexible. Also, graphene is impermeable to both liquids and gases.

Other interesting properties and peculiar phenomena related to graphene are beyond the scope of this thesis and will not be discussed here. However, this brief overview should suffice in explaining the enormous scientific interest that this material has attracted (and still attracts) since its discovery.

1.1.2 Van der Waals heterostructures

So much has been said and written on graphene that André Geim, the "father" of graphene, stated in 2013 that "it is probably fair to say that research on 'simple graphene' has already passed its zenith" [13]. A few years after the experimental discovery of graphene, a new, exciting perspective started to take shape. Researchers realized that because of their large exposed surface, several individual monolayers of various 2D materials could be stacked on top of each other to produce stable crystals held together by van der Waals (vdW) forces [13]. These artificial crystals, commonly known as vdW heterostructures, can be fairly easily prepared in laboratories to produce potentially infinite combinations of elementary 2D building blocks. Each of these unique vdW heterostructures will then display specific properties based on the characteristics of the parent 2D crystals and on the interplay between them. Ideally, one would then be able to design a system with desired properties to target a certain application. To clarify this concept, consider the example of ref. [21]: in this work, WSe_2 and graphene were stacked on top of each other to build an ultrafast and efficient photodetector. The key idea here was to combine a direct band gap semiconductor for light detection (WSe_2) with an excellent conductor for fast charge collection (graphene). Either of these two materials taken alone would have failed to serve the desired purpose.

To date, complex vdW systems have been proposed and realized, and vdW heterostructures are emerging as one of the most active fields of research in the 2D materials community.

1.2 Motivation and outline

Through the last decade, transmission electron microscopy (TEM) and scanning transmission electron microscopy (STEM) have established themselves as unmatchable tools for the study of 2D materials [22–25]. The first TEM study on suspended graphene appeared shortly after the material was discovered [26] and since then the scientific throughput of TEM research on 2D materials has been growing enormously. There are several reasons why TEM and 2D materials constitute a perfect match. First of all, because of the intrinsic atomic thickness of these crystals, no complicated sample preparation is needed to allow the required transmission of electrons, making 2D materials the "perfect" samples for TEM. As a second fortunate coincidence, when graphene was isolated for the first time, electron microscopes just began to have enough spatial resolution to image this crystal at atomic resolution and at energies low enough to prevent radiation damage. As a result, microscopists were for the first time able to image individual light atoms within the 2D crystal lattice, rather than atomic columns. Furthermore, the capability of TEMs to record rapid consecutive images enabled the study of time-resolved structural modifications on the atomic scale.

After ten years of continuous effort from the scientific community, it is becoming increasingly difficult to extract new information from these crystals by “standard” TEM techniques. The goal of this thesis is to explore both theoretically and experimentally novel detection methods in the STEM to gain insights into structural properties of 2D materials that could not be accessed otherwise. In particular, I will show how I was able to precisely determine the 3D atomic structure of a suspended vdW heterostructure consisting of a bilayer of graphene and hBN. I demonstrate that the heterostructure is far from being atomically flat, exhibiting in fact a strong out-of-plane distortion that arises from vdW forces acting between the two layers, and which is therefore an intrinsic property of the material. Another part of my thesis is devoted to the local detection of the isotopic composition of a graphene sample consisting of a mixture of ^{12}C and ^{13}C atoms. To this end, two different approaches are followed, trying to differentiate the two isotopes by either electron-atom energy transfer in Rutherford scattering or by knock-on damage. The results included in this thesis show how TEM and STEM are invaluable tools for the study of 2D materials, especially if combined with some “out-of-the-box” thinking and new detection schemes. With electron microscopes’ performances constantly improving and various new 2D crystals being isolated every year, TEM research on 2D materials is expected to remain in the spotlight for many years to come.

Chapter 2

Experimental

In this chapter I will introduce the experimental methods that were used for my research. A substantial part of the chapter will be devoted to electron microscopy, the most extensively employed investigation tool in this thesis. After a brief general introduction, the specific microscopes that were used for the experiments are described. Raman spectroscopy, another important characterization tool, is introduced in the following section. Finally, I will present the methods for the preparation of the samples and their transfer to TEM grids.

2.1 Electron microscopy

Electrons were first discovered by Sir Joseph John Thomson in 1897 [27]. In 1924 Louis de Broglie hypothesized in his Ph.D. thesis that all matter, including electrons, can exhibit a wave-like behavior [28]. De Broglie described the relation between the particle-like and the wave-like nature of an electron with the equation $\lambda = \frac{h}{p}$, where λ and p are respectively the wavelength and the momentum of the particle and h is the Planck constant. Due to this relationship, electrons can substitute photons to overcome the intrinsic limitations of resolution in light microscopy. It only took a handful of years until in 1931 the pioneering work of Ernst Ruska led to the construction of the first electron microscope and by 1933 his second prototype had for the first time a better resolution than a light microscope. After that, constant progress in electron optics and manufacturing processes has led to modern electron microscopes, that today are capable of imaging the structure of matter at the atomic level.

2.1.1 The transmission electron microscope

Simply put, a TEM consists of three fundamental components: an electron source, a set of electromagnetic lenses and a detector. The electron source (or electron gun) is responsible for the production of electrons that are extracted from a tip by either thermionic or field emission effect. The electrons are then accelerated by an electrostatic potential of typically tens to hundreds of kV and enter the central section of the microscope: the column. Here, depending on the specific microscope, a variable number of electrostatic and/or electromagnetic lenses are used to direct the electron beam to the sample. Provided that the sample is thin enough to allow electron transmission, the scattered electrons are finally collected by a detector. A simplified schematics of the electron trajectories inside a TEM is presented in fig. 2.1. Depending on the operation mode, either the direct image or the diffraction plane can be brought into focus on the detector plane to form, respectively, a real space image or a diffraction pattern of the sample. The objective aperture, which is positioned on the back focal plane, might be used to select the electrons that contribute to form the image. This aperture is often used to increase the ratio between forward transmitted and scattered electrons that reach the detector and thus to increase the image contrast between areas in the sample with different thicknesses (for this reason the objective aperture is often referred to as contrast aperture). The objective aperture is also used for selecting a particular diffraction spot in dark field (DF) mode. The selected area aperture is instead inserted on an intermediate image plane and it is used to limit the image formation on the detector to a selected sample area.

The interaction between the energetic electron beam and the sample produces a rich variety of signals as depicted in fig. 2.2. These signals can be classified into two main categories: electronic and photonic. Among the electronic signals, forward transmitted and elastically scattered electrons are those that have a weak interaction with the sample and conserve their initial kinetic energy. Elastic scattering fundamentally involves interaction between the electrons in the impinging beam and the atomic nuclei of the sample and it is typically used to obtain information on the structure of the sample. Inelastic scattering instead usually involves the interaction between the electron beam and the electronic structure of the specimen. A measurable amount of kinetic energy is lost by the electrons in the beam during the interaction and this information can be used to reveal the chemical composition of the sample. The technique that exploits this effect is called electron energy loss spectroscopy (EELS). The other signals that are produced upon the beam-sample interaction are not relevant for this thesis and will not be discussed here. Nevertheless it is important to notice that each of the signals listed in fig. 2.2, coupled with a suitable detector, can be used to extract relevant information on the sample.

At a typical acceleration voltage $V_0 = 100\,\mathrm{kV}$, electrons with charge e and rest mass m_0 have a relativistic wavelength

$$\lambda = \frac{h}{\sqrt{(\frac{eV_0}{c})^2 + 2m_0eV_0}} \simeq\ 3.7\,\mathrm{pm}$$

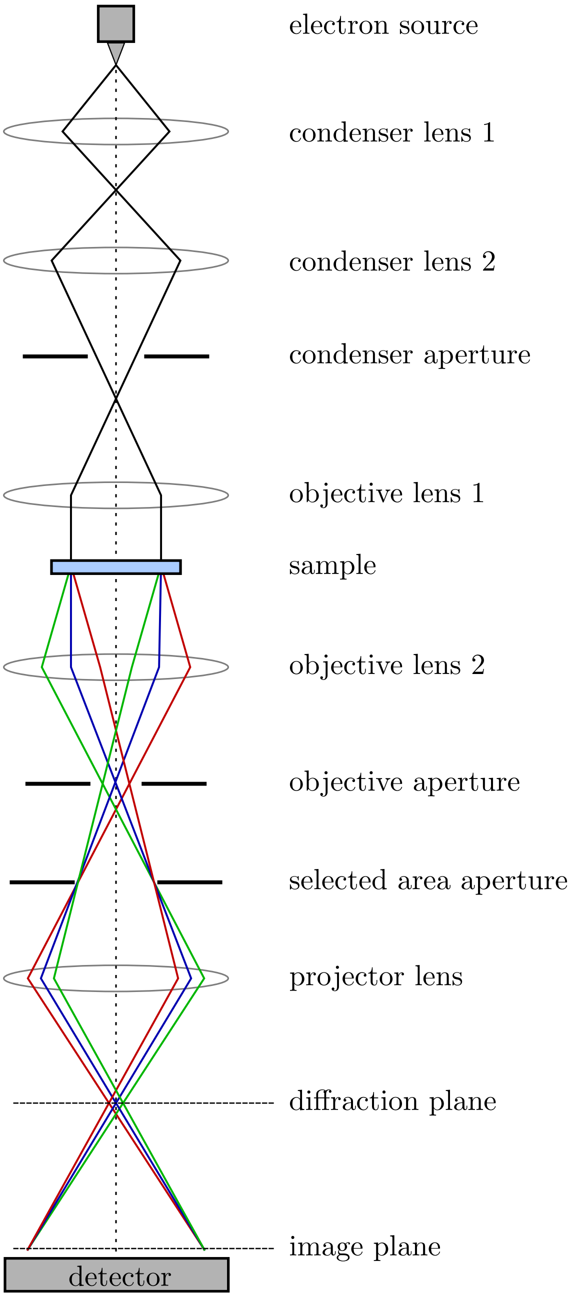

Figure 2.1: Simplified electron ray diagram in a TEM. Rays scattered from different points of the sample into the same direction are focused on the diffraction plane. Rays scattered from the same point of the sample into different directions are focused on the image plane.

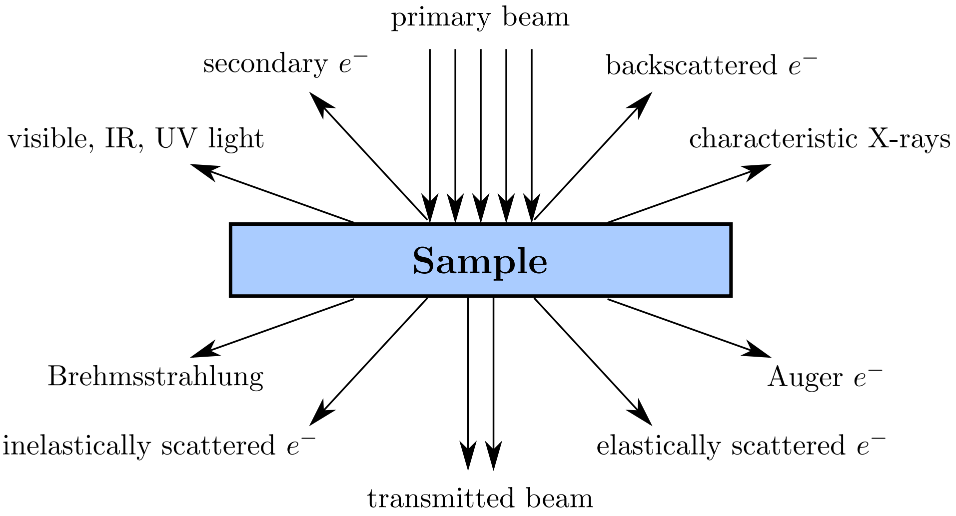

Figure 2.2: Schematic illustration of the rich variety of signals that is produced by the interaction of an energetic electron beam with a thin sample.

This wavelength is two orders of magnitude smaller than the typical interatomic distance in solids, making electrons a tiny enough probe to explore the structure of matter on the atomic scale. Unfortunately, it is not the electron wavelength what limits the resolution in a TEM, but rather spherical aberrations (C_s) and chromatic aberrations (C_c). C_s causes the electrons traveling at large distances from the microscope axis to be focused with higher strength than those traveling closer to the axis. This produces an undefined focal point and therefore the object (the sample) appears blurred on the image plane. C_c, together with the energy spread of the electron beam, also limits the resolution as electrons with larger kinetic energy are focused with higher strength than those with lower energy. In 1936 Otto Scherzer published his famous work on the aberrations of electron lenses [29]. The content of this publication is so important that it is usually referred to as *"Scherzer theorem"* and it states that any electron-optical system will have a positive C_s if these conditions simultaneously hold:

- the optical system is rotationally symmetric
- the system produces a real image of the object
- the fields of the system are static
- there is no charge on the axis of the system

These four conditions are so ubiquitous in a TEM that no obvious way to prevent aberrations seemed to be practicable at that time. Although already in 1947 Scherzer himself proposed a method to correct spherical aberrations [30], it was only in the late '90s that two groups of microscopists were able, independently from each other, to successfully build and test two correctors that actually improved the resolution of the microscope [31, 32]. The idea behind both correctors was to overcome the first of the Scherzer's conditions to break the rotational symmetry of the system. This was implemented by either adding a hexapole lens [31] or a combination of a quadrupole and an octupole lens [32] to produce negative C_s in order to compensate for the intrinsic positive C_s of the instrument. Correctors represent one of the most significant improvements in the history of electron microscopy and they are an essential component of many modern TEMs.

Some of the results contained in this thesis were obtained with a Philips CM200 TEM (see fig. 2.3). Although uncorrected, the CM200 is a very versatile TEM, ideal for conventional bright and dark field microscopy. It features a 200 kV electron gun, a sample stage capable of large tilts (up to ∼50°), cooling and heating holder and an energy-dispersive X-ray (EDX) spectrometer. As significant example of the imaging capabilities of the CM200, fig. 2.4 presents a dark field (DF) analysis of a graphene membrane. Fig. 2.4a shows a bright field (BF) view of a suspended graphene sheet. The diffraction pattern of fig. 2.4b was acquired by illuminating the entire suspended region and it clearly shows a polycrystalline structure. To conveniently image the individual grains of the graphene membrane, an objective aperture was inserted to select a particular diffraction spot. Fig. 2.4c and d are the DF images corresponding to the diffraction spots marked in cyan and in red in fig. 2.4b, respectively. DF imaging enables direct visualization of the grains and of their boundaries that would otherwise be invisible in BF microscopy (note that in fig. 2.4a the membrane does not show any discontinuity or irregularity at the grain boundary). The colored DF image in fig. 2.4e confirms that the two grains are complementary and do not overlap.

2.1.2 The scanning transmission electron microscope

A STEM has many similarities with a TEM and some components, such as the electron source, the lenses and the apertures, are common to both instruments. The most significant difference between the two, is that while in TEM the electron beam is spread on the sample over the whole region of interest, in STEM the probe is focused on a tiny spot and then scanned point by point across the sample. The transmitted electrons are detected at each scanning point and the image is then formed pixel-wise by associating the detected signal to the probe position. The ultimate spatial resolution is solely determined by the size of the probe which, in modern corrected STEMs, is as small as 1 Å or less. After the electrons leave the sample, no additional optical elements are required and a rich variety of detectors can be conveniently used to extract information from the specimen. The most common detector in STEM is

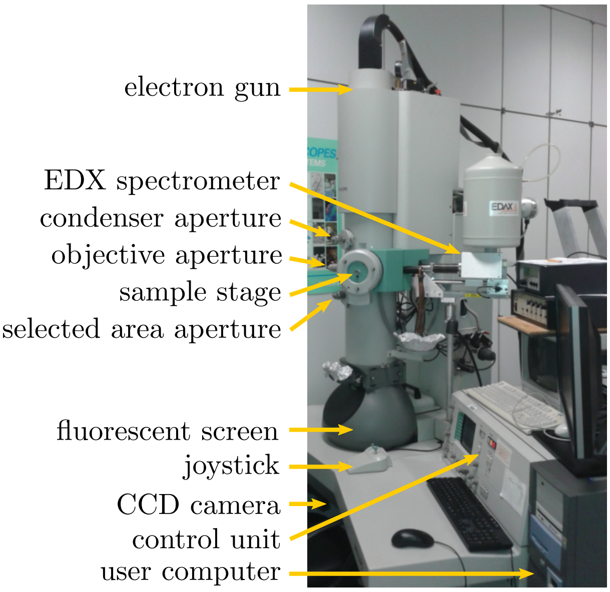

Figure 2.3: A photograph of the Philips CM200 TEM.

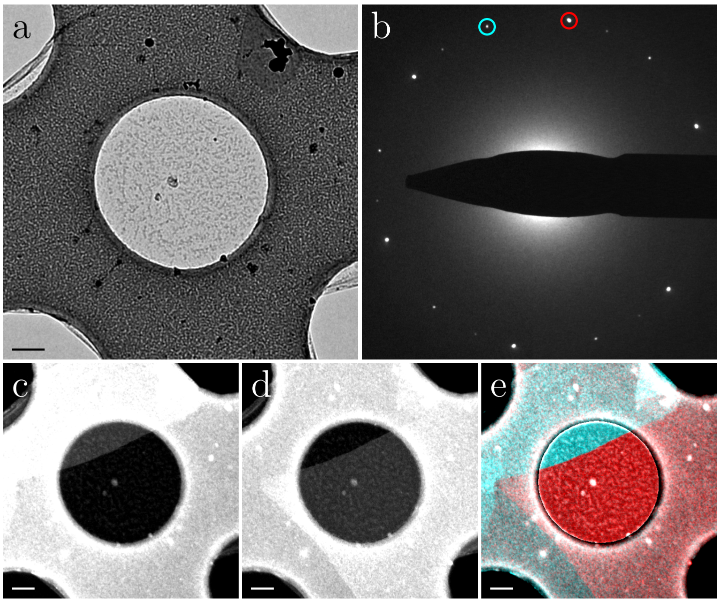

Figure 2.4: Example of DF imaging in the TEM. (a) BF image of a suspended flake of graphene. (b) Diffraction pattern obtained by illuminating the whole suspended graphene area in (a). (c,d) DF images of the same area as in (a) obtained by placing the objective aperture on the diffraction spots marked by the cyan and red circles in (b), respectively. (e) Combined DF image showing the two complementary grains. All scale bars are 200 nm.

the annular dark field (ADF) detector. There are usually two types of ADF detector in a STEM: the high angle annular dark field (HAADF) and the medium angle annular dark field (MAADF). Both detectors consist of a ring-shaped active region with a circular hole in the center to discard unscattered electrons. HAADF and MAADF only differ in the angular range at which they operate. When the beam interacts with the sample, some of the electrons undergo Rutherford scattering with the charged nuclei and are deviated from their original trajectories. The number of scattered electrons at a given angle depends on the thickness of the sample and on the atomic number Z of its atoms. It follows that, for a sample with constant thickness, the ADF detector can discern between atomic species simply by image contrast (often called Z contrast). The electrons that are scattered to small angles can pass through the detector's hole and enter the EELS section. In the EELS prism, the electrons are deflected by a static magnetic field that separates the electron trajectories according to their kinetic energy. The electrons eventually land on a scintillator that converts the impinging electrons into visible light that is recorded by a camera. EELS in the STEM is commonly used to investigate the chemical composition of the sample but other more exotic spectroscopic measurements have also been reported, including the identification of the atomic spin [33], the oxidation states [34] and the local bonding geometries [35]. With appropriate detectors, the STEM can be used to form images from most of the signals of fig. 2.2, making this instrument a very versatile tool capable of simultaneous acquisition of multiple signals.

In September 2013 a NION UltraSTEM 100 was installed in Vienna. Most of the results of this thesis were recorded using this state-of-the-art dedicated STEM. The UltraSTEM is a C_s-corrected instrument equipped with a 100 kV cold field emission gun (CFEG), MAADF and HAADF detectors and a EELS spectrometer. It has a nominal probe size of 1 Å at 30 pA beam current. Compared to other commercially available STEMs, our instrument features a fully bakeable ultra-high vacuum (UHV) system (objective pressure $\sim 10^{-10}$ mbar, gun pressure $\sim 10^{-11}$ mbar), an ultra-stable sample stage, a modular column design that allows for replacements and upgrades and control software that enables the user to easily write custom scripts. A more complete overview of the UltraSTEM microscope can be found in ref. [36]. Fig. 2.5 shows a photograph of the Vienna UltraSTEM instrument together with its schematic drawing adapted from ref. [36].

In the following I present one interesting example of MAADF imaging in the STEM. Fig. 2.6a shows an atomically resolved raw MAADF image of a graphene lattice acquired at 60 kV. Fig. 2.6b is obtained by applying a Gaussian blur filter to reduce the noise and in fig. 2.6c the filtered image is shown with contrast enhancement. After the image processing it becomes evident that one of the atoms is significantly brighter than all others. This is also confirmed by the intensity profile along the yellow line of fig. 2.6b that

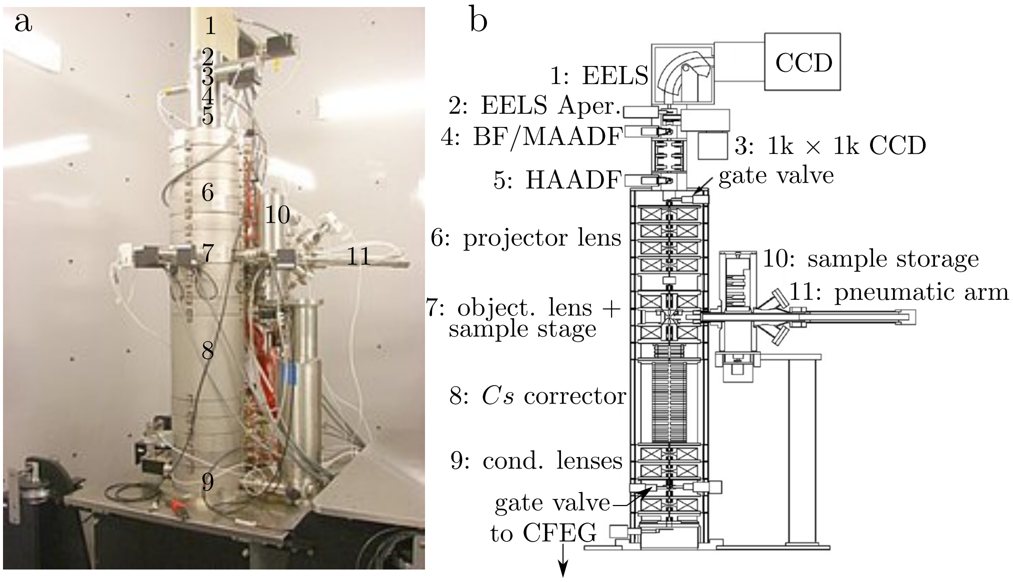

Figure 2.5: The NION UltraSTEM 100. (a) Photograph of the STEM (b) Schematic cross-section of the STEM column adapted from [36].

is shown in fig. 2.6d. As discussed above, Z contrast allows to identify the species of an unknown atom provided that a species in the sample is known and can be taken as reference (like carbon in this case). Then it is possible to assign the unknown atom to a specific element by simply comparing its intensity to the reference [37]. In this case the impurity was found to be a nitrogen atom. For this example, I wish to acknowledge Filippo Fedi who prepared the sample.

High resolution microscopy also allows to unveil the local atomic structure and to study defects in crystals. Fig. 2.7 shows a grain boundary in graphene that I imaged with our STEM. Grain boundaries in graphene are not easy to locate and, even when they have been found, are often hidden by contaminants that tend to accumulate at these locations. The example shown in fig. 2.7 is one rare case of a visible grain boundary in graphene, extending for several nanometers. Fig. 2.7a shows the raw MAADF image. The line of defects that separates the two grains is clearly visible. The inset shows the calculated Fourier transform (FT), where twelve diffraction spots (six per grain) can be seen, both for the first and for the second order. The grain boundary, consisting of a continuous chain of alternating pentagons and heptagons, is better visible in fig. 2.7b, where a Gaussian blur filter was applied to the raw image. The angle mismatch between the two grains is 29°. Fourier filtering allows to hide from the original image either one of the two grains. Fig. 2.7c and d show the inverse Fourier transforms of the FT in the corresponding insets, where one of the two sets of spots was masked out at the time.

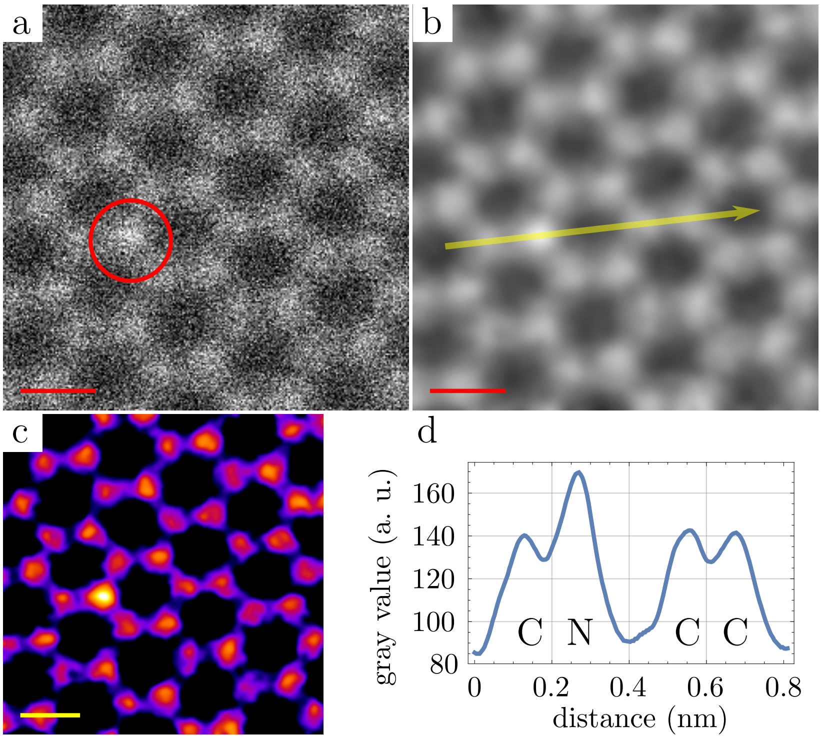

Figure 2.6: Example of MAADF imaging in the STEM. (a) Raw MAADF image of the graphene lattice. A careful observation reveals that the atom marked by the red circle is slightly brighter than all others. (b) Same as in (a) with four-pixel Gaussian blur filtering. (c) Same as in (b) with a color scale to enhance the contrast of the nitrogen atom. (d) Intensity profile along the arrow in (b). All scale bars are 2 Å.

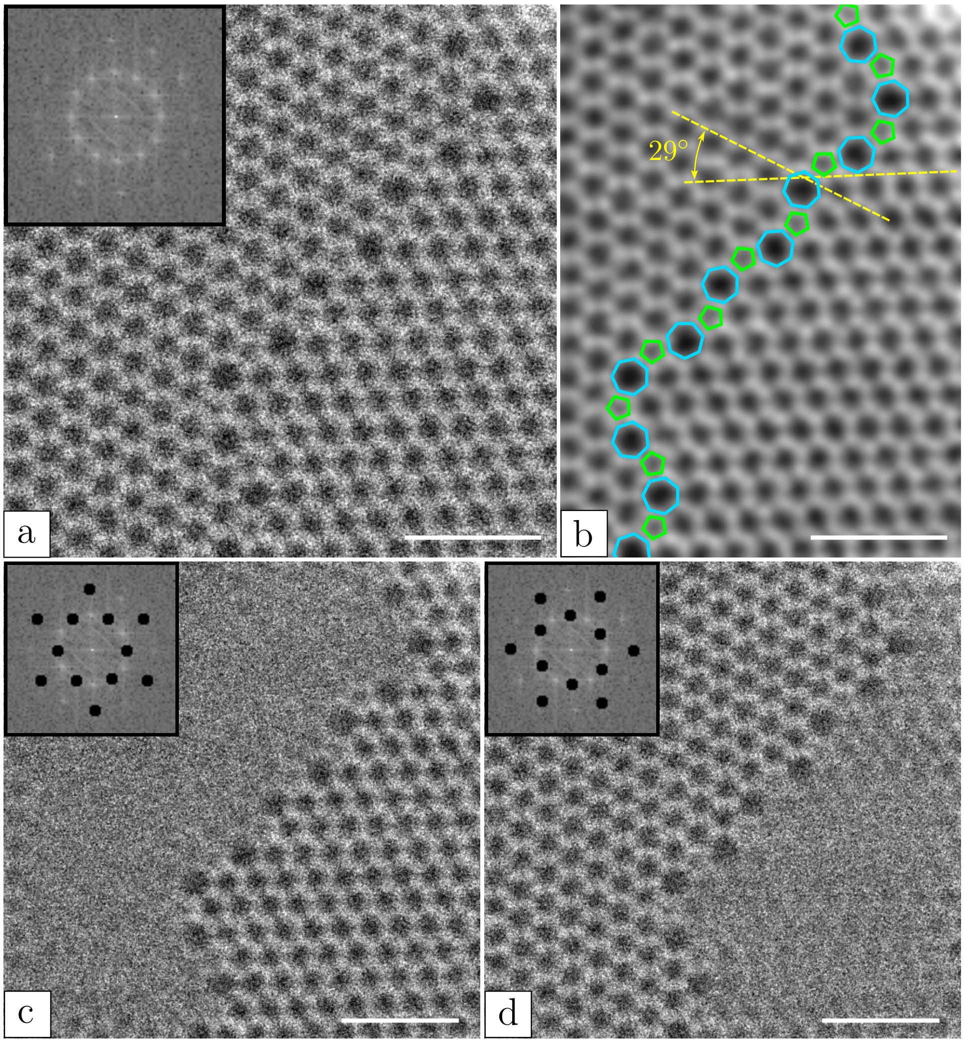

Figure 2.7: (a) Raw MAADF image of a grain boundary in graphene. The inset shows the calculated FT. (b) Same as (a), with a four-pixel Gaussian blur filter. Pentagons and heptagons along the grain boundary are marked in green and in cyan, respectively. All other polygons are hexagons. Each of two the yellow dashed lines is drawn through a crystallographic direction of one grain. (c,d) Inverse Fourier transforms of the FTs in the corresponding insets. For each of the two FTs one complete set of spots was masked out at the time by setting the values of the round selections to zero. All scale bars are 1 nm.

2.2 Raman spectroscopy

When it comes to the characterization of crystalline materials on the micrometer scale, few other techniques are as widely employed as Raman spectroscopy. Raman spectroscopy does not require any sample preparation, can be carried out in air and can easily extract a rich variety of information from the material under investigation. This section is not intended to provide an exhaustive introduction to the fairly complex physics of Raman scattering, but it will rather introduce Raman spectroscopy as a characterization tool for the materials investigated in this thesis.

The most condensed though complete definition of Raman scattering can be formulated as "inelastic scattering of photons by phonons". In a typical Raman setup, the sample is illuminated by a monochromatic laser beam containing photons with wavelength λ and energy $E = \frac{hc}{\lambda}$. The large majority of the impinging photons is elastically scattered by the sample and is discarded from the measurement since it does not carry any information on the sample. A tiny fraction of the incoming light, instead, undergoes a deeper interaction with the sample and an energy exchange between the photons and the vibrational states of the matter (phonons) occurs. The Raman interaction can either decrease the initial energy of the photon if a phonon is created (Stokes scattering) or increase it if a phonon is absorbed (anti-Stokes scattering). In both cases, the difference between the final and the initial energy of the photon is equal to the energy of a vibrational state of the sample. The vibrational states are quantized and characteristic for each material and therefore a Raman spectrum can be interpreted as a footprint of the particular sample under investigation. Moreover, the vibrational states of a certain material are also affected by intrinsic factors such as temperature, chemical doping, isotope ratios and defect density and by extrinsic factors such as mechanical deformation (strain and shear) and electronic doping. Provided that the spectra are properly interpreted, all of these quantities can be probed by Raman spectroscopy. The lateral resolution of this technique is limited by the laser spot size, which for a typical setup is in the order of 400 nm

In fig. 2.8 one example of Raman spectroscopy on 2D materials is presented. The sample considered here consists of a monolayer of hBN mechanically cleaved on top of a silicon oxide substrate and of several chemical vapor deposition (CVD) grown graphene flakes transferred on top of the same substrate. An optical image of the sample is shown in fig. 2.8a, where the contrast was adjusted to maximize the visibility of both materials in respect to the substrate. Raman spectra of three selected spots are presented in fig. 2.8b, where the number of each spectrum refers to the measurement location marked in fig. 2.8a. Measurement 1 is performed on the bare silicon substrate and the corresponding Raman spectrum shows two pronounced peaks at $520\,\mathrm{cm}^{-1}$ and at $960\,\mathrm{cm}^{-1}$. These two vibrational modes can be assigned to the transverse optical (TO) phonon mode and to the two phonon 2TO mode of the silicon crystal respectively (note that the very intense TO peak is reduced in intensity by a factor of 5). For measurement 2 the laser beam is moved to a region where the Si substrate is covered by the hBN flake. Since a monolayer of hBN is nearly optically transparent, the incoming photons can easily reach the Si substrate and probe both materials simultaneously. This can be seen in spectrum 2, where in addition to the already introduced Si peaks, one more feature is now visible. The additional peak is located at $1366\,\mathrm{cm}^{-1}$ and corresponds to the E_{2g} in-plane vibrational mode of the hBN lattice (note that the intensity of this peak is increased by a factor of 10). Finally, measurement 3 is performed on a region where a graphene flake is stacked on top of the hBN layer. As expected, spectrum 3 shows additional peaks that must be attributed to the presence of graphene. The two most intense peaks are located at $1580\,\mathrm{cm}^{-1}$ and at $2700\,\mathrm{cm}^{-1}$. The first peak is due to the E_{2g} vibrational mode of the graphene lattice and it is analogous to the hBN peak at $1366\,\mathrm{cm}^{-1}$. For historical reasons, since this peak is common to all graphitic sp^2-bonded carbon materials, it is commonly known as G peak. The second graphene peak is found at $2700\,\mathrm{cm}^{-1}$ and it originates from a second order scattering process of zone-boundary phonons. This peak is usually named $2D$[1]. Other two, less intense, peaks appear at both sides of the $2D$ mode and are attributed to additional vibrational modes of the graphene lattice. This simple example shows how Raman spectroscopy can unambiguously identify materials based on their unique spectroscopic signatures.

---

[1] The reason for the name is that the $2D$ peak is found at twice the wavenumber of the first order D peak, which only appears in defective graphene (hence the name D from “defect”).

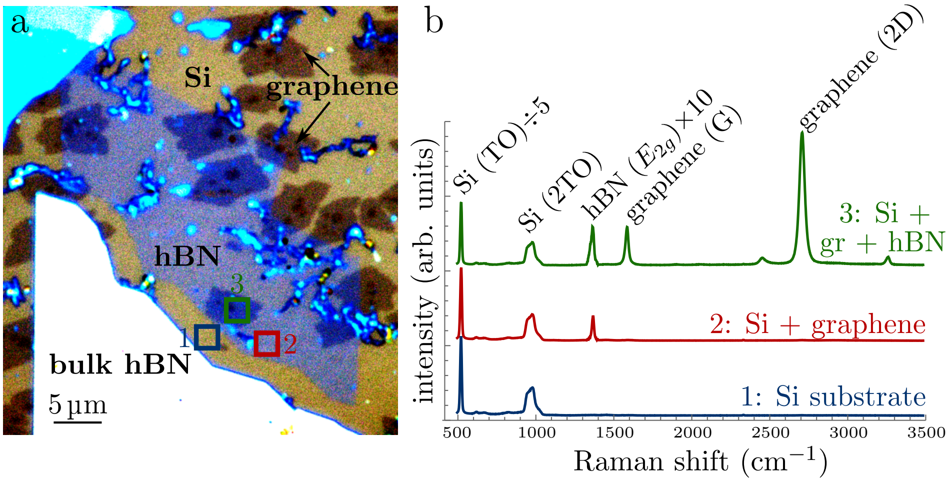

Figure 2.8: Example of Raman spectroscopy. (a) Optical microscopy image of the sample, consisting of exfoliated hBN flakes and CVD grown graphene islands on top of a silicon substrate. (b) Raw Raman spectra obtained from three different locations. The measurement location of each spectrum (1–3) is label by the corresponding number in (a). For the sake of clarity, the intensity of Si (TO) peak was divided by a factor of 5, while the intensity of the hBN (E_{2g}) peak was multiplied by a factor of 10.

2.3 Sample preparation

No experiment could possibly be successful without proper preparation of the samples. Sample preparation is a very vast topic and the specific techniques that are used can be different for each experiment. In this section I present the most relevant and well established techniques that have been used during the course of my research.In sections 2.3.1 and 2.3.2 two alternative methods for the production of graphene are introduced, while section 2.3.3 focuses on the transfer of the sample to other substrates.

2.3.1 Mechanical exfoliation

Mechanical separation (exfoliation) of the weakly bound layers of graphite is, from a chronological perspective, the first successful method to isolate graphene. The exfoliation method was introduced by Geim and Novoselov in 2004 and since then there has not been any significant modification to the original technique. In brief, an adhesive tape is folded around a graphite crystal (fig. 2.9a) and it is then repeatedly opened and closed to cleave the crystal into thinner flakes (fig. 2.9b). Because of the weak interaction between atomic planes and the strong in-plane covalent bonds, the graphite crystal will preferentially break separating adjacent planes. Once the material on the adhesive tape is so thin to appear almost transparent (fig. 2.9c), a silicon substrate coated by a silicon oxide (SiO_2) layer is pressed against the tape to pick up some of the flakes (fig. 2.9d). Next, an optical microscope can be used to search for graphene monolayers distributed on the silicon chip along with thicker graphite flakes.

The thickness of the SiO_2 layer plays a crucial role in making graphene visible asdiscussed in ref. [38]. In this work, the authors calculate and show experimentally that the contrast of a graphene flake with respect to the SiO_2 background is maximized for a few selected oxide thicknesses, substantially reducing the choice to either 90 or 300 nm. The contrast is predicted to increase linearly with the number of layers (up to ~5-7 layers), allowing straightforward identification of the thickness of a flake by simple optical inspection. Fig. 2.10a presents an optical image of an exfoliated graphene flake on a 90 nm SiO_2/Si substrate, where areas with different contrast can be identified. Fig. 2.10b shows the intensity profile plots along the two lines marked in fig. 2.10a. The profile along each line changes abruptly in a stepwise manner, with each step being approximately 7% in contrast. An intensity variation of 7% corresponds to the contrast of a monolayer of graphene, confirmed by the fact that no smaller contrast variations were ever found for this SiO_2 thickness. As clearly seen in fig. 2.10b, all other intensity levels along the profiles are an integer multiple of this elementary step. Based on this observation, it is possible to assign to each region of the flake the corresponding number of layers, as marked in fig. 2.10a by the overlaid numbers.

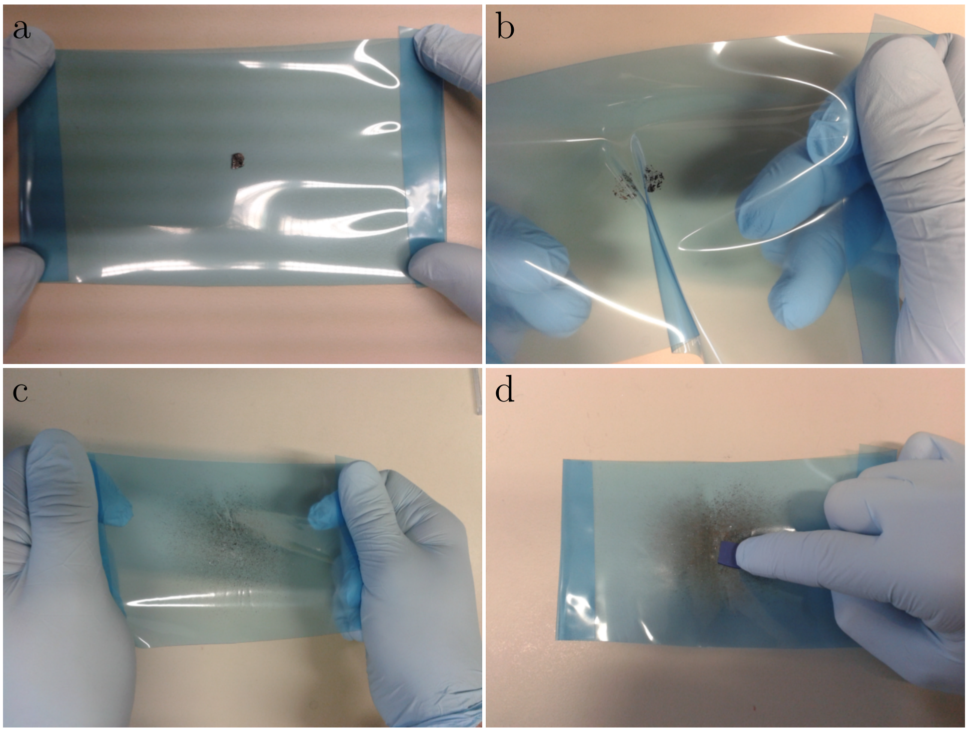

Figure 2.9: Mechanical exfoliation. (a) A bulk crystal of graphite is deposited on a piece of adhesive tape. (b) The tape is folded and reopened again to cleave the crystal. (c) This operation is repeated several times until the cleaved flakes appear almost transparent. (d) A SiO_2/Si chip is pressed against the tape to pick up some of the exfoliated flakes.

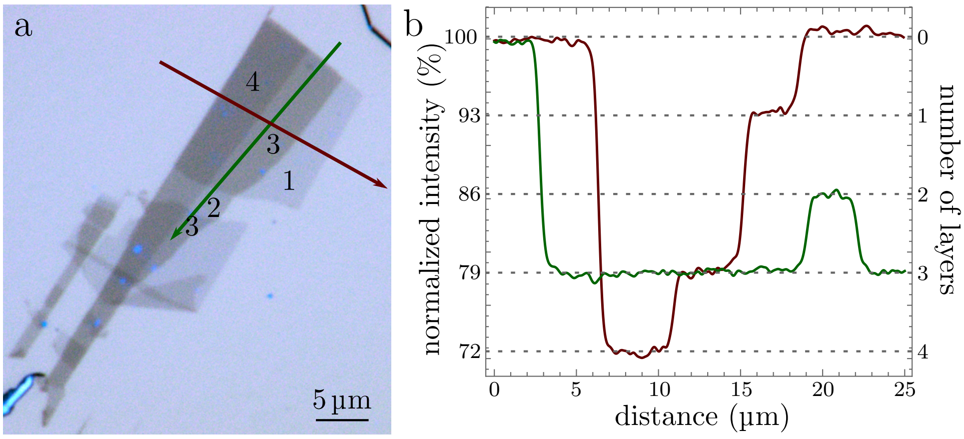

Figure 2.10: Optical analysis of an exfoliated graphene flake. (a) Optical microscopy image of the flake. The number of layers in each region is indicated by the overlaid numbers. (b) Two intensity profiles along the two arrows in (a).

Graphene flakes obtained by mechanical exfoliation are monocrystalline and have very low defect density. However, the lateral extension of an exfoliated graphene flake is typically in the range of up to some tens of micrometers. Also, the exfoliation process requires a fair amount of manual work and is difficult to automate for mass production. For these reasons, the preferred manufacturing method for applications that require large area graphene is chemical vapor deposition, which is introduced in the next section.

2.3.2 Chemical vapor deposition

Chemical vapor deposition (CVD) is widely employed in the semiconductor industry to produce thin films of various materials including metals and crystalline silicon. CVD has been known for over a hundred years and in the last decade this technique became very popular for the production of low dimensional carbon materials.

A typical CVD setup for graphene production consists of a hollow cylindrical furnace and of a quartz tube placed at its center. The quartz tube is connected to a vacuum pump at one end and to a gas inlet at the other. Fig. 2.11a shows a photograph of the CVD system that was used to produce most of the samples analyzed in this thesis. The synthesis of graphene by CVD is described in the following. A catalytically active metal foil (usually copper or nickel), is placed in the quartz tube and the volume is evacuated. Once the base pressure of the chamber is reached, the gas inlet valve is opened to allow the forming gas to enter the tube. Forming gas is a solution of hydrogen and argon in a 5:95 ratio. Argon does not participate in any of the chemical reactions but it is used as carrier and to prevent hydrogen to reach a concentration that might be explosive. The furnace is then turned on and the substrate is heated to a temperature that is close to its melting point. Once the target temperature is reached, the substrate is kept under a constant flow of forming gas for some time, ranging from a few minutes to over one hour. This is the so-called "pre-annealing step". This step is performed to remove the native oxide layer that covers the metal foil by exposure to hydrogen and to flatten its surface to provide a cleaner and more homogeneous substrate for graphene growth. After the pre-annealing has completed, the gas inlet connected to the carbon precursor is opened.

Fig. 2.11b shows a cross sectional schematic illustration of the growth mechanism inside the furnace for the case of graphene growth on copper from a methane precursor. The numbers 1–6 indicate the following significant reactions occurring during graphene growth:

1. Methane molecules are thermally decomposed into reactive CH_x species.
2. The reactants are adsorbed on the substrate's surface.
3. Unstable CH_x species can further decompose upon interaction with the catalyst, leading to desorption of molecular hydrogen.
4. Adsorbed carbon atoms are weakly bound to the substrate and have enough thermal energy to migrate on the Cu surface.
5. Not fully dehydrogenated CH_x species can react with hydrogen and desorb.
6. Atomic carbon migrates until a nucleation site is reached. This might be an already formed graphene flake, a Cu step edge or other surface imperfections. Carbon atoms bind covalently to each other to form a graphene lattice which, because of the planar geometry of the substrate, is the energetically favored structure.

After growth, the furnace is cooled back to room temperature while keeping a constant flow of forming gas. During growth, the Cu foil serves both as physical substrate and as catalyst for carbon adsorption. Since the graphene passivates the catalytic power of the foil, the growth is expected to terminate once the graphene covers the entire Cu surface. This surface mediated process is known as "self limiting" and it ensures that mostly monolayer graphene is synthesized. For other metals with larger carbon solubility, as nickel for instance, the growth kinetics involves diffusion of carbon atoms into the bulk of the substrate and the graphene is then formed upon cooling through segregation of carbon back to the surface. In this case multilayer graphene is typically produced.

While the exfoliation method introduced in the previous section has not changed significantly in the last decade, CVD growth of graphene has been extensively explored in the last couple of years, to the point that probably

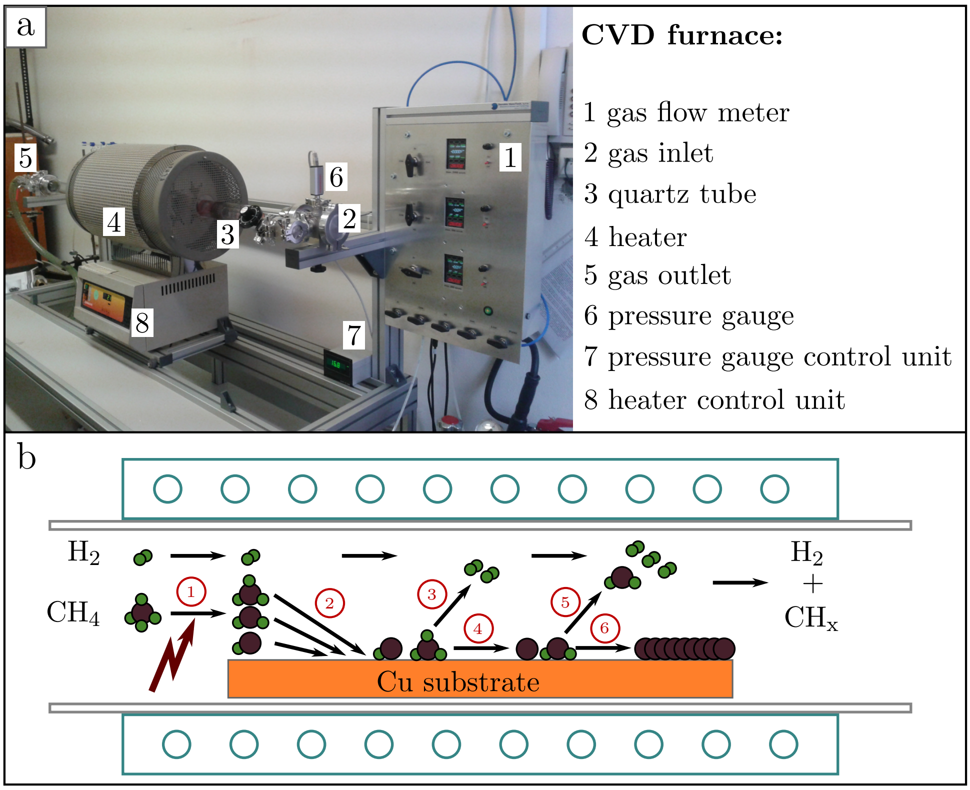

Figure 2.11: CVD synthesis. (a) Photograph of the CVD furnace used to synthesize most of the samples analyzed in this thesis. (b) Schematic cross-section of the CVD furnace and simplified illustration of the graphene growth dynamics. See main text for more details.

every group in the world has developed its own favorite growth method. This is mainly because of the large variety of parameters that can be varied in a CVD system, which include temperature, pressure, growth time, choice of precursor gas and substrate, preparation of the catalyst, flow rate, cooling rate and so on. The modification of each of these parameters can lead to completely different results. The positive aspect of this variety of different growth methods is that, with some effort, the synthesis can be modified to target a desired product.

Compared to its exfoliated counterpart, CVD graphene suffers from lower quality in terms of structural and electrical properties. This is mostly because of its polycrystalline nature and despite recent progress, the production of wafer-sized monocrystalline graphene is still to be achieved. Nevertheless, prototype systems for cost effective mass production of polycrystalline CVD graphene already exist and the next few years are expected to be an exciting time for industrial progress in this field [39–41].

2.3.3 Transfer to other substrates

Regardless of the production method, 2D materials often need to be transferred to a substrate different than the one used for their synthesis. For instance, the electronic transport properties of graphene produced by CVD cannot be tested on the metallic substrate used for the growth. For the purposes of this thesis the necessity for transfer mainly arises from the experimental methods that are used. For TEM investigation, the sample needs to be detached from either the silicon substrate (for the case of exfoliation) or the metallic foil (for CVD) and transferred to a support that allows electron transmission. The support used in this work is a 3 mm 200 mesh[2] TEM gold grid coated with a perforated amorphous carbon foil. These TEM grids were purchased from Quantifoil® Micro Tools GmbH and for simplicity I will refer to the holey carbon foil as Quantifoil® (QF) in the rest of this thesis. The transfer procedure to a QF grid is different for an exfoliated sample and for a CVD grown one.

Some of the steps of the transfer method for exfoliated graphene are illustrated in fig. 2.12 (for a more detailed report see [42]). A QF grid is laid down on the silicon substrate on which the target flake has already been identified (fig. 2.12a, where a graphene monolayer region is marked with red dashed line). With the help of a micro manipulator, the grid can be dragged over the silicon substrate until the desired position of the flake with respect to the grid has been achieved (fig. 2.12b). At this point, a drop of isopropyl alcohol (IPA) is released next to the grid to wet both the substrate and the QF. Upon evaporation of the IPA, the QF is pulled into contact with the Si substrate. To detach the flake from the substrate a two-molar aqueous solution

---

[2] the mesh size is the number of grid bars per inch

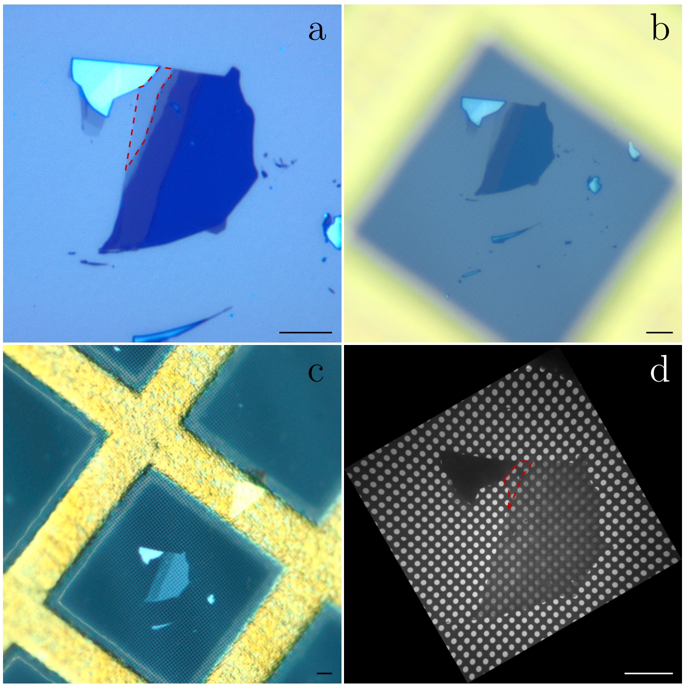

Figure 2.12: Transfer of exfoliated graphene to a TEM grid. (a) An exfoliated graphene flake on a SiO_2/Si substrate. The dashed line marks the position of a monolayer. (b) The same flake as in (a) seen through an overlaid TEM grid. (c) The flake suspended on the QF after transfer to the TEM grid. (d) TEM image of the transferred flake. The dashed line indicates the monolayer region. All scale bars are 10 µm.

of potassium hydroxide (KOH) is used to dissolve the SiO_2 layer. A few drops of KOH solution are released on the substrate and after a few minutes the TEM grid with the transferred flake should be freely floating in the solution. As last step, the grid is rinsed in deionized water to remove any residue of the KOH solution and then rinsed once more in clean IPA. After evaporation of the IPA the grid is ready for optical inspection to confirm that the flake has been successfully transferred (fig. 2.12c). Suspended monolayer graphene can be difficult to observe in the optical microscope because it is nearly transparent. Fig. 2.12d shows a low magnification TEM image of the transferred flake. Although slightly damaged, the monolayer region is still attached to the QF, while the thicker regions are perfectly intact.

Let us now consider CVD grown graphene. Depending on the growth time and on the flow rate of the precursor gas, the growth of graphene can extend to the whole substrate surface and create a continuous film, or it can be limited to a partial coverage, where separated “islands” of graphene discontinuously cover part of the available surface. Unfortunately, unlike exfoliated flakes on

SiO_2, monolayer graphene on copper is not optically visible. This might be a disadvantage as time-consuming measurements like Raman spectroscopy or scanning electron microscopy (SEM) are required to locate the flakes. This issue might be circumvented by exploiting the property of graphene of being an excellent protective coating against corrosion and oxidation. Fig. 2.13a shows an optical image of a copper substrate partially covered by well visible graphene flakes. This was achieved by post-growth annealing of the copper foil on a hot plate at 200 °C for 2 minutes in air. As a result of the high temperature combined with the presence of oxygen in the air, the exposed surface of the Cu foil starts to oxidize, while the graphene coated regions are prevented from reacting with oxygen. The difference in color between oxidized and not oxidized areas creates a sufficient optical contrast to identify the graphene islands.

To transfer CVD grown graphene to QF TEM grids, two different procedures can be followed: the polymer-assisted or the polymer-free transfer method. The latter one, which was the preferred method for this thesis, is described in detail in [43] and it is schematically illustrated in fig. 2.13e: the QF TEM grid is placed on the graphene coated substrate (step 1) and a drop of IPA is used to pull the grid in tight adhesion with the copper foil (step 2). Fig. 2.13b and c show the TEM grid on the Cu foil during and after IPA evaporation, respectively. After the IPA evaporates, the Cu foil changes its apparent color, a convenient way to quickly check whether the adhesion step was successful. The Cu/graphene/grid sandwich is then released on the surface of a 10% weight aqueous solution of $FeCl_3$ (step 3). After several hours the Cu foil is completely etched, while the graphene and the TEM grid are left intact (step 4). At this point the grid is picked up from the solution and rinsed in deionized water and in IPA to remove residues of the etchant (step 5). To confirm that the transfer was successful, the grid can be then inspected in a TEM. Fig. 2.13d shows an overview of a region of the QF, where a significant amount of holes are covered by a continuous graphene monolayer. The polymer-assisted transfer involves one additional intermediate step, in which the graphene is first transferred to a sacrificial Poly(methyl 2-methylpropenoate) (PMMA) layer and then, after Cu etching, the graphene/PMMA stack is transferred to a TEM grid. In the final step, the PMMA is removed via solvent. The advantage of the polymer-assisted transfer is that usually a large coverage of the TEM grids can be achieved, whereas direct transfer is more susceptible to perforation of the graphene membrane. However, it is difficult to remove PMMA completely and the transferred graphene will be typically dirty, while the direct transfer results in clean graphene and is also an easier and faster method.

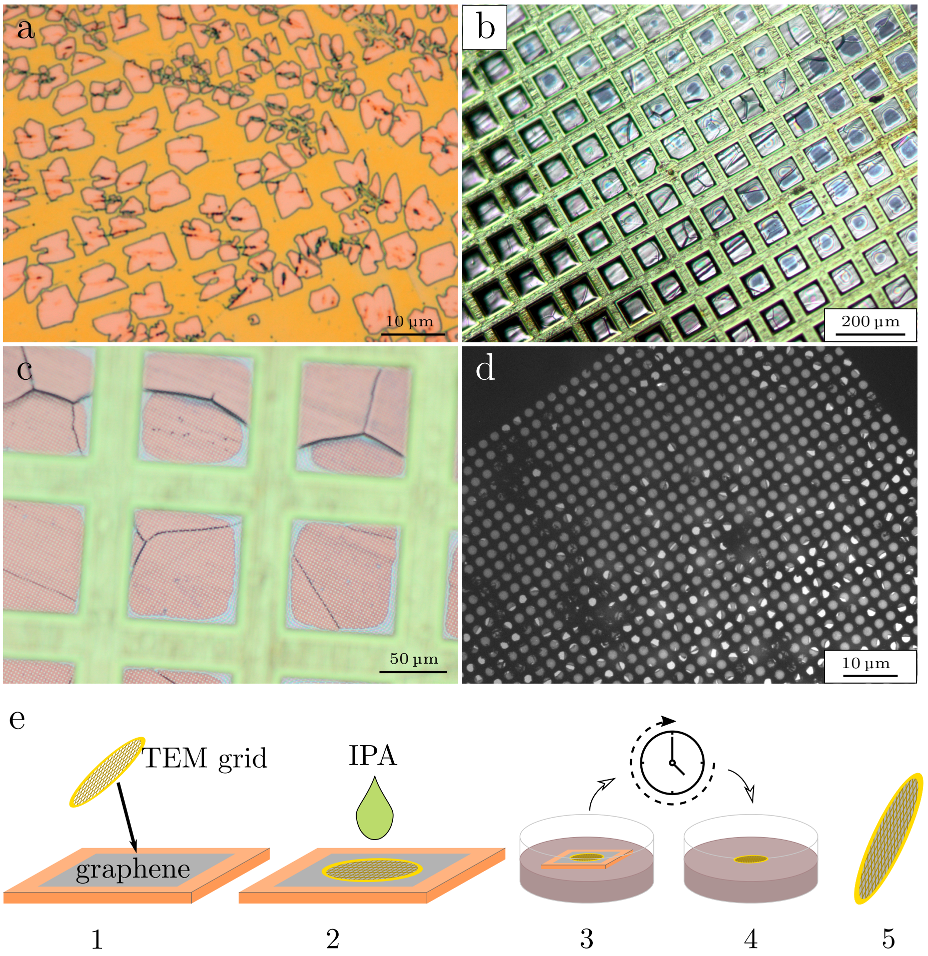

Figure 2.13: Transfer of CVD grown graphene to a TEM grid. (a) Isolated graphene flakes on the Cu substrate. (b) The TEM grid during IPA evaporation. (c) The TEM grid in adhesion with the substrate. (d) TEM image of the transferred graphene. (e) Illustration of the polymer-free transfer method.

Chapter 3

Advances in STEM

3.1 Limitations of current ADF detectors

The HAADF and the MAADF detectors, introduced in section 2.1.2, are the most widely used detectors in STEM. They allow fast scanning speed and because of their central hole they can be used in combination with EELS. Also, the capability of these detectors to discern between atomic species by simple intensity contrast is surely one of the reasons that contributed in making ADF detectors so popular among microscopists. Nevertheless, both HAADF and MAADF fail to capture in great detail the scattering dynamics of the electron beam with the sample. ADF detectors are monolithic: they detect only a subset of the available signal and output a cumulative measurement, i.e. they integrate the counts over the whole active surface during the exposure time and they return one number that is proportional to the overall detected signal. This means that there is no way of knowing *where* on the detector the triggering event occurred. Fig. 3.1 shows a simplified schematic of the scattering dynamics of a convergent electron beam with the sample. The dashed line represents the trajectory of an electron that is Rutherford scattered to an angle θ and that intercepts the detector's plane at a point described by the polar coordinates r and φ as drawn in the figure. None of the ADF detectors will be able to capture the coordinate φ of the event. Regarding the coordinate r, the ADF detector will only be able to probe whether $r_{min} \leq r \leq r_{max}$, where r_{min} and r_{max} are, respectively, the inner and outer radius of the detector. In brief, ADF detectors fail in providing a directional-sensitive detection of the scattered beam. This means that part of the information on the electron-nucleus interaction is lost not because it is not accessible in principle, but because it is hidden by the nature of the detector.

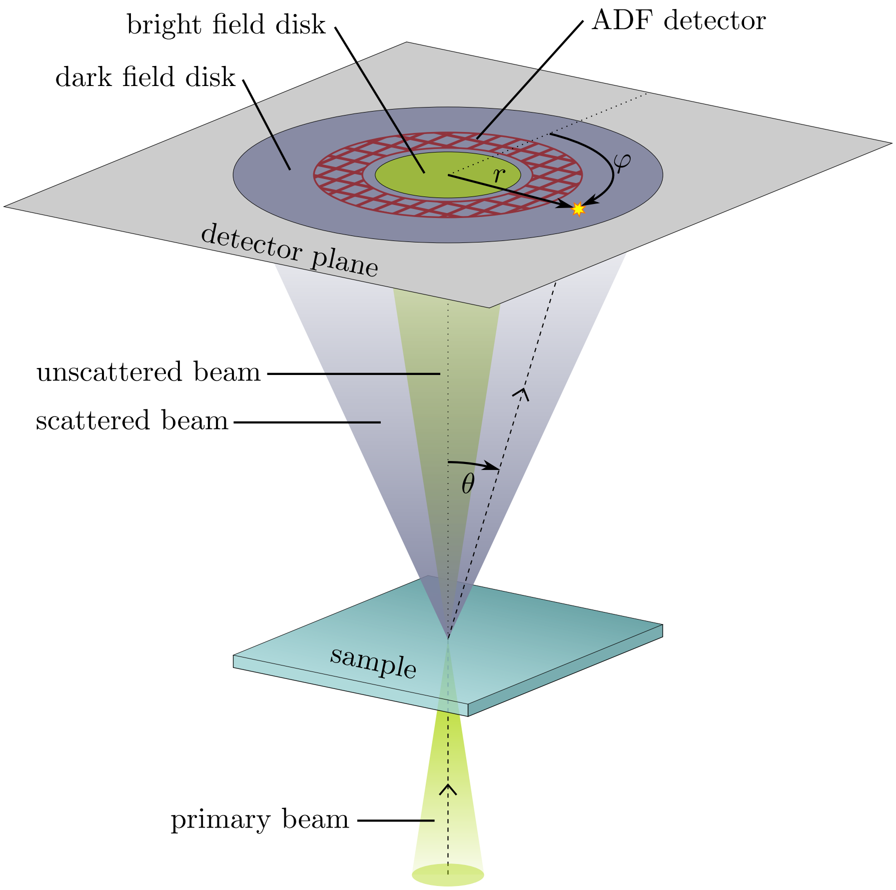

Figure 3.1: Simplified schematic illustration of the interaction of a convergent electron beam with the sample.

3.2 Pixelated ADF detection

To overcome the limitations of ADF detectors and to make efficient use of the rich signal available, new detection methods are emerging. The common idea behind some of them is to record the full 2D image of the transmitted beam for each point of the 2D scanned region, thus creating a four-dimensional (4D) dataset. For instance, it is possible to record 4D convergent beam electron diffraction (CBED) patterns as a function of STEM probe position to gain insight into various material properties [44, 45]. With a similar approach, one can use a pixelated detector to record the entire BF disk and the overlapping scattered disks to perform phase contrast imaging [46]. This technique is called ptychography and was first introduced by Nellist and Rodenburg [47, 48] as an improvement of differential phase contrast based on detectors consisting of two [49, 50], four [51] or eight [52] quadrants. One of the major advantages of 4D STEM is the ability to simultaneously extract a broad variety of signals from a single dataset, including bright field, annular bright field, dark field, center of mass and differential phase contrast, simply by post-acquisition selection of a portion of the detector [53].

In the following I treat theoretically the case of a pixelated annular dark field (PADF) detector that is used to detect the intensity of the electron beam elastically scattered by a graphene lattice, and show how such a detector can be employed to extract information on the electron scattering.

The simulated data presented in this section was obtained with the QSTEM software developed by C. Koch [54]. QSTEM is a software for quantitative simulation of TEM and STEM images based on a multislicing approach. If the option is selected, QSTEM saves for each scanned pixel the calculated two-dimensional intensity distribution of the electron exit wave that is generated on the detector's plane, ultimately producing a four-dimensional PADF dataset. Fig. 3.2a shows an aberration-free simulated STEM MAADF image of the graphene lattice obtained with a 60 keV beam having a 25 mrad convergence half-angle. Here the image is formed by the electrons scattered in the 60–200 mrad half-angle range, which is the typical detection range for the NION MAADF detector. Fig. 3.2b shows an example of the annular scattered intensity that is computed on the detector's plane (the BF disk was removed after the simulation by setting the corresponding pixels to zero). The scattered intensity in this case is the average of all diffracted intensities for the pixels contained in the graphene unit cell (marked in red in fig. 3.2a) and it is shown in logarithmic scale to enhance the visibility of the weak high-angle scattered signal. The inner and outer diameters of the MAADF detector are indicated by the two red circles. A full two-dimensional image of the diffracted intensity allows a more detailed analysis of the scattering process compared to the MAADF signal.

Consider for instance the following simple case: an individual electron crossing the sample plane at the position marked with 1 in fig. 3.2a is expected to be scattered towards the direction of the nearest nucleus, that is, in the direction shown by the arrow. Similarly, the electron that passes through the sample at the position marked with 2 is also expected to be scattered towards the nearest nucleus. As a result, one can predict that the detected signal on the detector will not be symmetric in the two cases: if the same reference system is used in fig. 3.2a and b, the electron passing at position 1 will cause a more intense signal in the lower half of the detector, while the electron passing at position 2 will cause a more intense signal in the upper half of the detector.

To test whether this hypothesis is correct, I analyze the 4D PADF dataset with the annular center of mass (ACOM) method. For each diffracted intensity distribution the center of mass of the image is calculated and its position is stored by the two polar coordinates r and φ. Each of these two coordinates has an important physical meaning. The radial coordinate r can be interpreted as the "degree of asymmetry" in the scattering process: the larger r is, the more anisotropic the scattering event is, producing an asymmetric illumination of the detector respect to its center. If the the scattering is isotropic instead, then the illumination of the detector is circularly symmetric, the position of the ACOM is at the center of the detector and r goes to zero. The angular coordinate φ, in the case of an asymmetric scattering event, indicates the dominating direction in the scattering process. In brief, r and φ together quantify the preferential scattering direction of the electron beam.

Fig. 3.2c shows the r map of the graphene lattice, where the color scale goes from black, for $r = 0\,\mathrm{mrad}$, to white, for $r = 1\,\mathrm{mrad}$. The red overlay indicates the position of six atoms. The map shows minima of intensity at the atomic positions, at half distance between neighboring atoms and at the center of the hexagons. These locations correspond exactly to those points where the in-plane electrostatic field produced by the nuclei cancels out and no preferential electron scattering direction exists. In all other points of the plane there is a residual non-zero component of the field that causes the electrons to be preferentially scattered in one direction and displaces the ACOM of the detected signal up to $\sim$1 mrad. The position-dependent preferential scattering direction is shown in the φ map of fig. 3.2d, where the color spectrum covers the entire 0–2π range. The r and φ maps are combined in fig. 3.2e, where the intensity and the color encode, respectively, the radial and the angular coordinate of the ACOM, as graphically illustrated in fig. 3.2f. The $r + \varphi$ map confirms that the spots labeled as 1 and 2 are not equivalent but correspond to two lattice locations where the beam gets scattered in two opposite directions. This difference is not visible in fig. 3.2a where the same two spots display the same gray value and are therefore identical. More in general the $r + \varphi$ map provides a much richer description of the electron-sample scattering dynamics than a traditional ADF image. It is important to highlight that ADF images can always be post-generated after PADF acquisition by integrating the signal

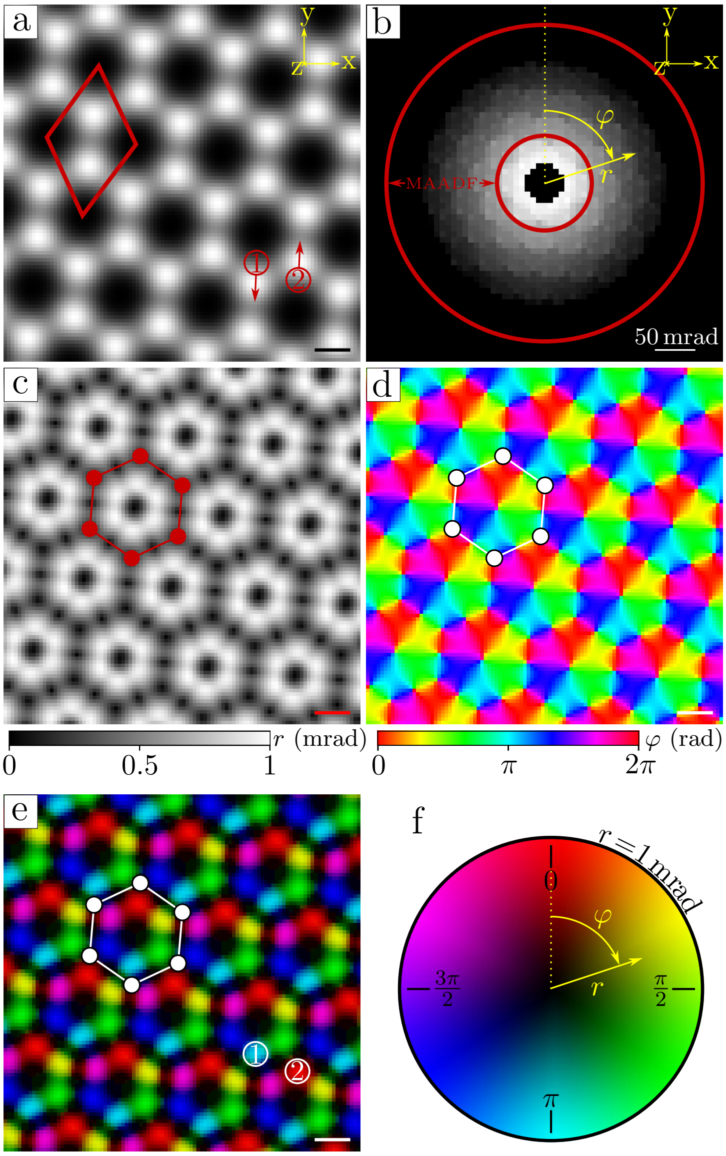

Figure 3.2: QSTEM simulation of the graphene lattice with PADF/ACOM analysis. (a) MAADF image of the graphene lattice obtained by integrating the intensity of the computed exit wave functions in the 60–200 mrad range. (b) Scattered intensity in logarithmic scale averaged over the graphene unit cell as drawn in (a). The red circles delimit the angular range for the MAADF detector used to obtain (a). The coordinates r and φ identify the position of the ACOM. (c,d) r and φ maps of the same area as in (a), respectively. (e) Combined $r + \varphi$ map. (f) Color scheme used for the $r + \varphi$ map. Scale bars in (a), (c), (d) and (e) are 1 Å.

in the detector area. In fact, PADF is much more versatile than ADF because it allows to generate a real image of the sample from practically any arbitrarily shaped virtual detector that one might wish to use by simply integrating the scattered intensity in the desired region of interest. This way the imaging capability of the STEM is not limited by the monolithic HAADF and MAADF detectors but the full range of scattering angles becomes accessible and can be explored in a continuous fashion.

3.3 Implementation of the custom detector

As just shown in the previous section, PADF acquisition offers, at least in the theoretical case, many advantages over traditional ADF imaging. The next obvious question is whether such an acquisition setup can be realized experimentally. In this section I show how a custom detector for PADF measurements was implemented in our STEM.

Graphene is a very weak electron scatterer and almost all of the transmitted beam is contained in the BF disk, while only a small fraction of it is scattered to high angles. To be able to detect only the latter component, the intense BF disk needs to be hidden from the detector to avoid overexposure and to minimize inter-pixel crosstalk at the edge of the BF disk. To achieve this, a custom aperture was fabricated. The aperture is shown in fig. 3.3c and it consists of a regular 3 mm gold TEM grid coated with a continuous amorphous carbon foil on top of which a 1 µm thick Cu layer was thermally evaporated through a hollow mask to produce a disk with a 400 µm diameter. After deposition, the carbon foil was removed using oxygen plasma etching, leaving the Cu disk suspended on the grid bars. The aperture was then inserted into the STEM in one of the slots dedicated to EELS apertures. A simplified schematic of the path of the electron beam is illustrated in fig. 3.3a. The projector lenses of the microscope are adjusted so that the bright field disk is just as large as it needs to be in order to be completely blocked by the Cu disk, while the scattered component of the beam can be transmitted through the aperture and reach the EELS prism. Importantly, the EELS spectrometer can be used with or without energy dispersion. In the first case the electrons are separated according to their energy along the x direction (see reference system in fig. 3.3). As a consequence, the spatial information of the directional scattering along the x axis is lost and substituted by energy dispersion. This mode was employed for the ^{12}C – ^{13}C EELS detection method discussed in section 4.3. In the second case, when no energy dispersion is used, the information on the scattering direction of the electrons is maintained through the EELS prism both along the x and the y axes. This detection mode was employed for the directional scattering analysis of the graphene/hBN heterostructure presented in section 4.1. In both cases the scattered electron beam eventually reaches the scintillator and produces a light signal that is detected by a charge-coupled device (CCD) camera (Andor iXon 897 EMCCD). An example exposure of the CCD camera for the case of a non energy-dispersed scattered beam is shown in fig. 3.3b. The Cu disk is clearly recognizable at the center of the image, as well as the "shadow" of the grid bars arranged in a square pattern. This image is the experimental equivalent of fig. 3.2b.

In fig. 3.4 an example of a real PADF acquisition on graphene is presented. The ADF image of the lattice is shown in fig. 3.4a and was generated by integrating the diffracted intensity collected in the 60–140 mrad half-angle range. An example of the detected PADF signal, averaged over the pixels of the graphene unit cell marked in fig. 3.4a, is shown in fig. 3.4b. The two red circles mark the inner and the outer diameter chosen for the virtual detector. The graphene lattice in fig. 3.4a is atomically resolved and the noise-level in the image is low, proving the PADF detector to work as expected. Nevertheless, compared to the computed case of fig. 3.2a, this image has fewer pixels per lattice unit area. The limiting factor here is the speed of the CCD camera which, depending on the specific settings, can read at a frequency in the range of 100–1000 fps. For the experimental image of fig. 3.4a the exposure time for each pixel was 3 ms. For comparison, the MAADF image of fig. 2.6a was acquired with 16 µs dwell time, which translates into almost 200 times faster scanning speed. To avoid scanning distortions, the total frame time should not exceed the few seconds time scale, which, in turn, implies that the number of pixels has to be drastically reduced for PADF acquisition. Clearly, the slow reading speed of the CCD camera is what currently limits the performance of PADF measurements. Since faster cameras exist, an upgrade of the current setup would allow for faster scanning and combine the speed of traditional ADF imaging with the versatility of PADF measurements.

In conclusion of this chapter, I have shown that common ADF detectors fail to provide a detailed description of the electron-atom scattering dynamics. In particular, no information on the direction of scattering can be retrieved from ADF measurements. A significant improvement is introduced by using a pixelated detector which is able to record the full 2D distribution of intensity of the scattered beam. The PADF detector was first treated theoretically and then its experimental implementation was described. Despite poor pixel resolution due to slow acquisition speed of the CCD camera, the custom detector was successfully tested on graphene. Sections 4.1 and 4.3 contain experimental results based on PADF measurements.

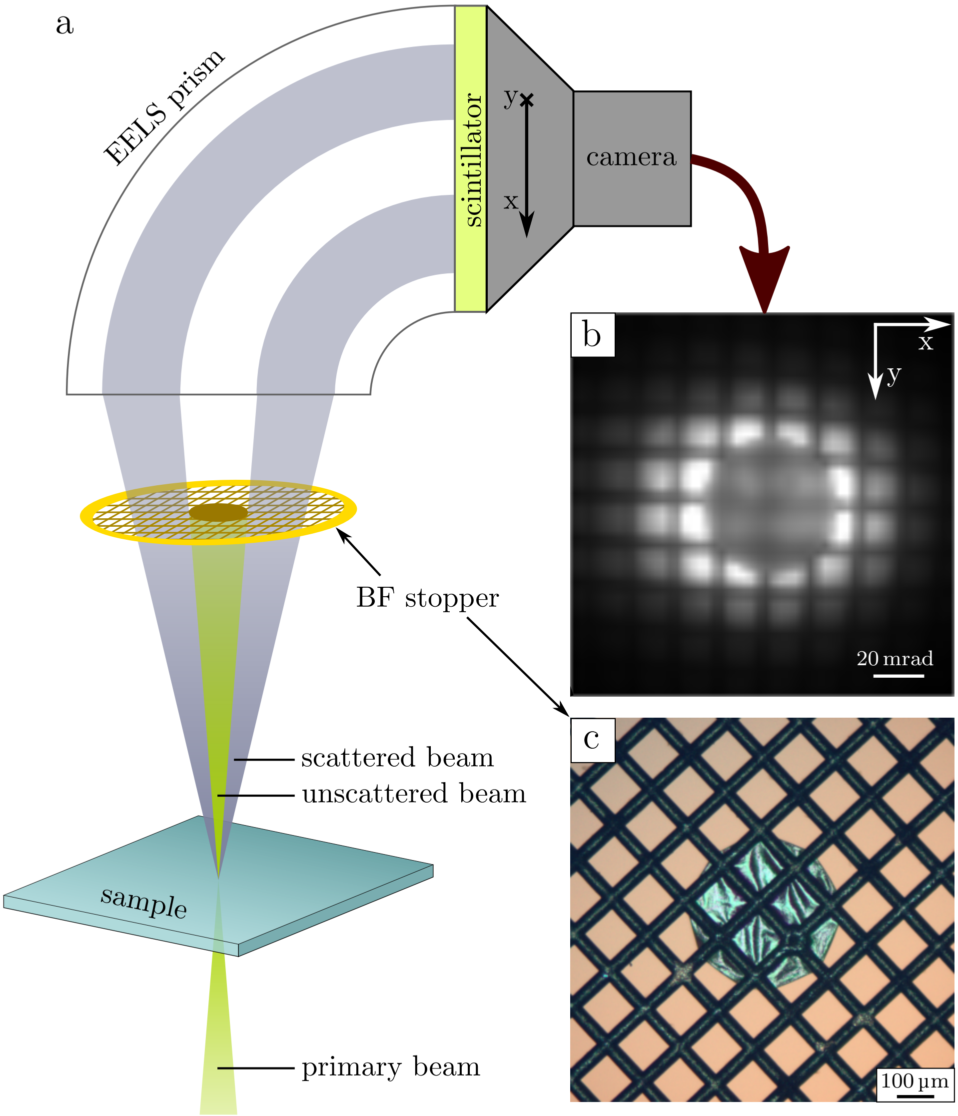

Figure 3.3: Implementation of the PADF detector. (a) Schematic illustration of the electron beam trajectory. The bright field disk is stopped by the custom aperture while the scattered beam is let through. The diffracted intensity is then collected on the EELS scintillator and recorded by the CCD camera. (b) Example of actual exposure on the CCD camera. (c) Optical image of the custom EELS aperture, showing the Cu disk suspended over the grid bars.

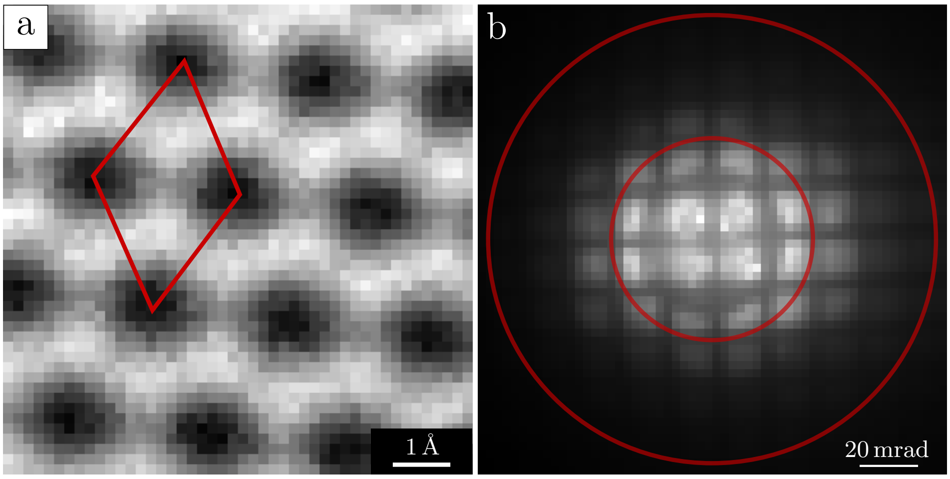

Figure 3.4: PADF measurement of the graphene lattice. (a) Atomically resolved graphene lattice obtained from a PADF dataset by integrating the detected scattered intensity in the 60–140 mrad range. (b) Detected PADF signal averaged over the lattice unit cell as marked in (a). The red circles delimit the area chosen as virtual detector.

Chapter 4

Results and discussion

This chapter is dedicated to the results that were achieved during the course of my Ph.D. and that are partially published in peer-reviewed scientific journals. The chapter can be conceptually divided into two parts. Section 4.1 is devoted to the analysis a graphene/hBN heterostructure, where the custom detector was used to determine its 3D structure. Sections 4.2, 4.3 and 4.4, focus on carbon isotope detection in a STEM, either by EELS spectroscopy of high-angle scattered electrons using the custom detector (sections 4.2 and 4.3) or by electron knock-on damage (section 4.4).

4.1 Topology of a graphene/hBN heterostructure

The content of this section is based on entry 1 of the List of publications.

4.1.1 Sample preparation and preliminary characterization

Van der Waals heterostructures were introduced in section 1.1.2 as an exciting new frontier in the field of 2D materials. Among such heterostructures, graphene on hBN is certainly one of the most studied. Both crystals are chemically inert, have similar crystal structures and their lattice constants only differ by 1.8%. Compared to SiO_2, hBN provides a flatter, cleaner and electronically more homogeneous insulating substrate [55–57] and is now routinely used to manufacture high-performance graphene-based devices [55, 58, 59]. Besides serving as an excellent substrate, hBN also provides graphene with a periodical potential that, in the case of carefully aligned crystals, can lead to small commensurate areas [60].

In contrast to previous works, where thick (bulk) hBN was used as a substrate for single-layer graphene, a suspended heterostructure consisting of monolayer graphene on monolayer hBN is investigated here. Since the sample does not have a rigid support, fundamental phenomena governing the interaction between the two crystals are accessible in the absence of external

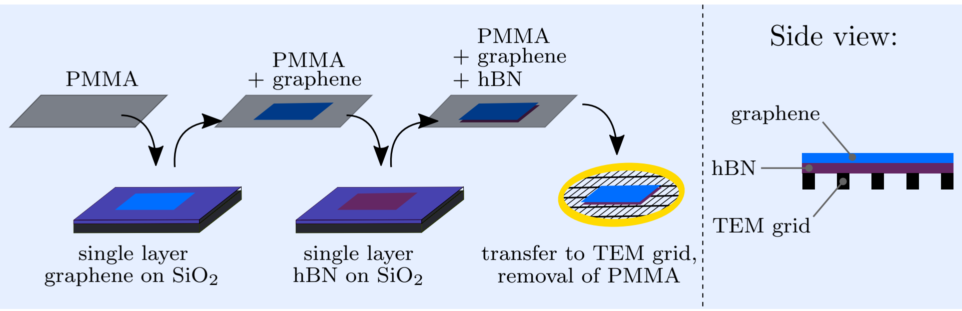

Figure 4.1: Schematic illustration of the sample preparation and of its transfer to a QF TEM grid.

perturbations. The structure is investigated via TEM and STEM, using low electron energies (80 keV for TEM and 60 keV for STEM) in order to minimize radiation damage [61]. In the STEM investigation, the used detection scheme is very sensitive to small local tilts of the sample, which allows to obtain the 3D shape of the heterostructure through a comparison to model structures.

To fabricate the sample, an hBN crystal was cleaved on top of an oxidized Si wafer. A single layer hBN flake, chosen by optical observation, was picked up by a single layer graphene attached to a PMMA membrane following the method described in ref. [62] and illustrated graphically in fig. 4.1. The dry transfer method ensures clean interface between the flakes. Because both hBN and graphene cleave preferentially along their main crystallographic directions, during the transfer procedure flakes with well-defined facets were used and were aligned (within a precision of 1.5°) using a rotating positioning stage under an optical microscope. Since the edges of the flakes are either armchair type or zigzag type, aligning the facets of graphene and hBN can result with equal probabilities in heterostructures having either 0° or 30° relative angular twist. The bilayers were then transferred onto gold QF TEM grids, where portions of the heterostructures are suspended on holes measuring approximately 1.5 µm in diameter. A thin layer of Pt was deposited on the TEM grids (prior to attaching the 2D sample) in order to reduce hydrocarbon contamination [63].

I investigated two heterostructures in the Philips CM200 TEM operated at room temperature at 80 kV. Fig. 4.2a and b show two BF images of the first sample, recorded at two neighboring QF holes. Although apparently similar in BF mode, the two areas show significantly differences in the diffraction patterns. The diffraction pattern of the area of fig. 4.2a is shown in fig. 4.2c, and it reveals that the suspended membrane consists of a single crystal rather than a heterostructure. This is because the two flakes are only partially overlapping and, a priori, it is not possible to say whether this crystal is graphene or hBN. The intensity profile of the diffraction pattern along the gray line is shown in fig. 4.2e: the relative intensity of the first and second order diffraction spots indicate that the crystal is a monolayer [64]. For the area shown in fig. 4.2b the diffraction pattern in fig. 4.2d clearly indicates that the sample consists of a stack of two crystals twisted by ∼30°. The intensity profiles along the two drawn lines are shown in fig. 4.2f and prove that both crystals are monolayers. The circular dashed overlays are drawn through one set of diffraction spots for both the first and second order reflections. The other two sets of spots consistently fall inside the drawn circles, i.e. they are all closer to the center of the diffraction pattern. This is especially well visible for the second order reflections. Also, the intensity profiles in fig. 4.2f show that the peaks along the red line are slightly further apart from each other than the ones along the blue line. The position of the diffraction spots indicates that the two layers are different crystals. Since graphene has a slightly smaller lattice constant than hBN, the inner and the outer set of reflections are attributed, respectively, to hBN and graphene (one graphene and one hBN reflection is indicated by the red and the blue arrow in fig. 4.2d, respectively). The lattice mismatch, calculated as the ratio of the measured distances of the two sets of spots from the center of the diffraction pattern, is $(1.80 \pm 0.17)\%$, in good agreement with the predicted value of 1.8%. By comparing the crystallographic orientations in the diffractions patters in fig. 4.2b and d and considering that exfoliated samples are single crystals, the suspended layer in fig. 4.2a is identified as graphene. Fig. 4.2g shows two EDX spectra acquired at the two considered areas. The most evident differences of the spectrum taken at the bilayer in respect to the monolayer are the peak at ∼400 eV and the shoulder at ∼180 eV. These two features are attributed to the K edge electronic transitions of nitrogen at 397 eV and of boron at 188 eV, respectively. The EDX data thus confirms that the monolayer region is graphene, while the bilayer contains graphene and hBN. The additional peaks for silicon and oxygen can be attributed to the silicon oxide contamination often observed in STEM images, while the gold peak probably originates from the TEM grid.

I then considered the second sample. Fig. 4.3a shows a BF image of the suspended heterostructure. The diffraction pattern, taken from the entire QF hole, is shown in fig. 4.3b. As for the 30° twisted heterostructure, two distinct sets of diffraction spots with hexagonal symmetry can be observed, but this time the two crystals are precisely aligned to each other, with only 1° relative twisting. Again, because of the mismatch between the lattice constants of graphene and hBN, it is possible to assign the outer and the inner set of spots to the graphene and to the hBN lattice, respectively. The red and the blue arrow in fig. 4.4b indicate one graphene and one hBN diffraction spot, respectively. Fig. 4.3c shows a DF image from the same QF hole, acquired by selecting with the objective aperture one graphene and one hBN spot simultaneously. The selected spots are marked by the red circle in fig. 4.3b. In contrast to the BF image, in DF mode a strong modulation of the intensity appears, with bright parallel lines arranged on a dark background. The in-

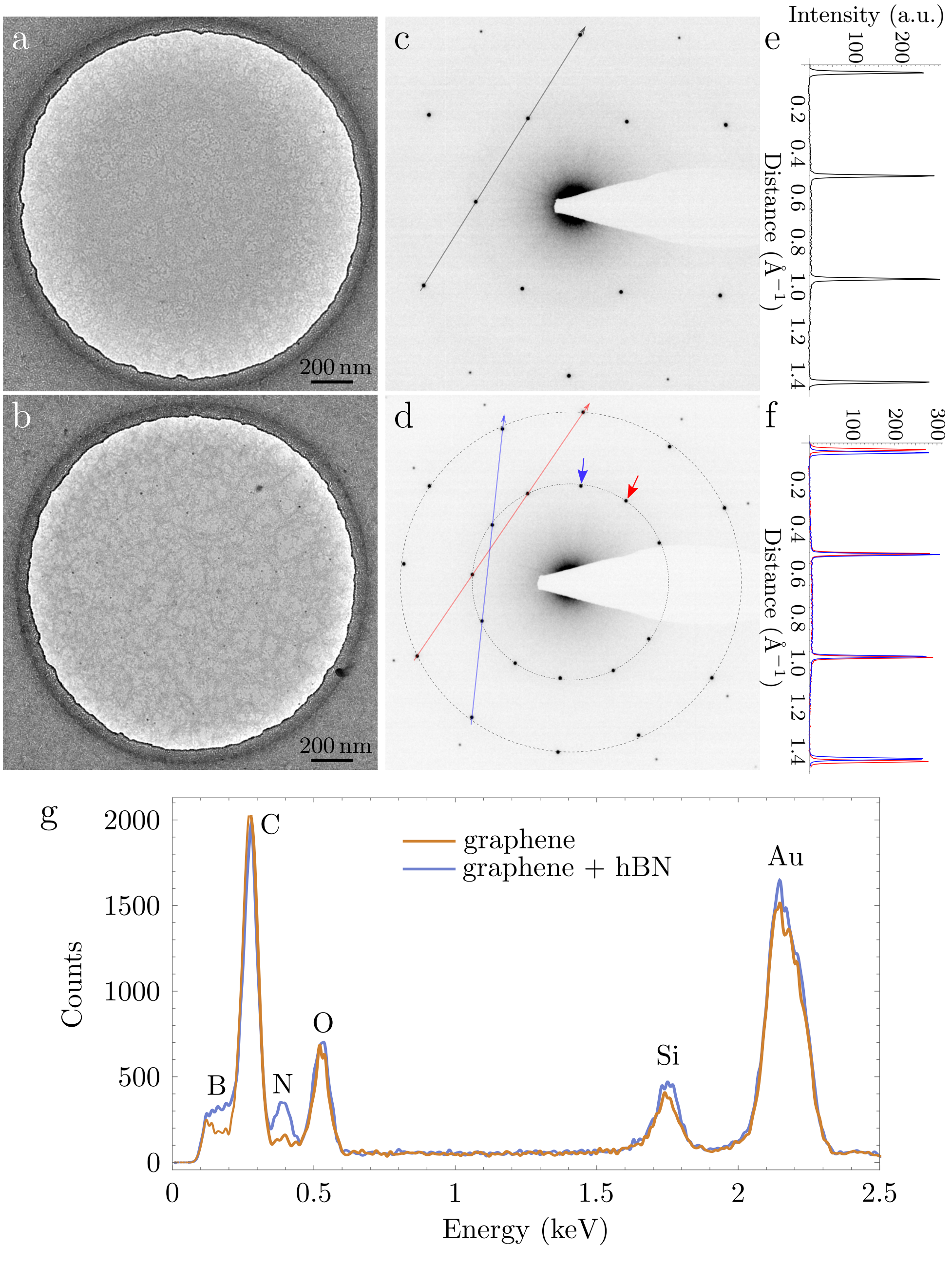

Figure 4.2: (a,b) BF images of two neighboring QF holes covered by graphene (a) and by the graphene/hBN heterostructure (b). (c,d) Diffraction patterns of (a) and (b) respectively, obtained by illuminating the whole suspended regions. The intensity profiles along the drawn lines are shown in (e,f). (g) EDX spectra acquired on graphene and on the heterostructure (200 seconds accumulation time).

tensity modulation abruptly vanishes within the area marked by the yellow box. Fig. 4.3d–g show the region inside the box at a higher magnification. The BF view of fig. 4.3d does not show any abrupt change in intensity and it confirms that the suspended membrane is continuous throughout the field of view. In contrast, the DF images of fig. 4.3e, f and g, acquired selecting the spots marked by the red, green and blue circles in fig. 4.3b respectively, show a very sharp edge between the region decorated with fringes and the homogeneously dark area. Each inset of fig. 4.3e–g displays the calculated Fourier transform (FT) for the respective panel. From the FT, the measured period of the intensity modulation is $\sim$10 nm for all three directions. I interpret these fringes as a one-directional resolved moiré interference pattern originated by the superimposition of the graphene and of the hBN lattices. In this perspective, the sharp transition observed in fig. 4.3e–g can be explained by an hBN edge which delimits the graphene/hBN bilayer region (on the left side of the edge) and the graphene monolayer region (on the right side)[1]. Moiré superlattices were already observed by atomic force microscopy (AFM) and STM in other works for the case of graphene on bulk hBN [56, 57, 60, 65–67]. The predicted moiré period for a 1° misaligned graphene/hBN bilayer is 9.9 nm [68], in good agreement with the value measured with the FT analysis.

The aligned heterostructure is then investigated at a neighboring QF hole, where the bilayer extends over the entire hole. Fig. 4.4a shows a BF image of the suspended heterostructure. At the locations marked with red arrows, dark patches of contamination are clearly visible. Their nature and position on the sample are discussed below. Fig. 4.4b shows the diffraction pattern obtained by illuminating the whole suspended area of the sample. Again, in DF mode, the moiré interference pattern can be clearly visualized: fig. 4.4c shows a DF image of the same area of fig. 4.4a. Fig. 4.4d shows the area inside the yellow square in fig. 4.4c at higher magnification. The objective aperture used for DF imaging is marked by a red circle in fig. 4.4b. Interestingly, the moiré pattern changes when the sample is tilted. Fig. 4.4e shows again a DF image of the same area of fig. 4.4a, acquired with a sample tilt of 16° (the tilt axis in the reciprocal space is indicated by the dotted black line in fig. 4.4b). A magnified view of the area inside the yellow box is shown in fig. 4.4f. The interference pattern now changes to bright spots arranged in a triangular lattice, showing that tilting the sample allows to resolve the moiré pattern in all three directions. Note that the periodicity of these modulation does not change compared to the non-tilted case.

At some locations the moiré interference pattern is completely suppressed (marked by arrows in fig. 4.4e, corresponding to the same locations marked in fig. 4.4a). These regions (which also appear much darker in the BF image)

---

[1] In principle the opposite case (a graphene edge and a hBN monolayer on its right side) is also possible, but I tend to exclude it because the hBN flake was much smaller than the graphene flake.

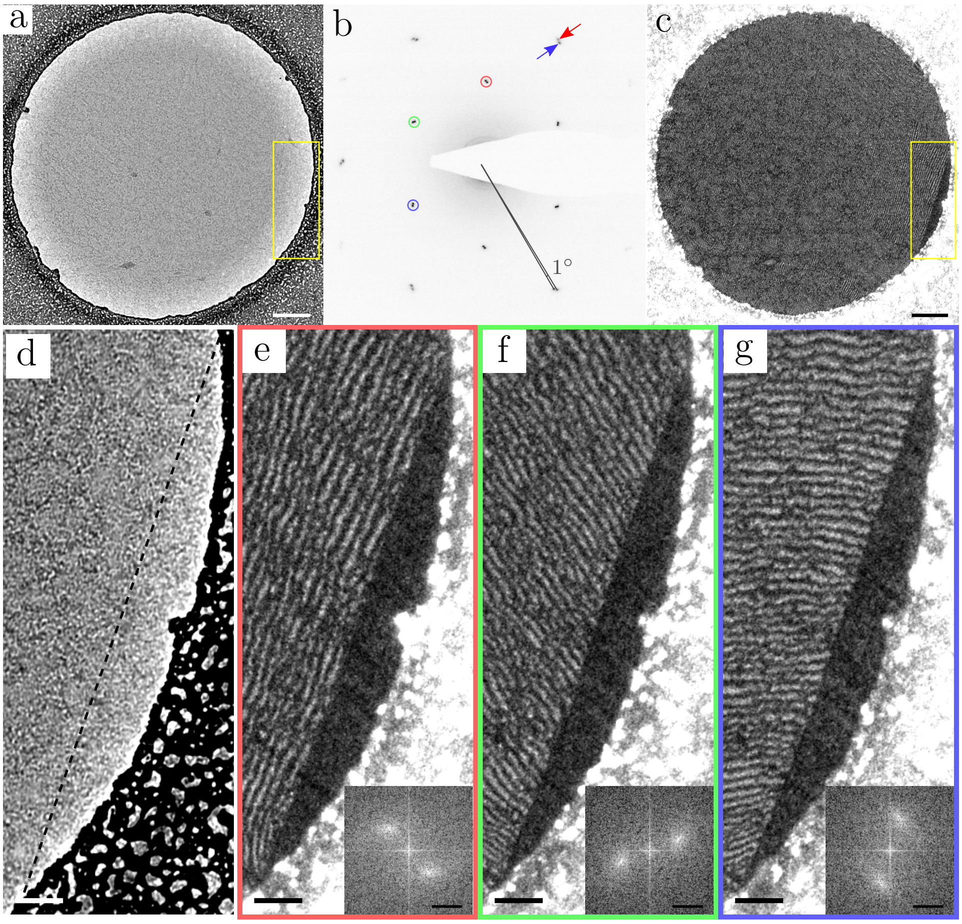

Figure 4.3: (a) BF image of the suspended heterostructure. (b) Electron diffraction pattern from the area in (a). The red and the blue arrows indicate one graphene and one hBN diffraction spot, respectively. (c) DF image of the same area as in (a), obtained by selecting with the objective aperture one graphene and one hBN spot, marked by the red circle in (b). The strong contrast variation visible in the yellow box originates from the edge of the hBN flake. The area contained in the yellow box in (a) and (c) is shown at higher magnification in (d) in BF mode and in (e–g) in DF mode. The dashed line in (d) indicates the edge of the hBN flake. (e), (f) and (g) were obtained by selecting the diffraction spots marked by the red, green and blue circles in (b), respectively. Insets in (e–g) show the FT of the image in the respective panels. Scale bars are 200 nm in (a) and (c), 50 nm in (d–g) and 10 nm^{-1} for the FT insets.

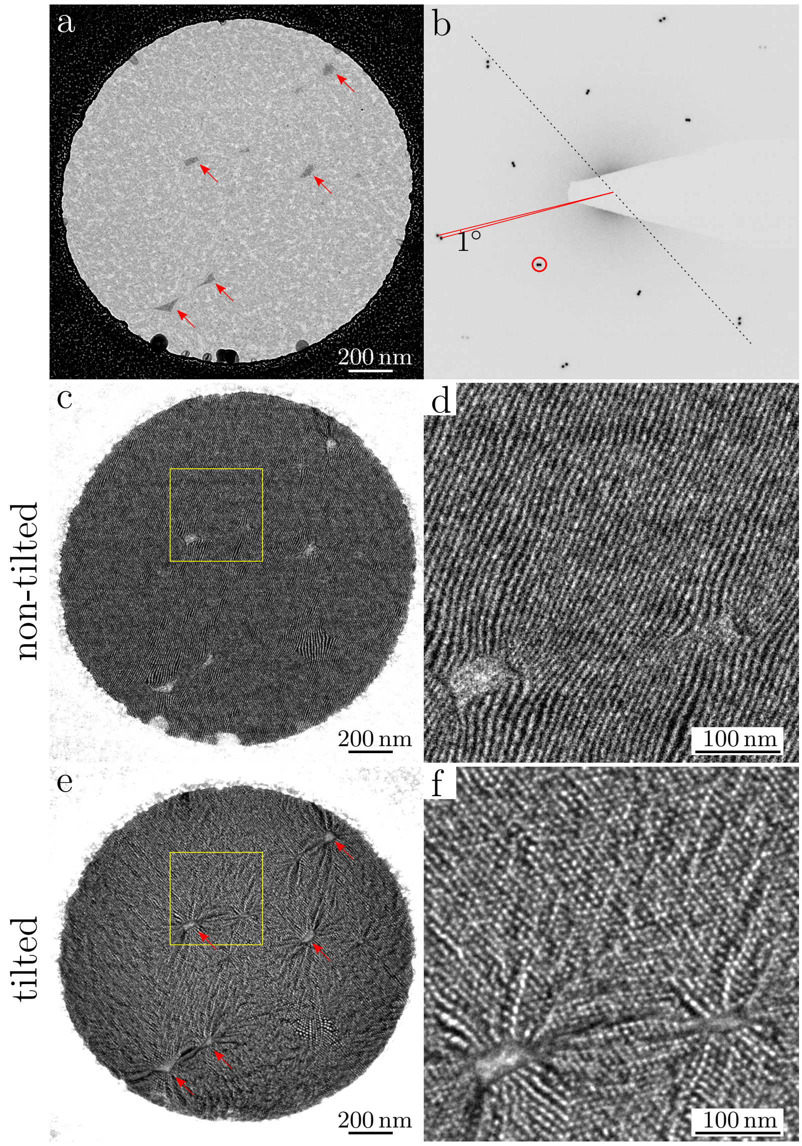

Figure 4.4: (a) BF image of the heterostructure freely suspended on a QF hole. The red arrows indicate some aggregations of contaminants. (b) Electron diffraction pattern of the heterostructure from the suspended area in (a). The misalignment between the two crystals is 1°. With reference to dark field imaging (c–f), the red circle marks the position of the objective aperture and the dotted line indicates the tilt axis. (c,e) DF images of the same area as in (a), acquired with no sample tilt (c) and with a sample tilt of 16° (e). (d) and (f) show magnified views of the areas inside the yellow box in (c) and (e), respectively. The red arrows in (e) point to the same features as in (a). At these locations the moiré interference pattern is completely suppressed.

are interpreted as pockets of contamination trapped between the layers, as reported previously on the basis of cross-sectional TEM imaging [69]. At these locations, the two layers are separated by amorphous contamination and the diffraction conditions for moiré interference are suppressed. Indeed, the presence of the moiré in the DF TEM images indicates that most of the graphene/hBN interface is atomically clean. Therefore, the clearly visible homogeneously distributed contamination, similar to what is typically seen in TEM studies of graphene, must be on the outer surfaces of the heterostructure.

4.1.2 Experimental methods

Further investigation on this sample was performed in the NION UltraSTEM 100 operated at 60 kV. Fig. 4.5a shows an atomically resolved MAADF image of a small portion of the suspended heterostructure. In the range of scattering angles used here (∼60–120 mrad), regions where the atoms are precisely on top of each other appear brighter than the sum of the individual atoms as in HAADF images, because of non-linear effects that contribute to the formation of contrast in this intermediate range of scattering angles [70]. Indeed, as shown in fig. 4.6, in HAADF imaging (∼80–240 mrad) the intensity does not vary across the differently stacked regions, while the MAADF image shows a remarkable variation of intensity across the moiré unit cell. For this reason, and also because for light species as carbon the MAADF image has a better signal-to-noise ratio than the HAADF image, MAADF imaging was preferred over HAADF in this work.

There are three types of high-symmetry stacked regions labeled as AA (C atoms aligned with B and N atoms), AB (C atoms aligned with B atoms only) and AB' (C atoms aligned with N atoms only). The top view structure models of the three stacking types are schematically shown in fig. 4.5b–d. In fig. 4.5f–h the AA, AB and AB' regions are shown at higher magnification in red, cyan and green frames, respectively. A STEM simulation of the heterostructure, performed using the QSTEM software [54], is shown in fig. 4.5e and the AA, AB and AB' regions are shown at higher magnification in fig. 4.5i–k. Fig. 4.5l–n show the intensity profiles for each of the three regions along the yellow lines of fig. 4.5f–k for the experimental (solid line) and for the simulated (dashed line) case. The AA region can be identified already from its visual appearance, which is distinctly different from that of the AB and AB' regions (compare fig. 4.5f, i with fig. 4.5g, h, j, k). The AB and AB' regions can be distinguished by comparing the intensity modulation in the lattice, which is always stronger in the AB' region (where C and N are aligned, fig. 4.5n) than in the AB region (where C and B are aligned, fig. 4.5m). Hence, from the appearance and relative intensity variations (fig. 4.5l–n are plotted with the same intensity scale), it is possible to unambiguously associate each moiré spot to a specific stacking type.

A careful analysis of many regions across the sample reveals that the AB

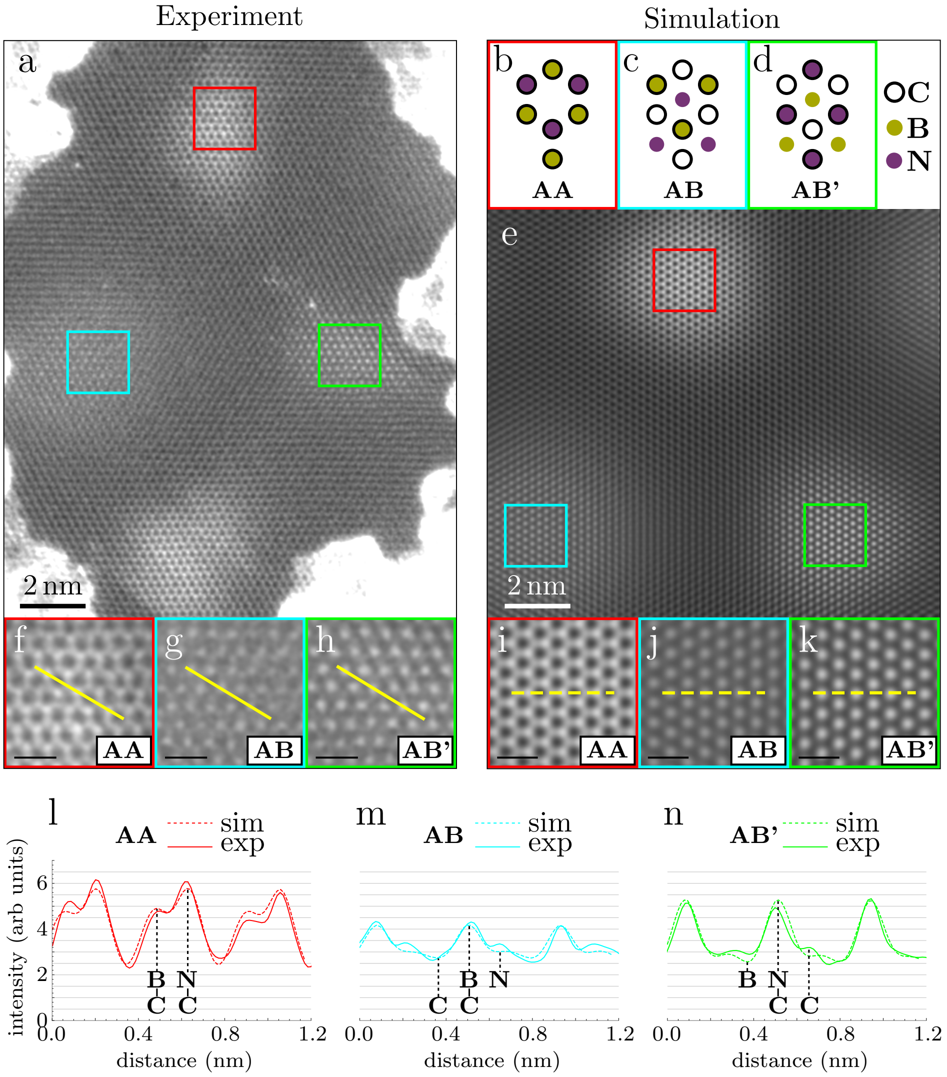

Figure 4.5: MAADF imaging. (a) Atomically resolved MAADF image of a portion of the heterostructure. Because of the contrast mechanism for medium angle scattering, high-symmetry regions appear brighter. The top-view structure models of the high-symmetry regions are shown in panels (b–d). The regions in the colored squares of panel a are shown at higher magnification in panels (f–h). (e) STEM MAADF simulation of the considered heterostructure. (i–k) Magnified views of the three high-symmetry regions of (e). (l–n) Gray value intensity profiles for the experimental (solid lines) and the simulated (dashed lines) case along the yellow lines in (f–k). Scale bars in panels (f–k) are all 0.5 nm.

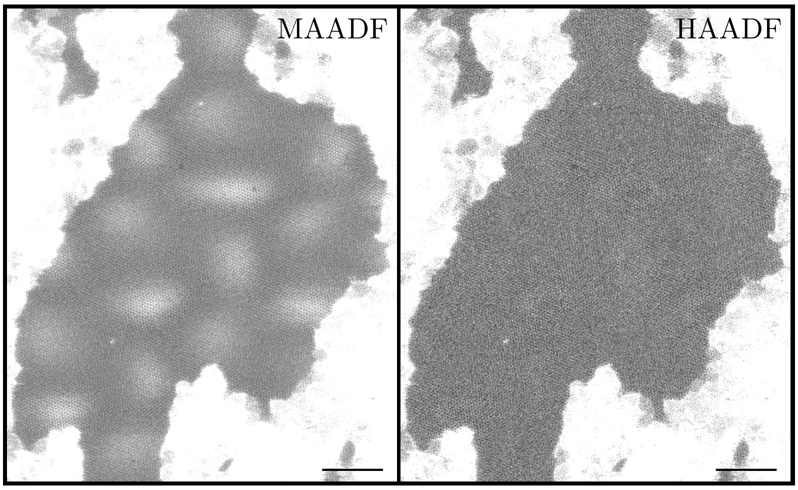

Figure 4.6: Comparison between MAADF (left) and HAADF (right) imaging of the same area of the heterostructure. The images shown are raw data and were recorded simultaneously. Scale bars are 5 nm.

stacked regions consistently appear larger than the AA and AB' regions. This can be clearly seen for instance in fig. 4.7a, where a MAADF image containing several moiré spots is presented (a black mask was used here to cover contaminated areas). The three different moiré regions were identified as explained above for fig. 4.5. Individual AA, AB and AB' regions are enclosed by red, cyan and green polygons respectively. The sides of the polygons are placed approximately along the lines of minimum intensity between two adjacent moiré regions. Already at a first glance, it is evident that the AB region is the largest of the three. Indeed, as drawn in fig. 4.7a, the AB region measures 55 nm^2, while the AA region is 34 nm^2, and the AB' region is 32 nm^2.

To get more insight into the local atomic stacking and to ultimately understand the reason behind the different sizes of the three moiré regions, the PADF detector that was introduced in sections 3.2 and 3.3 was employed to extract information on the preferential scattering direction of the electron beam. For every scanned pixel, the relation between recorded PADF image, preferential scattering direction and local atomic stacking is based on the following argument: for high-symmetry stacked regions, i.e. at the center of AA, AB and AB' spots, the heterostructure shows perfect in-plane isotropy and the electron beam will be elastically scattered along a cone around the axis of the primary beam. The corresponding PADF detected signal will therefore show symmetric illumination with respect to its center. However, when the probe hits the side of a moiré spot, where the two lattices are slightly off register, the electrons experience an anisotropic potential that results in the beam being predominantly scattered in one direction. Consequently, the recorded image will show asymmetric illumination. Examples of the locally obtained scattered intensity distributions are shown in fig. 4.7b, for selected points as drawn on the MAADF image of fig. 4.7a. The insets show the structure model of the bilayer at the considered positions. The six images show important differences: regions 1 and 5, respectively centered on the AA and on the AB stacked regions, produce strong isotropic scattering of the beam around the center of the detector, with the AA region being the stronger scatterer of the two (as can also be seen from MAADF images). Regions 2 and 4 are respectively selected slightly off the centers of AA and AB spots and in the corresponding scattering images the intensity is preferentially accumulated on one side of the detector. Finally, the center of mass of the detected intensity for regions 3 and 6 is at the center of the image, but the signal shows a two- and three-lobe geometry that mirrors the local symmetry of the corresponding regions. Since this signal is very sensitive to the local (projected) stacking of the two layers at each position, the comparison to simulated data from model structures allows to establish the 3D structure of the free-standing bilayer heterostructure.

To quantitatively evaluate the preferential scattering direction the recorded dataset was analyzed with the ACOM method introduced in section 3.2. Examples of the calculated r and φ values of the scattered intensities for the six considered regions are noted in fig. 4.7b. Here, the position of the ACOM is also indicated by a red cross in each image, showing that only for regions 2 and 5 the ACOM is significantly displaced from the center of the detector (in fig. 4.7b the radial coordinate of the cross was exaggerated by a factor of 20). Fig. 4.8a shows a map of the same sample region of fig. 4.7a obtained by assigning to each pixel the value of r of the corresponding diffracted intensity encoded by a gray scale, where black and white colors correspond, respectively, to $r = 0$ and $r = r_{max}$. As expected from the considerations above, the map shows minima at the center of the moiré spots, indicating perfect symmetry, and maxima around these points, where the stacking offset produces prevalent electron scattering in one direction. Note that points halfway between two adjacent moiré spots are also dark. This is because in these regions the atomic stacking is perfectly halfway between two high-symmetry configurations and the coordinate r of the ACOM goes to zero (as, for instance, for regions 3 and 6 of fig. 4.7b). Fig. 4.8b includes information on the angular direction of the preferential scattering, where the coordinate φ is encoded by the color (see fig. 4.8e for graphical explanation of the color code). It is interesting to observe how the scattering direction depends on the angle around the center of a moiré spot, spanning a range of 2π around each. For comparison, STEM simulations based on a structure model consisting of a flat graphene/hBN heterostructure were performed. Saving the simulated exit waves (ronchigrams) for each pixel allows to treat the computed dataset in the same way as its experimental counterpart. Fig. 4.8c and 4.8f show the results of this simulation. The experimental and the simulated maps show a qualitative agreement but important differences become evident when comparing the relative sizes of the

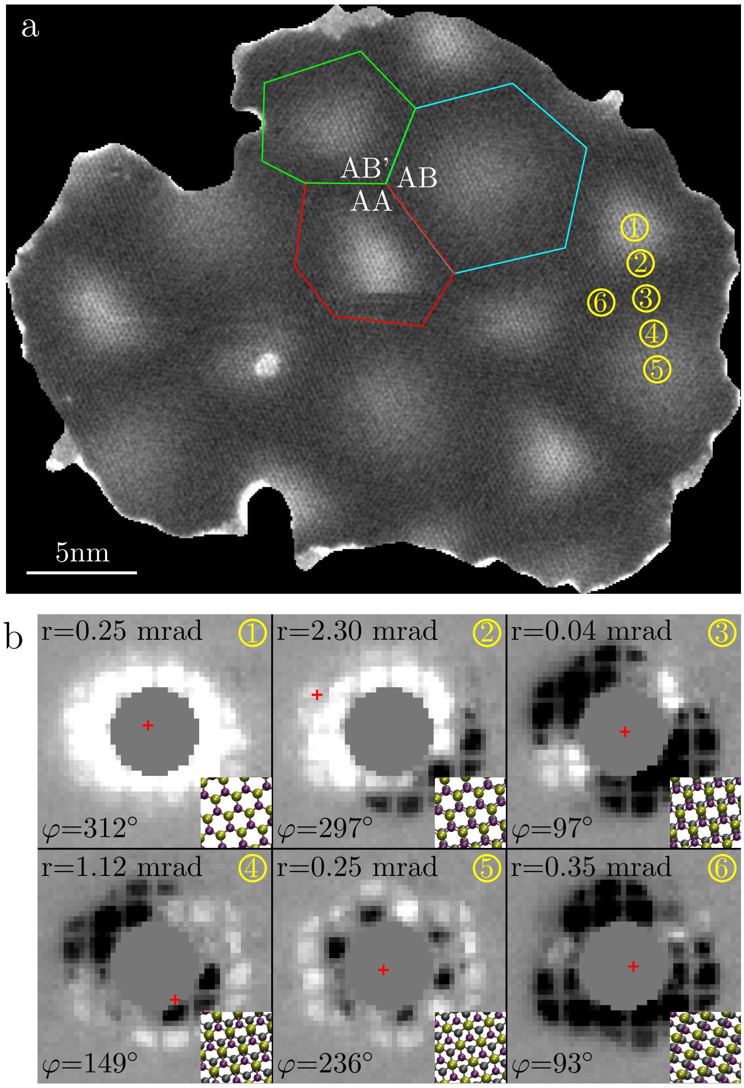

Figure 4.7: (a) MAADF image of an area of the sample containing several moiré regions. The AB stacked region (enclosed in the cyan polygon) is found to be consistently larger than the AA (in red) and the AB' (in green) regions. (b) From the indicated regions (1–6) in panel (a), the scattering intensity distributions are shown as the difference between a 10×10 pixels area binned signal and a reference signal that is obtained as an average of all recorded images (excluding those corresponding to contamination). Insets illustrate the local relative lattice offsets that are associated with the asymmetric scattering intensity (carbon is gray, boron is yellow and nitrogen is purple). The red cross indicates the position of the ACOM in each image (the radial coordinate was exaggerated by a factor of 20). The r and φ coordinates of the ACOM position are also indicated for each image.

moiré spots. The black dotted lines in fig. 4.9a, b and c are calculated by averaging 7 to 12 intensity profiles of fig. 4.8a along straight paths connecting adjacent moiré spot centers. Three such paths are indicated in fig. 4.8a by colored dashed lines and they connect AA to AB (red), AA to AB' (yellow) and AB to AB' (green). The position of the central minimum in each of these plots, which marks the transition between two adjacent stacking types, is significantly different for the experiment and the simulation based on the rigid model (orange solid lines). This disagreement can only be corrected by considering a new structural model for the simulation that allows for in-plane strain of the two crystals and/or out-of-plane distortion of the heterostructure. The flat and rigid graphene/hBN model has therefore to be abandoned in search of a more realistic atomic structure.

4.1.3 Computational methods

A relaxed graphene/hBN model was computed by energy minimization using a combination of density functional theory (DFT) calculations and empirical potentials as explained in the following. Note that the combination of the two methods is a key point here, since full-scale DFT would be computationally prohibitive for a moiré unit cell consisting of ~16000 atoms, while empirical potentials have not been reported so far for the case of graphene on hBN. In order to determine the energy landscape of graphene on an hBN monolayer the same approach as in ref. [71] was followed, where several DFT methods for simulating the vdW interaction between the two layers were examined. For this work, the vdW-DF2 method [72, 73] was chosen. A supercell consisting of eight atoms (four carbon, two boron and two nitrogen atoms) was constructed and the interaction energy between the two layers was calculated as:

$$E_{vdW} = E_{\infty} - E_{d_0}$$

where E_{∞} and E_{d_0} are the total energies of the supercell at infinite and at the equilibrium interlayer distances, respectively. The blue dots of fig. 4.10a show the calculated values of E_{vdW} for the three high-symmetry stacking types and for other intermediate disregistry configurations. The plot clearly shows that the AB type is by far the most energetically favorable stacking type, followed by AB' and finally by AA. This result is in agreement with existing literature [71, 74] (note that in ref. [71] the AB and AB' structures were inadvertently misidentified, with their names exchanged). To extend the calculation to the entire moiré unit cell, the vdW interaction between the layers is described by a Morse potential in the form:

$$V(r) = D_e(e^{-2\alpha(r-r_e)} - 2e^{-\alpha(r-r_e)})$$

where D_e is the value of the potential at the equilibrium interlayer distance r_e and α sets the width of the potential. The numerical values of the parameters

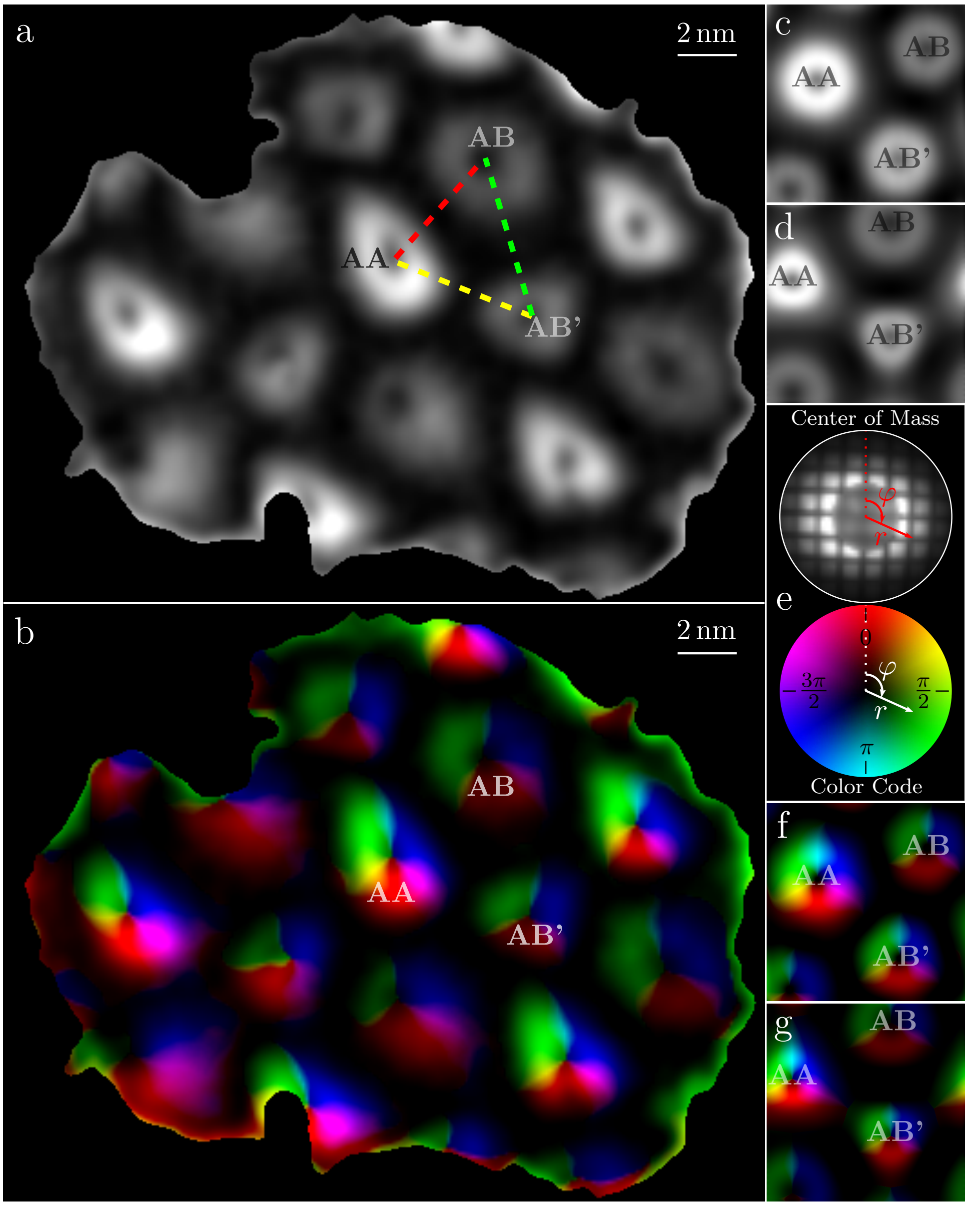

Figure 4.8: Directional scattering analysis. (a) Radial (r) map of the same area of fig. 4.7a. The gray scale ranges from black ($r = 0$) to white ($r = r_{max}$). (b) Radial and angular ($r + \varphi$) map of the same area in (a). The color of each pixel is assigned based on the position of the ACOM by a one to one correspondence that is graphically explained in (e). (c) Simulated r map and (f) $r + \varphi$ map based on the rigid model. (d) Simulated r map and (g) $r + \varphi$ map based on the relaxed model. Note that translations and rotations of the maps must be allowed when comparing them to each other.

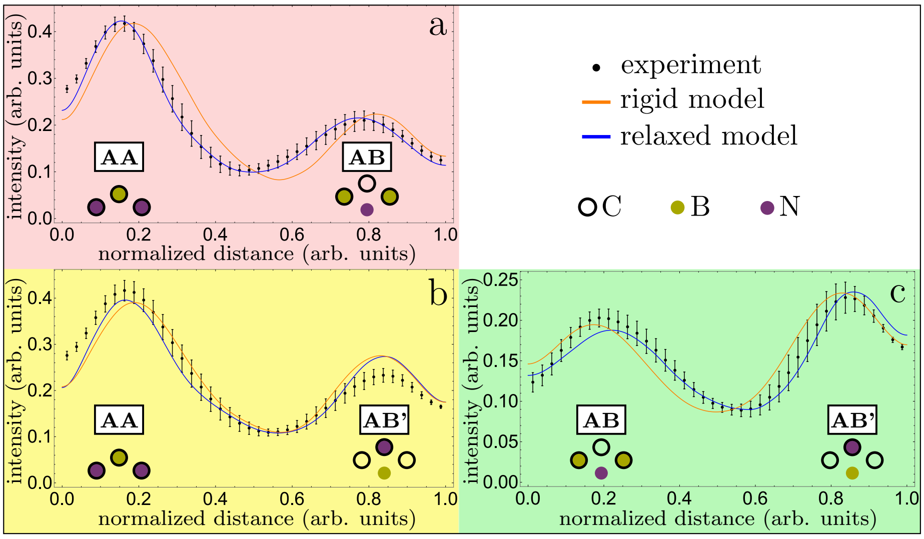

Figure 4.9: Intensity profiles of the radial map of fig. 4.8a along paths connecting AA to AB (a), AA to AB' (b) and AB to AB' (c). The black dotted lines are the experimental profiles (obtained by averaging 7 to 12 individual profiles of fig. 4.8a), the orange solid lines are the simulated profiles of the rigid model (fig. 4.8c) and the blue solid lines are the simulated profiles of the relaxed model (fig. 4.8d).

were adjusted so that the interlayer interaction agrees with the DFT results, leading to $D_e^{CB} = 2.9\,\text{meV}$, $\alpha^{CB} = 2.08\,\text{Å}^{-1}$ and $r_e^{CB} = 3.86\,\text{Å}$ for the C–B interaction and to $D_e^{CN} = 8.3\,\text{meV}$, $\alpha^{CN} = 2.54\,\text{Å}^{-1}$ and $r_e^{CN} = 3.84\,\text{Å}$ for the C–N interaction. With these values, an excellent match could be obtained as shown by the red dots in fig. 4.10a. The C–C and B–N interaction is treated using many-body lcbop [75] and Tersoff [76, 77] potentials, respectively, leading to a lattice mismatch of ∼1.6%. Both potentials are implemented in the code *large-scale atomic/molecular massively parallel simulator* (LAMMPS) [78, 79]. For a moiré unit cell of graphene on hBN (0° misalignment), 65×65 unit cells of graphene on 64×64 unit cells of hBN are needed to keep the periodic boundary conditions, totaling 16642 atoms. The structure with 1° of rotational misalignment is avoided as one would need to consider millions of atoms to properly model that structure. The total potential energy is minimized by relaxing both layers without applying any constraint until the forces are below $10^{-6}\,\text{eV}\,\text{Å}^{-1}$.

The initial and the fully relaxed models are presented in fig. 4.10b and c, respectively, with the three stacking types marked. The relaxed model visibly distorts in the out-of-plane direction, forming a wavy structure with a periodicity that matches the moiré superlattice. In particular, the AB region is found at a smooth bulge having the concavity on the graphene side, while

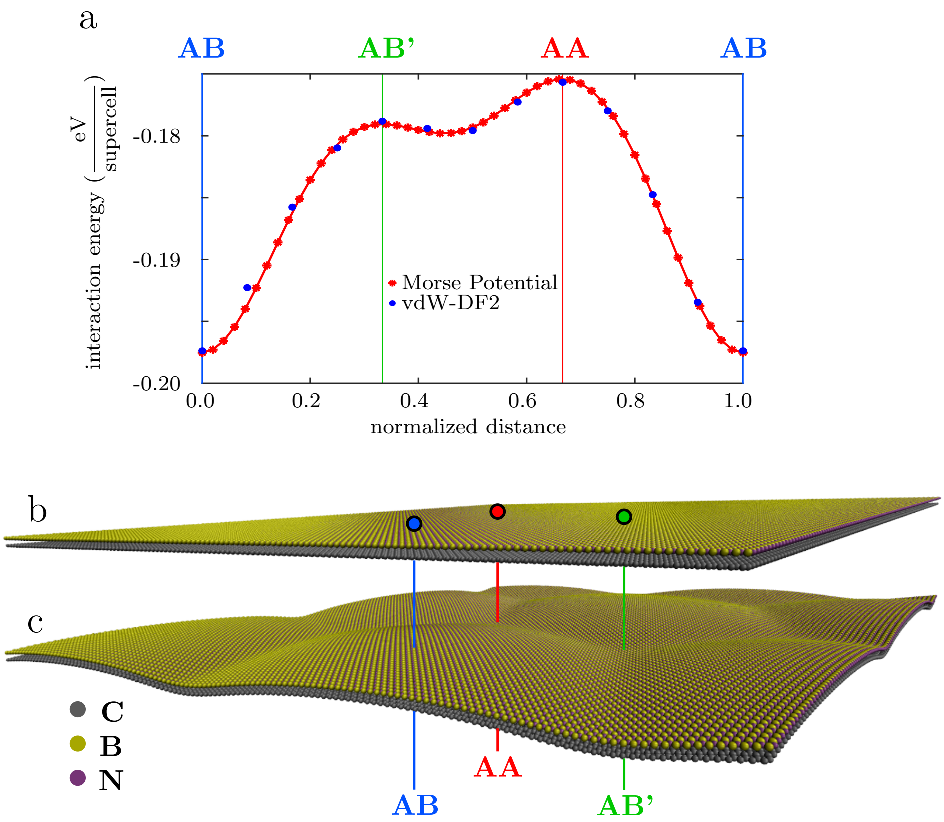

Figure 4.10: (a) Interlayer interaction energy plot per supercell (four carbon, two boron and two nitrogen atoms). The blue dots represent the values obtained by DFT calculations for different stacking configurations, while the red dots indicate the shape of the Morse potential, whose parameters were optimized to fit to the DFT points. (b) Rigid structure model of the graphene/hBN bilayer before relaxation. (c) Structure model of the graphene/hBN bilayer after full relaxation. The relaxed model visibly distorts in the out-of-plane direction.

at AA and AB' regions the structure has sharper kinks with the concavity facing the hBN side. The calculated topography map is shown in fig. 4.11a, where the z height value is taken at half distance between the two layers. The total amplitude of the corrugation is $\sim 8.5\,\text{Å}$ for each layer. The results of the relaxation are in good agreement with the theoretical prediction of ref. [80].

4.1.4 Discussion

STEM simulations based on the relaxed model were performed and the resulting r and $r + \varphi$ maps are shown in fig. 4.8d and g, respectively. Although the rippling changes the positions of the moiré spots, the distances and relative angles between them do not change. Rather the main change to the moiré introduced by the rippling is the size and shape of the spots. In particular the rippling expands the AB region and causes the AA and AB' regions to become more triangular, in much better agreement with the experiment. The intensity profiles for the map of the relaxed structure are shown in fig. 4.9a–c as blue solid lines. In fig. 4.9a and c the experimental and the simulated data based on the relaxed model now show excellent agreement, with both central minima being accurately reproduced. In other words, the plots from AA to AB (fig. 4.9a) and from AB to AB' (fig. 4.9c) allow to clearly distinguish the rigid, flat model from the relaxed, rippled structure.

Along the line from AA to AB' (fig. 4.9b), no significant difference between the flat and rippled model can be identified. This is not surprising because there is neither significant out-of-plane deformation nor in-plane lattice distortion (discussed further below) along this particular line in the relaxed structure. Also note that, while the positions of the maxima and minima in the profiles for the experiment and the simulation now match extremely well, the maximum amplitudes of the r values still deviate slightly (in fig. 4.9b and c the simulations slightly underestimate the amplitude near AA and AB, while they are overestimated near AB'). This cannot be due to inaccuracies in the structure model, because distortions in the membrane shape and layer alignment would shift the positions of maxima and minima, but not affect their amplitude. Nonlinearities of the detector, aberrations in the electron optics between sample and detector, or remaining inaccuracies in modeling of the scattering might be the reason. It is important to point out that none of these effects would affect the locations of the minima in r, since the minima reflect special cases in the symmetry of the projected structure.

At this point, it is worth to briefly comment on how the ACOM analysis would compare to analyzing the MAADF intensity: each of the ACOM profiles as discussed above features two maxima and three minima, making the position of the central minimum very sensitive to the transition point between adjacent stacking types. A profile through the MAADF intensity, on the other hand, only has two side maxima with a single broad central minimum, which makes it difficult to distinguish tiny differences in the stacking transition.

The superior match between the experiment and the relaxed rippled model indicates that the latter is far more realistic than the flat model. The strain maps for the two layers in the relaxed structure are also computed. As shown in fig. 4.11b, the interatomic distances for both graphene and hBN are not constant but modulated with a periodicity matching the moiré wavelength. In particular, graphene tends to stretch at AB regions and compress along lines connecting AA to AB' regions, while hBN appears mostly unstrained, with small local stretching accumulated at AA and AB' regions. From the strain distribution in each layer the lattice mismatch is extracted and shown in the map of fig. 4.11c. Here it can be clearly seen how the two layers attempt to minimize the mismatch at the AB regions, while at AA and AB' the mismatch is significantly larger. This behavior can be explained by taking into account two conflicting effects, as already discussed in ref. [60]: as demonstrated earlier, AB is the most energetically favorable stacking type and the two crystals will attempt, by a combination of stretching and compression in each layer, to extend laterally this favorite stacking and thus to gain in vdW energy, at the expense of the AA and AB' regions that will necessarily shrink. This behavior is in contrast to the elastic energy of the crystals' lattices, which scales with the square of the strain and therefore attempts to restore the intrinsic lattice constants. The equilibrium is reached when these two competing forces cancel out. Note that the smallest value of lattice mismatch is $\sim 1.2\%$, indicating that the two lattices are never found in a completely synchronous state.

4.1.5 Conclusions

In conclusion, I have presented here a TEM study of a free-standing 2D vdW heterostructure consisting of a well aligned bilayer of graphene on hBN. DF imaging in a conventional TEM confirms that the contaminants trapped between the two layers are squeezed into few isolated pockets, leaving most of the heterostructure with an atomically clean interface. A direction sensitive acquisition mode for the scattered electron beam of a STEM was developed and employed to extract in-depth information on the local atomic stacking. Comparison with STEM simulations based on a relaxed model indicates that the heterostructure corrugates in the out-of-plane direction, with an undulation having the same periodicity as the moiré pattern and a total amplitude (in each layer) of $\sim 8.5\,\text{Å}$. This work shows that depending on lattice mismatch and stacking misorientation, suspended heterostructures, usually regarded as pure 2D materials, should be effectively considered as 3D objects, with vdW interlayer forces playing a key role in determining the in-plane strain and out-of-plane deformation of each layer.

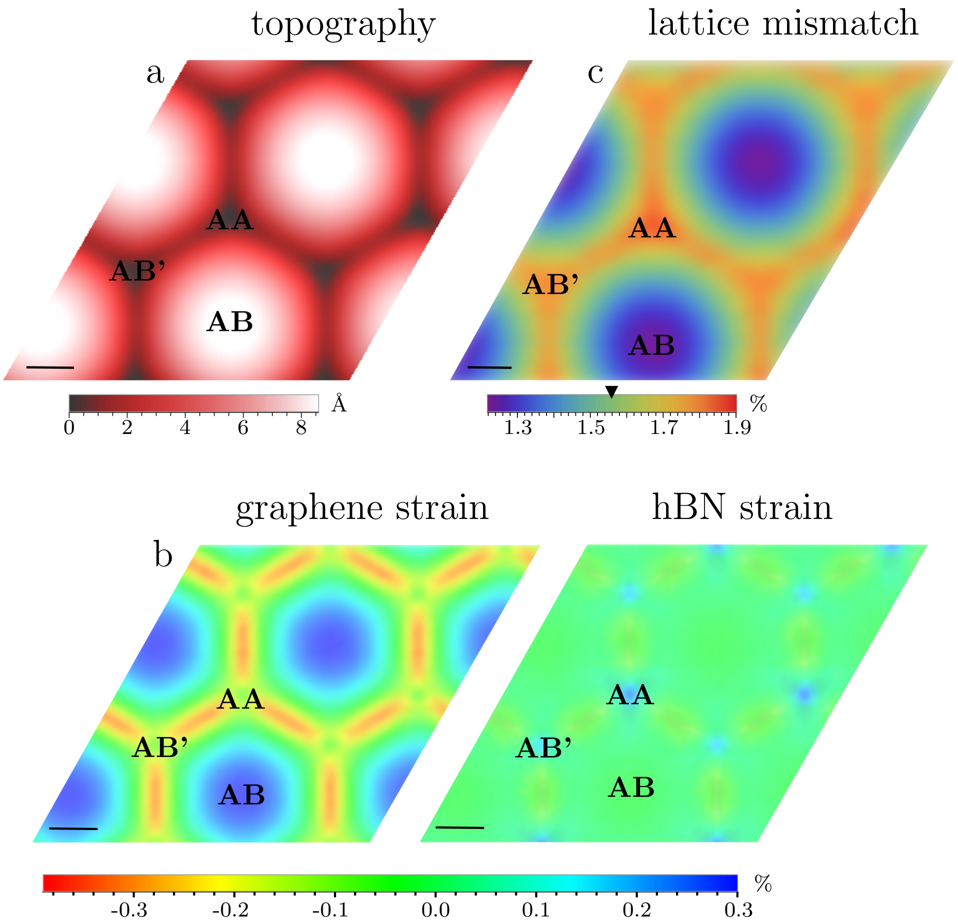

Figure 4.11: Calculated maps for the relaxed heterostructure. (a) Topography map showing the out-of-plane deformation of the heterostructure. The shown values are taken at half distance between the two layers. (b) In-plane strain maps of graphene (left) and hBN (right). (c) Lattice mismatch map. The black arrow next to the color bar indicates the initial lattice mismatch between the two crystals before the relaxation. All scale bars are 2 nm.

4.2 Weighing atoms by high-angle electron scattering. Part 1: theory

The content of this section is based on entry 7 of the List of publications.

4.2.1 Introduction and basic principles

As discussed in section 2.1.2, the atomic-size probe of the electron beam in a STEM can provide a wealth of information via the large variety of signals that can be recorded as a function of probe position. Most of these signals are, in some way, connected to the atomic number Z of the atoms, or to the electronic structure of the sample. To date, no measurement technique in the STEM has been able to discern atoms based on their atomic weight, rather than on their atomic number. That means, for instance, that different isotopes of the same species cannot be distinguished with the current detection techniques. If that would be possible, the capability to weigh atoms, and identify isotopes, would combine the powerful tools of isotope labeled chemistry with the atomic-resolution analysis in a scanning transmission electron microscope.

As an example for motivation, consider the growth of isotope labeled graphene[2] [81, 82] from benzene molecules [83]: conceivably, the carbon rings of the molecule might disassemble during synthesis and then reassemble into the graphene sample (as schematically represented in fig. 4.12, left) or, alternatively, might stay connected as molecules (or fractions) which assemble into the 2D honeycomb lattice (as in fig. 4.12, right). Synthesis from a mixture of isotopes, followed by atomic-resolution isotope-sensitive imaging, would shed unprecedented insight to the growth mechanism.

In this section, I explore theoretically the possibility of distinguishing between atomic masses in a STEM by high-angle elastic scattering of electrons. To this end, consider the electron-nucleus Rutherford scattering geometry shown in fig. 4.13, where, in the general case, the target particle is not at rest but moves with velocity $\boldsymbol{V}$. The electron with initial momentum $\boldsymbol{p_e^i}$ and kinetic energy E_e^i is deflected by the positively charged nucleus of initial momentum $\boldsymbol{p_n^i}$ and kinetic energy E_n^i to an angle θ. After the interaction, the electron has final momentum $\boldsymbol{p_e^f}$ and kinetic energy E_e^f, while the nucleus has final momentum $\boldsymbol{p_n^f}$ and kinetic energy E_n^f. During the interaction, a tiny amount of energy $E_t = E_e^i - E_e^f$ is transferred between the electron and the nucleus. By imposing the conditions for conservation of momentum and energy, one can write an expression for E_e^f in terms of the known initial energy

---

[2] Isotope labeled CVD growth will be discussed in section 4.3.1

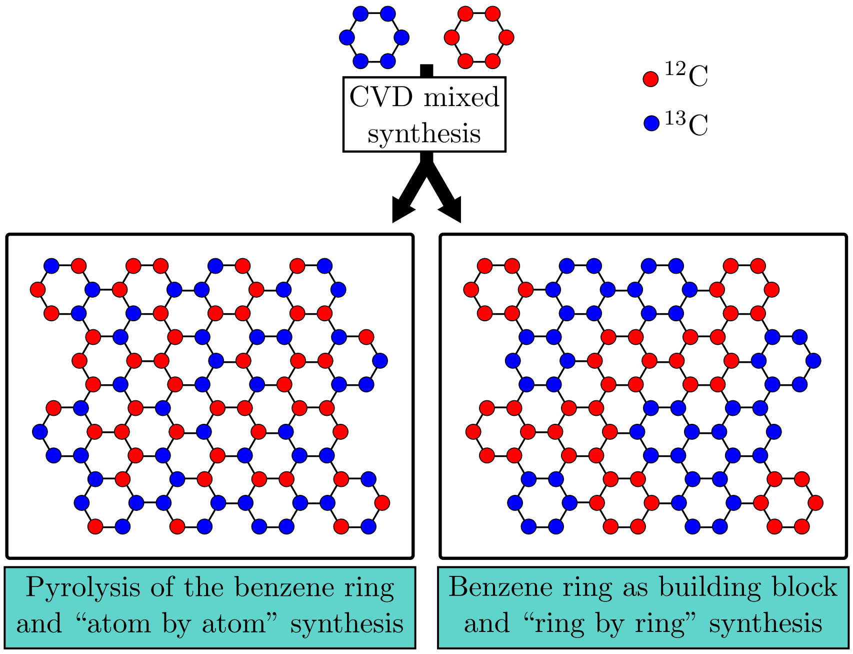

Figure 4.12: Example motivation for isotope sensitive imaging of graphene as a tool to understand synthesis mechanisms or chemical modifications.

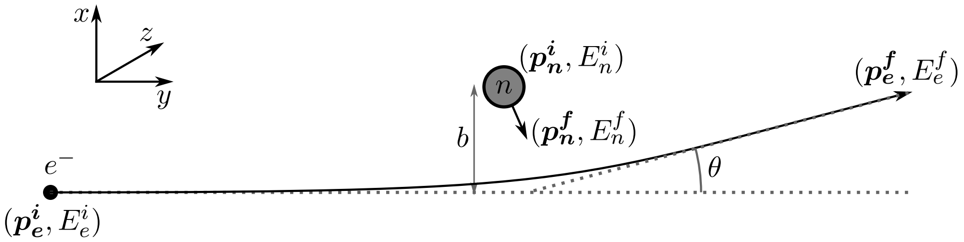

Figure 4.13: Schematics of Rutherford scattering of a fast electron on a positively charged nucleus. b is the impact parameter. The reference system, as used in the calculations, is also shown.

and momentum of both particles as:

$$E_e^f = \frac{E_e^i(M - m + 2m\cos\theta) - 2\sqrt{mME_e^iE_n^i}\left[\frac{V_x}{|\boldsymbol{V}|}\sin\theta + \frac{V_y}{|\boldsymbol{V}|}(\cos\theta - 1)\right]}{M + m} \tag{4.1}$$

where m and M are, respectively, the rest masses of the electron and of the nucleus. Note that the z component of the velocity $\boldsymbol{V}$ does not appear in eq. 4.1. This is because for a two-body scattering event the motion of both particles always lies on a plane, allowing a full description of the problem using a 2D reference system.

The first observation that can be made on eq. 4.1 is that for the trivial case of $\theta = 0$, the expression simplifies to $E_e^f = E_e^i$, which simply means that there is no interaction between the particles and the electron continues on its initial trajectory and conserves its energy. Consider now the case where $\theta \neq 0$ but $E_n^i = 0$, meaning that the target nucleus is initially at rest. In this case the second term of the numerator is zero and, as follows from the first term of the numerator, the final energy of the electron decreases as the scattering angle increases. The physical meaning of this behavior can be explained as follows: the smaller the impact parameter b is, the stronger the Coulombian interaction between the particles will be. Consequently, the electron will be scattered to higher angles and a larger amount of energy will be exchanged with the nucleus. Finally, in the most general case ($\theta \neq 0$ and $E_n^i \neq 0$), the second term of the numerator will also affect the transferred energy depending on the initial velocity of the nucleus. Importantly, eq. 4.1 shows that E_e^f depends on the mass of the scattering nucleus M. Since m and E_e^i are known, θ is the (known) detection angle and $\boldsymbol{V}$ is zero in average (the nuclei do not migrate inside the sample), then the mass M of the scattering nucleus can be deduced by measuring E_e^f. Unfortunately, the transferred energy E_t becomes increasingly small, and thus more difficult to detect experimentally, as the difference between the masses of the particles increases. It follows from equation 4.1 that if m becomes negligible in respect to M, then $E_e^f = E_e^i$ regardless of the scattering angle, and no information on M can be obtained. For the case of a carbon atom $\frac{M}{m} \approx 2 \times 10^4$ and therefore the transferred energy is very small. Nevertheless, an accurate measurement of the electron energy loss should provide a method to effectively "weighing" individual atoms and thus to distinguish between isotopes in a sample.

The scattering event described above, also called electron-atom Compton scattering (EACS), was employed by Vos et al. as an experimental technique to observe the motion of the nuclei in solids or molecules, and is an electron analog for neutron Compton scattering [84]. Below, I explore the possibilities of EACS measurements in connection with a spatially resolved probe, and in scattering geometries that might be achieved in a STEM. I consider scattering to large angles with the primary beam focused to smallest dimensions, as is possible in STEM experiments. Since the column geometry of existing instruments will allow electrons scattered up to ∼10° (175 mrad) to pass through the post-sample optics, special consideration is given to the "smaller" range of high-angle scattering. The primary beam of the STEM would ideally be focused to a single atom of the sample, which is possible with 2D materials. Then, electrons scattered to low and high angles are simultaneously recorded in the spectrometer; i.e., the diffraction plane is condensed in one direction, energy-dispersed, and recorded on a 2D detector, as described in section 3.3. The obtained energy-momentum map would be recorded at every point of the scanned primary beam, thus creating a 4D dataset. Since the incoming beam must be convergent, there will inevitably be an uncertainty in the measured scattering angle, i.e., spectra will be "washed out" in the angle or momentum direction.

I show calculations of the electron energy loss of elastic scattering events for the two stable isotopes of carbon (^{12}C and ^{13}C), hydrogen as the lightest, and gold as a common heavy element. The energy of the incoming beam is assumed to be $E_e^i = 60\,\mathrm{kV}$ and the relativistic effects are ignored for this low beam energy, as the correction factor

$$\gamma = \frac{1}{\sqrt{1 - \dfrac{v^2}{c^2}}} \approx 1.11$$

is close to 1. Eq. 4.1 provides the energy loss for a given velocity of the nucleus. However, within a typical measurement interval the nucleus changes its velocity continuously and therefore the expected electron energy loss will be a continuous distribution rather than one single value. To calculate the EELS distribution the nucleus velocity $\boldsymbol{V}$ has to be integrated over all possible values. Within the Debye model, the mean square velocity of an atom of mass M can be calculated from the Debye temperature θ_D and the temperature T as [85]:

$$\overline{|\boldsymbol{V}|^2} = \frac{9K_b}{8M}\theta_D + \frac{9K_bT}{M}\left(\frac{T}{\theta_D}\right)^3 \int_0^{\theta_D/T} \frac{x^3}{e^x - 1} dx \tag{4.2}$$

and I consider a 2D Gaussian velocity distribution given by:

$$P(V_x, V_y) = \frac{1}{2\pi\sqrt{\overline{V_x^2}}\sqrt{\overline{V_y^2}}} e^{-\left(\frac{V_x^2}{2\overline{V_x^2}} + \frac{V_y^2}{2\overline{V_y^2}}\right)} \tag{4.3}$$

Here, $P(V_x, V_y) \cdot dV_x dV_y$ is the probability of finding the nucleus within an interval dV_x,dV_y around a given velocity V_x,V_y and $\overline{V_x^2}$ and $\overline{V_y^2}$ is the mean square velocity in the respective direction (eq. 4.2 is applied for each direction, using an orientation-dependent Debye temperature for the case of anisotropic materials). Note that since E_e^f (eq. 4.1) does not depend on V_z the integration over the probabilities is only required in the two dimensions of V_x and V_y.

4.2.2 Numerical calculations

To calculate the EELS distribution one would first need to write an expression for $\boldsymbol{V}$ as a function of E_e^f by inverting eq. 4.1 and then substitute the obtained expression into eq. 4.3 to find the probability distribution as a function of the transferred energy E_t. Unfortunately, this cannot be solved analytically and therefore a numerical evaluation is necessary. The problem can be restructured as follows. The probability of finding the electron at a given scattering angle θ with energy loss between $\tilde{E}_t(\theta)$ and $\tilde{E}_t(\theta) + dE_t$ is given by:

$$P(\tilde{E}_t, \theta) dE_t = \int dV_x dV_y \delta(E_t(\theta, V_x, V_y) - \tilde{E}_t) \cdot P(V_x, V_y) dE_t \tag{4.4}$$

i.e., one would integrate all probabilities for combinations of velocities that result in the considered transferred energy $\tilde{E}_t(\theta)$. I consider the nucleus to have a velocity between $\pm 4\sigma = \pm 4\sqrt{\overline{V_{x,y}^2}}$, which ensures that more than 99.99% of all possible velocities are accounted for. The probability for finding the electron within an interval ΔE at an energy loss $\tilde{E}_t$ and scattering angle θ can be computed through numerical evaluation of eq. 4.4 as:

$$P(\tilde{E}_t, \theta) = \sum_{V_x, V_y \text{ } with \text{ } \tilde{E}_t \leq E_t(\theta, V_x, V_y) \leq \tilde{E}_t + \Delta E} P(V_x, V_y) \tag{4.5}$$

i.e., summing the probabilities of all velocities that would result in a transferred energy within a specified range $\tilde{E}_t \leq E_t(\theta, V_x, V_y) \leq \tilde{E}_t + \Delta E$. The temperature is assumed as $T = 300\,\mathrm{K}$ in all calculations.

The results of these calculations can be visually displayed by assigning to each element of the probability matrix a gray-scale color proportional to its value. In this way, fig. 4.14a and b show two maps calculated for ^{12}C, respectively in the 0°–180° and 0°–12° range, displayed to the full gray-scale range at each scattering angle. The red solid line indicates the position of the peak in the simulated spectrum, while the red dashed line shows the FWHM broadening of the spectra.

For a quantitative analysis, the strong dependence of detection probability from the scattering angle must be included in the calculation. The Rutherford scattering cross section is adequate for the intermediate range of scattering angles (beyond ∼4°) that are of main importance here [86]. The number of

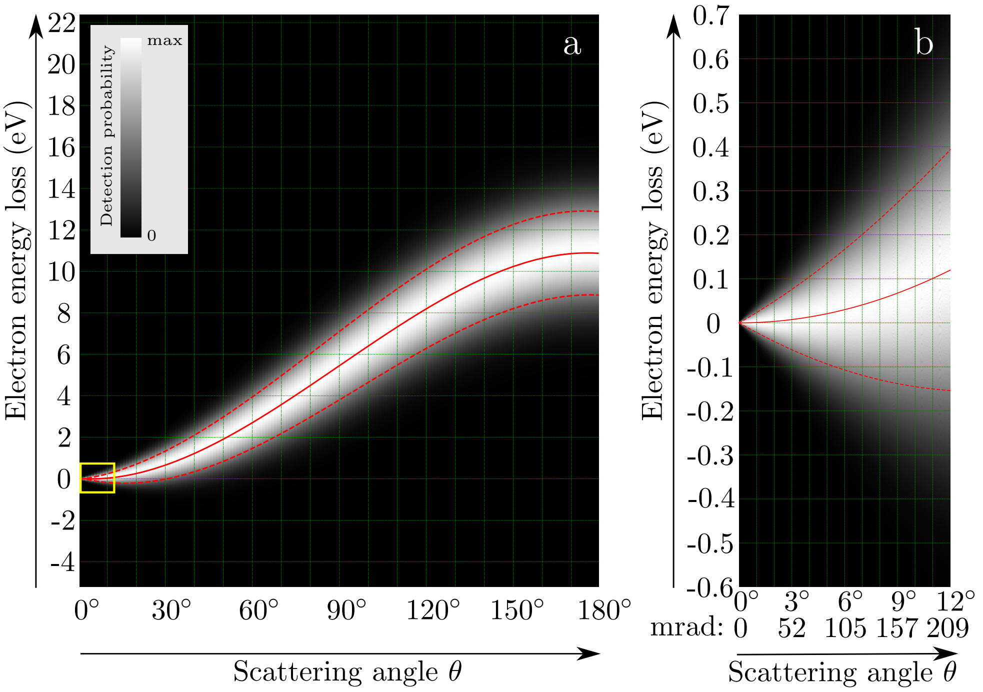

Figure 4.14: Detection probability map as a function of electron energy loss and scattering angle, shown here for the case of ^{12}C. The gray-scale range is adjusted for every scattering angle between black (zero) and white (max). The solid and dashed red lines show respectively the center and FWHM of a Gaussian fit to a vertical profile at each angle. (a) Full range 0°–180°. (b) Close up on the range indicated by the yellow box in (a) (calculated at a higher precision).

electrons ΔN scattered in the interval θ to $\theta + \Delta\theta$ is given by:

$$\Delta N = N d \pi \left(\frac{6e^2}{8\pi\varepsilon_0 E_e} \right)^2 \frac{\cos\left(\frac{\theta}{2}\right)}{\sin^3\left(\frac{\theta}{2}\right)} \Delta\theta \tag{4.6}$$

where N is the primary dose and d is the density of scattering centers. Including this effect, the map for ^{12}C changes as shown in fig. 4.15. Note that the number of scattered electrons decreases dramatically with the angle, spreading over several orders of magnitude in the 0°–12° range. For this reason, fig. 4.15 requires a logarithmic display. It should also be pointed out that eq. 4.6 implies an integration over an annular aperture with an angle from θ to $\theta + \Delta\theta$; a round aperture offset from the optical axis would only capture a small part of the scattered electrons.

For gold, the root mean square (rms) velocity was assumed to be isotropic and was calculated from the Debye temperature of 170 K [87], as 196 m s^{-1}.

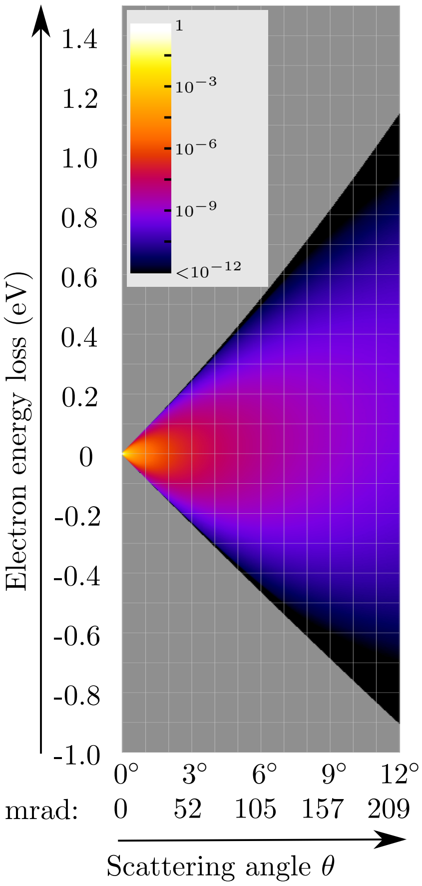

Figure 4.15: Probability of detecting the scattered electron, taking into account the Rutherford scattering cross section for each scattering angle. Note the logarithmic color scale, which indicates the rapid decay of intensity with higher scattering angle.

For carbon ^{12}C, a graphene sample is assumed, where the in-plane and out-of-plane Debye temperatures taken from [88] are respectively 2300 K and 1287 K, leading to rms velocities of $1349\,\mathrm{m\,s^{-1}}$ and $1050\,\mathrm{m\,s^{-1}}$ respectively. For ^{13}C graphene, the Debye temperature of ^{12}C graphene is rescaled, considering that for a mass-spring model it scales as $\theta_D \sim \sqrt{c/m}$ where c is the spring constant and m is the mass. Also for hydrogen, in shortage of a model compound, a rescaled Debye temperature of graphene is used, assuming that the spring constant is 1/3 of that for carbon (one bond instead of three), while mass is obviously 1/12. It must be noted that, in any case, these approximations are only aimed at getting an order-of-magnitude estimate on the rms velocity of the atomic vibrations, and should be replaced by more accurate calculations. Even for different phases of the same element (carbon), the rms velocity of the atoms varies significantly, according to the Debye model: taking the Debye temperatures for amorphous carbon, graphite out-of-plane, graphite in-plane and diamond as 337 K, 950 K, 2500 K and 1860 K [89], respectively, the room temperature rms velocities are, according to eq. 4.2, 813, 951, 1403, and $1222\,\mathrm{m\,s^{-1}}$. The broadening of the profiles in the model is proportional to these velocities, and hence, amorphous carbon should display approximately a half as wide broadening as graphene. Using the rms velocity of amorphous carbon, the calculation well reproduces the measured curve of ref. [84]. The velocities are sampled with steps from $10\,\mathrm{m\,s^{-1}}$ (gold) to $200\,\mathrm{m\,s^{-1}}$ (hydrogen). The calculations in the 0°–180° range were performed with angular steps of 1° while the range 0°–12° was calculated with higher precision with angular steps of 0.05°.

Fig. 4.16 shows the calculated electron energy loss for different elements and isotopes as a function of scattering angle, respectively in the 0°–180° and 0°–12° range. This is done the same way as for fig. 4.14a and b, this time omitting the whole map and only showing the peak position (solid line) and the FWHM (dashed lines) for each species. The first noticeable difference between the considered elements is the different energy loss ranges. This is a direct result of the different atomic masses, resulting in electrons to transfer a larger amount of kinetic energy to lighter nuclei than to heavy ones, as discussed in section 4.2.1. Another remarkable difference between the species taken into account is that the broadening of the energy loss at a given scattering angle is much larger for lighter atoms and it progressively decreases for heavier ones. The reason for this is directly related to the different rms velocities. The plots in fig. 4.16 are obtained by calculating the energy loss for each individual scattering angle, as if one would detect deflected electrons within an infinitesimal angle $d\theta$. Hence, for a real detector with finite size, a measurement would comprise a weighted sum of spectra from a range of scattering angles. To account for this, I integrate the scattered electrons (including the angle dependence via the Rutherford factor) over a range of scattering angles with 2° (35 mrad) width. This operation results in a plot of the simulated detected intensity as

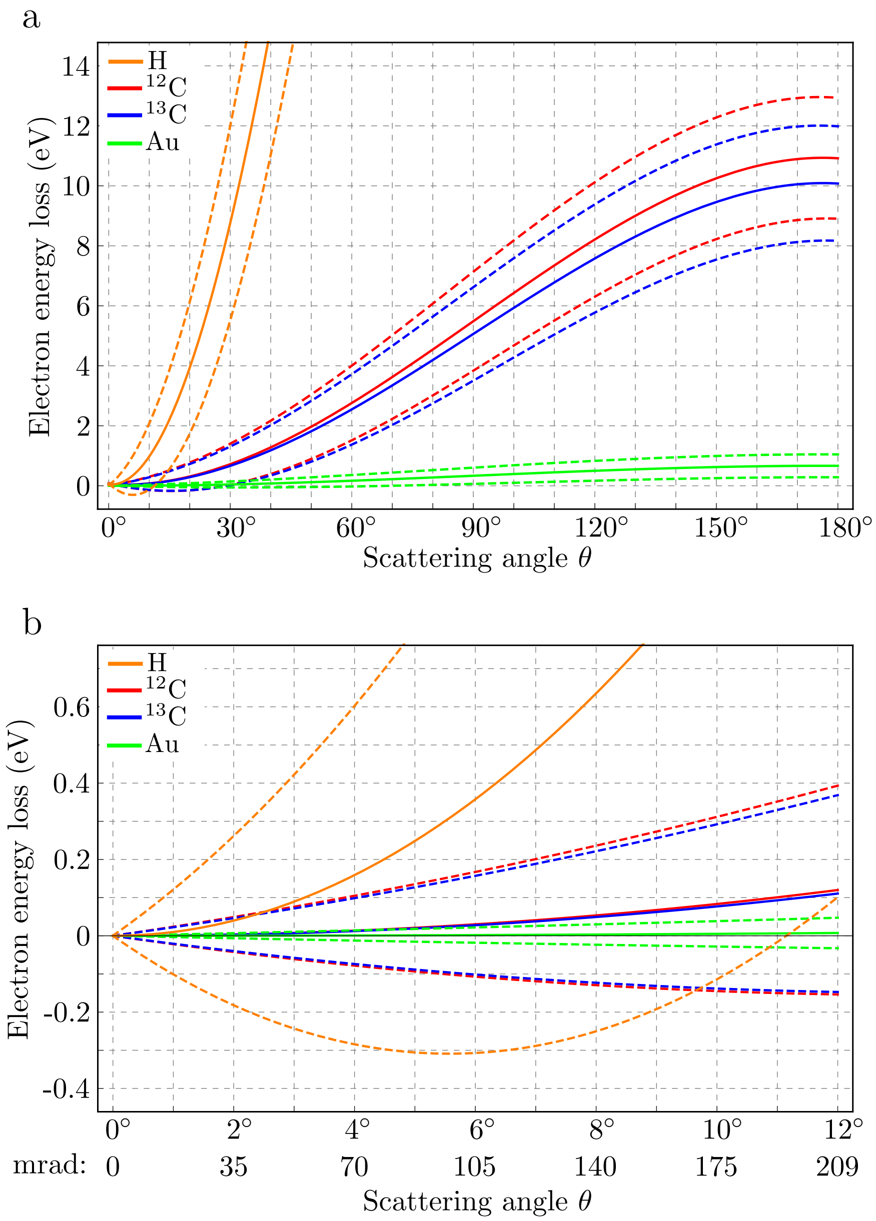

Figure 4.16: Peak position (solid lines) and FWHM (dashed lines) of the energy loss for H, ^{12}C, ^{13}C, and Au as a function of scattering angle. (a) Shows the full range, (b) a close-up for 0°–12° calculated at higher precision.

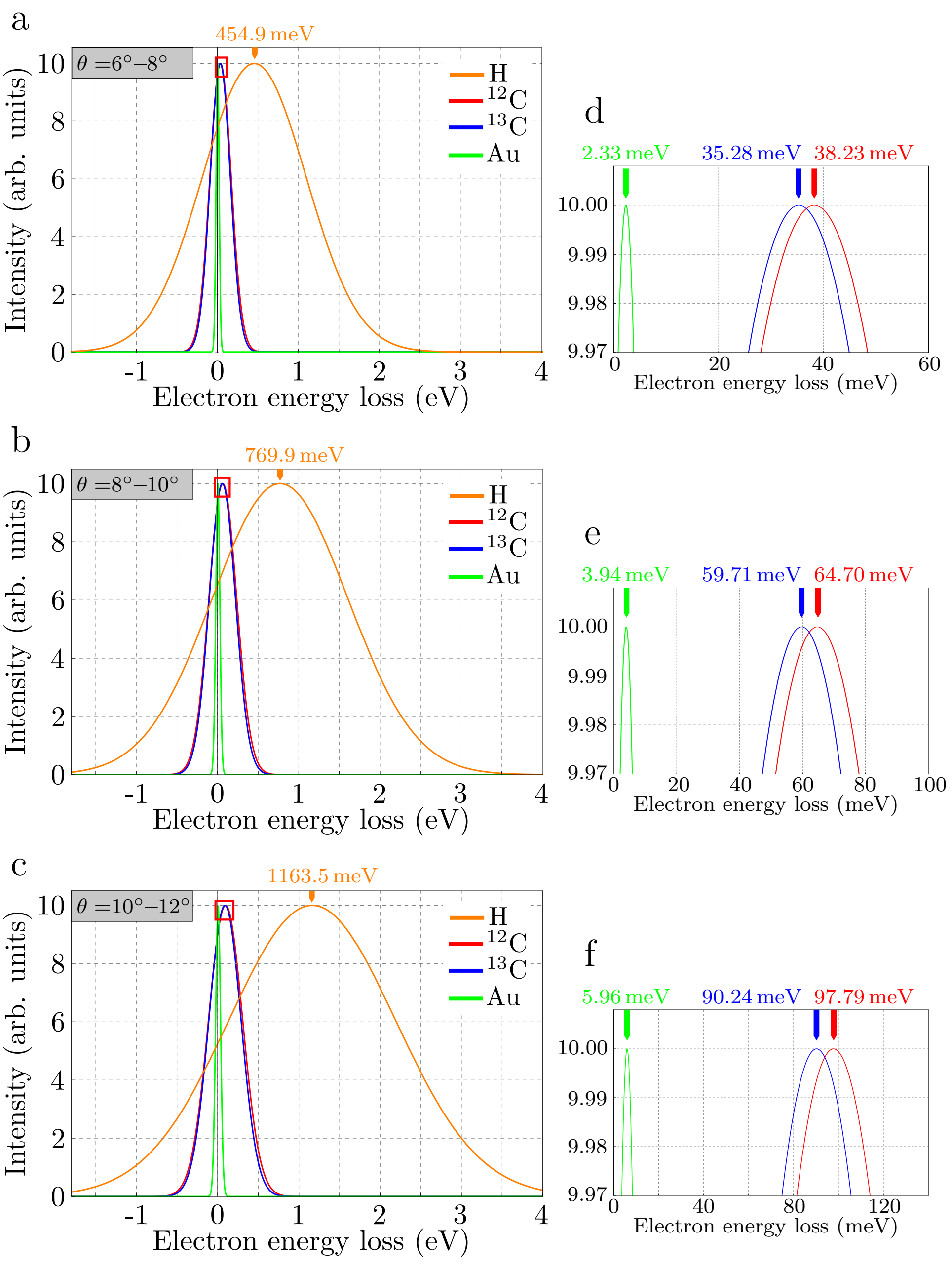

Figure 4.17: Simulated EELS spectra for a detection angle in the 6°–8° (a), 8°–10° (b) and 10°–12° (c) range. The spectra are obtained as a vertical integration of the scattered intensities of fig. 4.16. (e–f) Show a magnified view of the area inside the red box in (a–c).

a function of energy loss. For the sake of brevity, this plots will be sometimes referred to as EELS spectra, although it should be kept in mind that these are not EELS spectra in the traditional sense, since inelastic scattering is not considered here. The calculated spectra are shown in fig. 4.17 for the four considered species at different angles. Fig. 4.17a, b and c show the simulated EELS spectra detected in the 6°–8°, 8°–10° and 10°–12° angular scattering range respectively. The area inside the red box in each of the spectra is shown at higher magnification in fig. 4.17d–f. The results depend only weakly on the choice of the integration width (2° or more), as the result is dominated by the smallest angles in the sum, due to the rapid decay of intensity at higher angles. It is striking that the curves for ^{12}C and ^{13}C, which have a $\sim$8% relative difference in mass, appear to be almost on top of each other, due to the large broadening. The peak separation is on the order of 1% of the FWHM at 10° scattering angle, and even for back-scattered electrons is only 20% of the FWHM. It is also worth mentioning that, due to the thermal motion of the nuclei, the electron may not only loose but also gain energy.

4.2.3 Analysis and discussion

Many potential applications of spatially resolved EACS can be derived from those previously demonstrated for bulk samples and in the absence of spatial resolution, such as the analysis of sample composition [90], momentum distributions of atoms [91, 92], or the detection of light elements [92, 93]. If a beam is scattered from a larger number of atoms, the main question will be whether partially overlapping peaks can be separated. The Doppler broadening of the peaks, resulting from the motion of the nuclei, would make it impossible to separate the peaks from atoms of neighboring masses, if they are recorded simultaneously. However, if the primary beam can be limited to a single atom, the problem of separating partially overlapping peaks will be reduced to that of identifying the center position of a single peak with sufficient precision.

Here, it is crucial to realize that the center position of a peak can be determined with much higher accuracy than the resolution, only limited by the available signal to noise ratio. In the following, I will analyze the possibility to separate the two stable isotopes of carbon, ^{12}C and ^{13}C. In a 2D form of carbon (graphene), a probe size of 1.4 Å would be sufficient to place the beam on a single atom. Fig. 4.16 show the center and FWHM of the energy loss profile at various scattering angles for ^{12}C and ^{13}C, with a difference in peak position in the order of 1% of the FWHM at scattering angles of 5°–10°. For distinguishing the two spectra, detecting the small shift in a wide Gaussian peak will require a sufficient number of counts. Importantly, while the shift becomes wider with increasing scattering angle, the intensity decreases. From basic statistics, it is known that the peak position in a Gaussian distribution can be determined to a precision σ_c that is only determined by the width (either expressed by the standard deviation σ or by the FWHM) and by the number of counts N in the measurement [94]:

$$\sigma_c = \frac{\sigma}{\sqrt{N}} = \frac{FWHM}{2.35\sqrt{N}} \tag{4.7}$$

For our purpose, σ_c must be equal to or smaller than the separation E_{sep} of the two peaks. This means that the limiting precision for the peak identification is $\sigma_c = E_{sep}$, and inverting equation 4.7 gives a minimum required number of counts N:

$$N = \left(\frac{1}{2.35\dfrac{E_{sep}}{FWHM}} \right)^2 \tag{4.8}$$

Fig. 4.18 shows the result of this analysis. In fig. 4.18a the ratio between the peak separation and FWHM is shown, both for the ideal case (infinite energy resolution) and for a realistic setup with a limited energy resolution of 300 meV. For the latter case, the intrinsic width and the width due to finite resolution are added in quadrature as:

$$\mathrm{FWHM}_{total} = \sqrt{(\mathrm{FWHM}_{resolution})^2 + (\mathrm{FWHM}_{intrinsic})^2}$$

Again, a 2° (35 mrad) integration was used, and the horizontal axis in fig. 4.18 refers to the inner angle. Fig. 4.18b shows the required number of counts according to equation 4.8 that is needed to detect the difference in the peak position. Finally, using the Rutherford cross section, this can be converted into a required dose of the primary beam, as a function of scattering angle (fig. 4.18c). For the target of a single-atom identification, this dose has to be considered as dose per atom. Remarkably, the curve for finite energy resolution has a pronounced, relatively broad optimum (minimum) at an inner collection angle of 6.3° or 110 mrad. An additional point that is worth noting, is that the required primary dose does not grow dramatically even for larger angles. This is because the required number of counts at the detector drops at large angles, due to larger separation. One might even consider a spectrometer for back-scattered electrons (e.g. >160°), where a few (4–5) detected electrons per 10^9 primary electrons would be sufficient for a mass fingerprint of the sample. Finally, it is worth to comment on the primary beam energy dependence of these effects. Higher voltages would lead to a larger energy losses, which potentially are easier to detect. However, it is likely that sample stability under the beam will be a key limitation [95–97]. Graphene was found to be regularly stable up to 10^8 $e^-/\text{Å}$ (which already involves hours of continuous irradiation) and probably well beyond, in 60 kV STEM experiments under UHV conditions (2×10^{-9} mbar), while at 100 kV this experiment would be impossible due to the destruction of the sample.

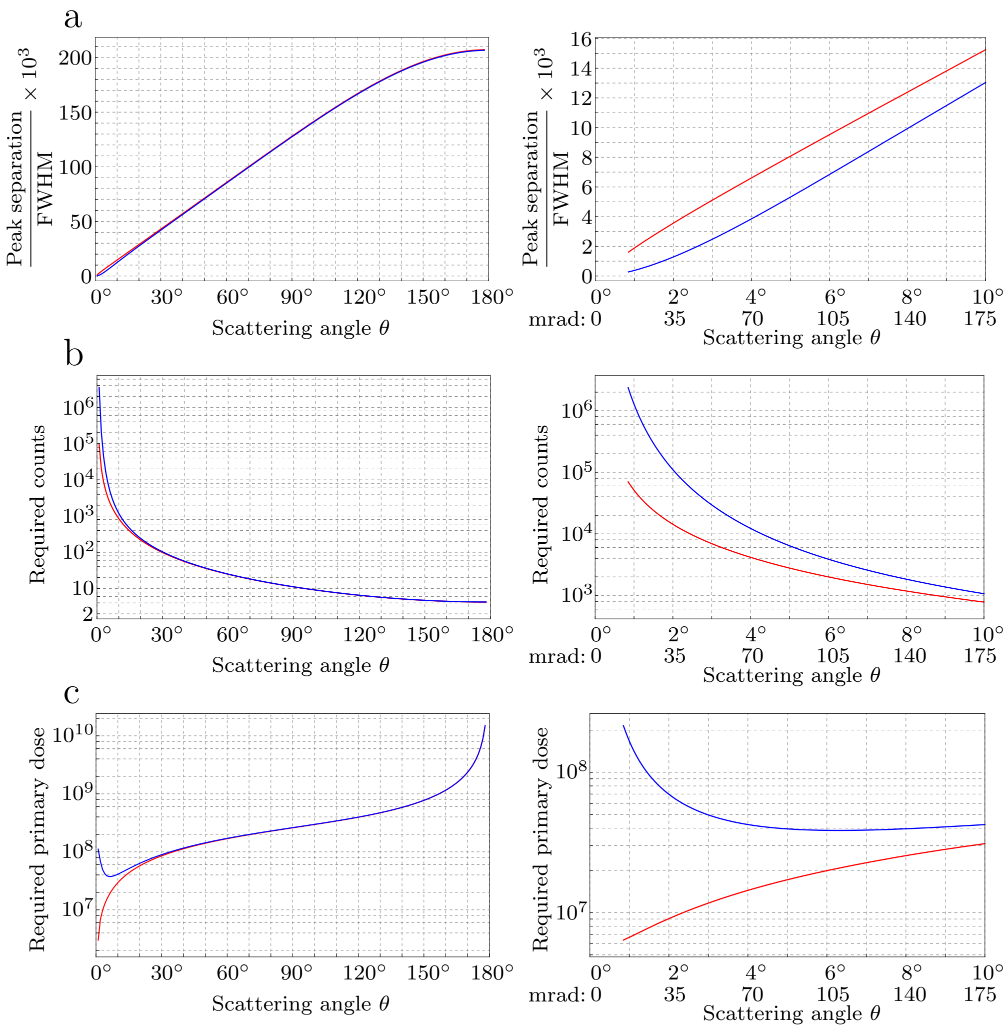

Figure 4.18: Plots of: (a) ratio of peaks separation to FWHM. (b) Minimum required counts at the detector needed for separating the peaks of ^{12}C and ^{13}C. (c) Minimum required primary dose for Rutherford scattering of the required counts in (b) to the given angle. The red curves are for an ideal spectroscopic setup, while the blue curves are for a finite energy resolution of 300 meV. All curves are plotted as a function of scattering angle. Left side: 0°–180° range, right side: detailed plot for the 0°–10° range.

4.2.4 Initial experiments

As a proof of principle, I show here an initial experiment on an amorphous carbon film with gold particles, where the energy loss of electrons scattered to large angles was measured. For this experiment, the NION UltraSTEM 100 was used, operated at 60 kV. The Gatan parallel EELS spectrometer was equipped with an Andor Zyla 5.5 sCMOS camera for fast acquisition of 2D spectra (momentum-energy maps) at each point of the scan, as introduced in section 3.3. The scan size was 64 × 64 nm with 128 × 128 pixels, and each spectrum consisted of a 1k×1k exposure. For this experiment, instead of using the custom aperture described in section 3.3 to block the BF disk (which was not available at the time yet), electrons scattered to larger angles were measured by tilting the beam before the entrance of the spectrometer, using a deflector in the last projection lens. The BF (forward-scattered) beam was tilted outside of the EELS entrance aperture, and only the high-momentum-transfer "tail" of the zero-loss peak (ZLP) that contains electrons scattered to a certain range of angles is detected. Using the bright field disc with a diameter of 50 mrad (of the non-tilted beam) as reference, the spectrometer was estimated to capture angles up to 60 mrad, i.e., the angular field of view is ca. 120 mrad. By tilting a beam with 50 mrad convergence angle outside this aperture, it can be concluded that the tilt was at least 85 mrad; in this way scattering angles between 25 and 145 mrad, or more, can be observed simultaneously in one exposure. The precise angles are difficult to estimate, as they are affected by aberrations [98]. In this mode, the HAADF detector becomes a BF detector, and its signal is recorded simultaneously with the momentum-resolved EELS map.

Fig. 4.19a shows an individual exposure on the spectrometer camera. The BF disc was tilted away far to the left and the main curvature of the line is due to aberrations, strongly magnified in the y-direction by a large dispersion. However, only the variations of this curvature during the scan are of relevance here. At a small scattering angle (yellow box), a reference measurement is made, in order to compensate variations e.g. in the high voltage. At a larger scattering angle, the peak position is measured (cyan box). Fig. 4.19b shows profiles from gold and carbon, along with the Gaussian fits that were used to extract the peak positions. Fig. 4.19c shows the simultaneously acquired BF STEM image, where the carbon film, gold particles and a portion of vacuum are visible. Fig. 4.19d shows a map, where the energy difference between the peak position of the reference and the measured profile are displayed. Note that the reference signal peak position by itself has no visible correlation with the sample structure.

The difference in energy loss between gold and carbon measured in this way is ∼150 meV, estimated from the separation of the Gaussian fits in fig. 4.19b. This is somewhat larger than the 50–100 meV that would be expected from the calculations. The difference may be due to uncertainty in the angles, or

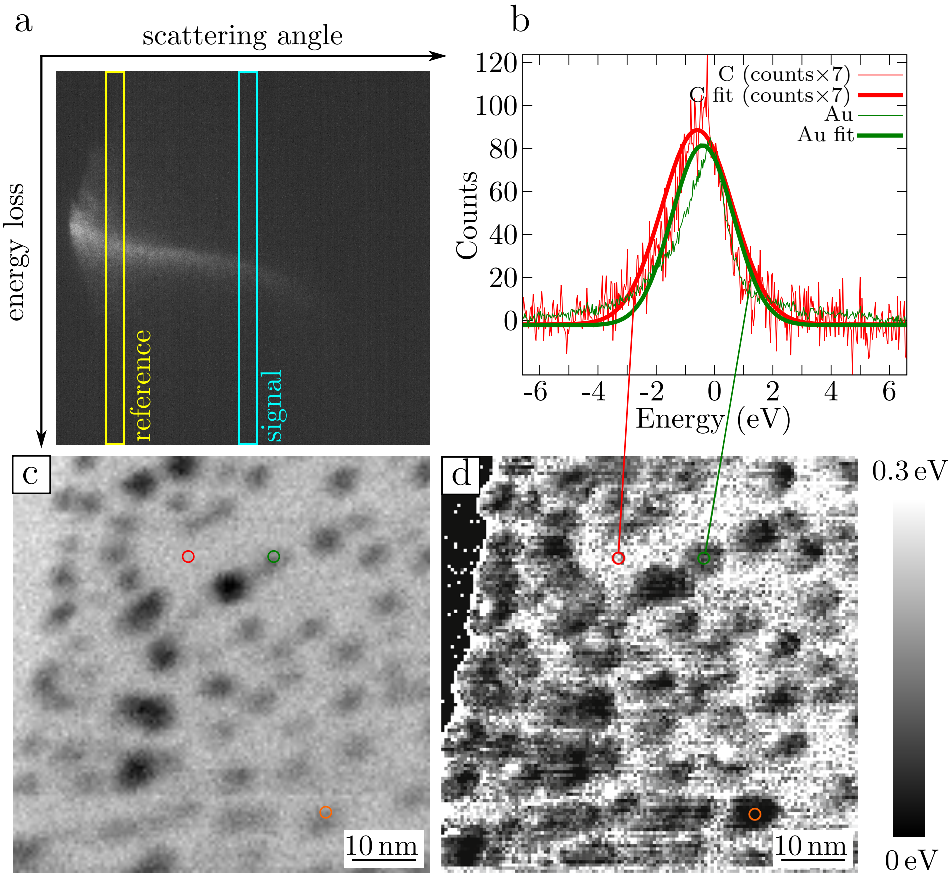

Figure 4.19: First attempt of acquisition of energy-momentum maps for high scattering angles, using gold particles on amorphous carbon. (a) Individual exposure on the spectrometer, where the yellow profile (small scattering angle) is used as reference, while a profile from the cyan box is used as signal. (b) Signal on carbon (multiplied by a factor of 7) and on gold for comparison. For the two points chosen the reference peak position happened to be at the same value. (c) Simultaneously acquired BF image. (d) Map of the difference between the reference peak position and the signal peak position. A small area of vacuum is present in the upper left part of the image.

fits to the curve being affected by the differences in scattered intensity on gold and carbon. For example, in fig. 4.19b it is visible that the Gaussian fit does not match perfectly to the curves. However, it is important to point out that a clear difference in the position of the maximum is already discernible by eye in the raw curves. When the beam is on a gold particle, it also passes through carbon. But the signal on any gold particle is much stronger than on carbon, hence it should be dominated by scattering on gold. It is also interesting to note that the correlation between the peak shift and the BF image is not perfect. Consider, for example, the particle marked by an orange ring in fig. 4.19c,d: it is particularly strong in the energy loss signal but barely visible in the BF image.

The shift in peak position can be detected even though it is below the energy resolution and stability of our instrument. This is achieved by recording simultaneously multiple angles and using the small-angle signal as a reference. A similar measurement was shown by Lovejoy et al. [93], using a monochromated instrument, and recording only the high-angle scattering signal.

4.2.5 Conclusions

Spatially resolved electron-atom Compton scattering could provide a new and interesting type of signal in STEM, even with the scattering angles that are currently accessible. It can provide a way to identify the mass of a sample up to individual atoms and to obtain a direct insight into their vibration amplitudes. I showed that it is possible to distinguish gold from carbon on the basis of this signal experimentally, and I discussed the prerequisites for identifying the isotopes of carbon, which appear identical in all other contrast mechanisms so far available in an electron microscope. One of the identified prerequisites will be that the primary beam is limited to a single atom, so that only the center position of the energy loss peak needs to be measured, rather than a separation of two strongly overlapping peaks. Further, the sample has to withstand a high dose. Most importantly, a precision (but not resolution) in measuring energy loss to a few millielectronvolts will be needed, simultaneously with an efficient collection of electrons scattered to large angles.

4.3 Weighing atoms by high-angle electron scattering. Part 2: experiment

Based on the solid theoretical study presented above, isotope mapping experiments were designed and performed in our STEM. In this section, which contains unpublished material, I present and discuss these experiments. As I will show, despite significant effort, unambiguous identification of ^{12}C and ^{13}C on the atomic scale was never achieved. Nevertheless, I learned that the success of the experiment is not forbidden by fundamental limitations and that it is reasonable to imagine that atomic-scale isotope mapping might be accomplished in the future through further improvement of the instrumentation.

4.3.1 Isotope labeled CVD synthesis

Before presenting the STEM experiments, in this section I show how graphene samples consisting of a mixture of ^{12}C and ^{13}C carbon atoms can be prepared and characterized. Isotope labeling is a widely employed and very versatile technique used to track atoms during chemical reactions or to monitor fluxes in metabolic pathways. The "labeling" is done by substituting part of the atoms participating in the reactions with a different isotope of the same species. The power of this technique relies on the fact that, from a chemical perspective, the isotope labeled atoms behave identically to the non labeled atoms and therefore do not affect the outcome of the reaction. Isotope labeling has proven to be a very useful tool to study the growth mechanisms of CVD graphene [99]. To be able to track the distribution of carbon isotopes in graphene samples, an isotope-sensitive measurement technique is required. Undoubtedly, Raman spectroscopy is the primary choice for this task. The positions of the characteristic Raman peaks depend on the masses of the atoms that participate in the lattice vibrations. Based on a simple harmonic oscillator model, one can calculate the shifted Raman frequency ω of an isotopically modified graphene sample as:

$$\frac{\omega_0 - \omega}{\omega_0} = 1 - \sqrt{\frac{12 + c_0}{12 + c}} \tag{4.9}$$

where ω_0 is a particular frequency of a ^{12}C graphene sample, $c_0 = 0.0107$ is the natural abundance of ^{13}C in a ^{12}C sample and c is the concentration of ^{13}C in the enriched sample. Eq. 4.9 provides a straightforward method to measure the concentration of ^{13}C in a graphene sample by simply measuring the position of any of the characteristic Raman peaks. Although Raman spectroscopy is normally an ex-situ technique, when combined with a clever use of isotope labeling, it can reconstruct in great detail the growth dynamics of a CVD sample (see for instance [100]).

In the following, I present two examples where isotope labeling and Raman spectroscopy were employed to study the isotopic composition of two different

CVD graphene samples. For the synthesis of both samples, the inlet of the CVD furnace was connected to two methane bottles, one containing carbon atoms in the natural isotopic composition and one containing 99% of ^{13}C. For the first sample, consisting of separated domains of ^{12}C and ^{13}C graphene, the annealed copper foil was first exposed for 45 seconds to the ^{13}C enriched methane and then to the natural methane for other 45 seconds. Between the two growth steps, both inlets remained closed for 10 seconds to allow residual ^{13}C atoms to be evacuated and thus avoid mixing of the two isotopes

Fig. 4.20a shows a composite Raman map of the as-grown sample on copper. The red and the blue channels of the map were obtained by integrating pixel-wise the signal under the spectra in a $100\,\mathrm{cm}^{-1}$ wide range centered at the position of the ^{12}C and of the ^{13}C $2D$ peak, respectively. The map shows that the sample consists of partially merging graphene islands, with characteristic ^{13}C cores surrounded by ^{12}C ring-shaped regions. Spectra from three selected points in the map are shown in fig. 4.20c (spectra 1–3). Spectra 1 and 2, taken respectively at regions corresponding to ^{12}C and ^{13}C graphene, show the characteristic Raman signature of the graphene lattice, with single G and $2D$ peaks. As expected, the position of the two peaks is different for the two spectra. The accurate position of the peaks is estimated through a Lorentzian fit, leading to $\omega_{G,12} = 1585\,\mathrm{cm}^{-1}$, $\omega_{G,13} = 1525\,\mathrm{cm}^{-1}$, $\omega_{2D,12} = 2726\,\mathrm{cm}^{-1}$ and $\omega_{2D,13} = 2621\,\mathrm{cm}^{-1}$. The measured frequency shift is $60\,\mathrm{cm}^{-1}$ for the G line and $105\,\mathrm{cm}^{-1}$ for the $2D$ line, in good agreement with equation 4.9. Spectrum 3 is taken at a transition region, i.e. at the boundary between a ^{12}C and a ^{13}C domain. Here, the spectrum carries a clear signature of both isotopes, with two G and two $2D$ peaks. This means that, within the area illuminated by the laser ($\sim 0.16\,\mu\mathrm{m}^2$), part of the sample responds as a pure ^{12}C lattice and part as pure ^{13}C lattice, indicating that the boundary between the domains is relatively sharp, with little isotope intermixing.

For the second sample, the annealed copper was exposed simultaneously for 120 seconds to a homogeneous mixture of ^{12}C and ^{13}C methane. Since the two isotopes are chemically identical, ^{12}C and ^{13}C atoms are expected to arrange randomly within the graphene lattice. The Raman map of a continuous monolayer region is shown in fig. 4.20b. Here, the gray scale maps the spatial distribution of the ^{12}C concentration based on the G peak position. Despite significant local variation of the isotopes ratio, none of the mapped area presents ^{12}C only or ^{13}C only behavior, showing an overall good intermixing of isotopes. One spectrum is shown as example in fig. 4.20c (spectrum 4). The positions of both characteristic peaks do not coincide with neither the pure ^{12}C nor the pure ^{13}C frequencies, but they rather fall in an intermediate range ($\omega_{G,mix} = 1548\,\mathrm{cm}^{-1}$ and $\omega_{2D,mix} = 2645\,\mathrm{cm}^{-1}$). Inverting equation 4.9, the calculated local ^{12}C concentration corresponding to spectrum 4 is:

$$c_{12} = 1 - \left[(12 + c_0) \left(\frac{\omega_{G,12}}{\omega_{G,mix}} \right)^2 - 12 \right] \simeq 0.44$$

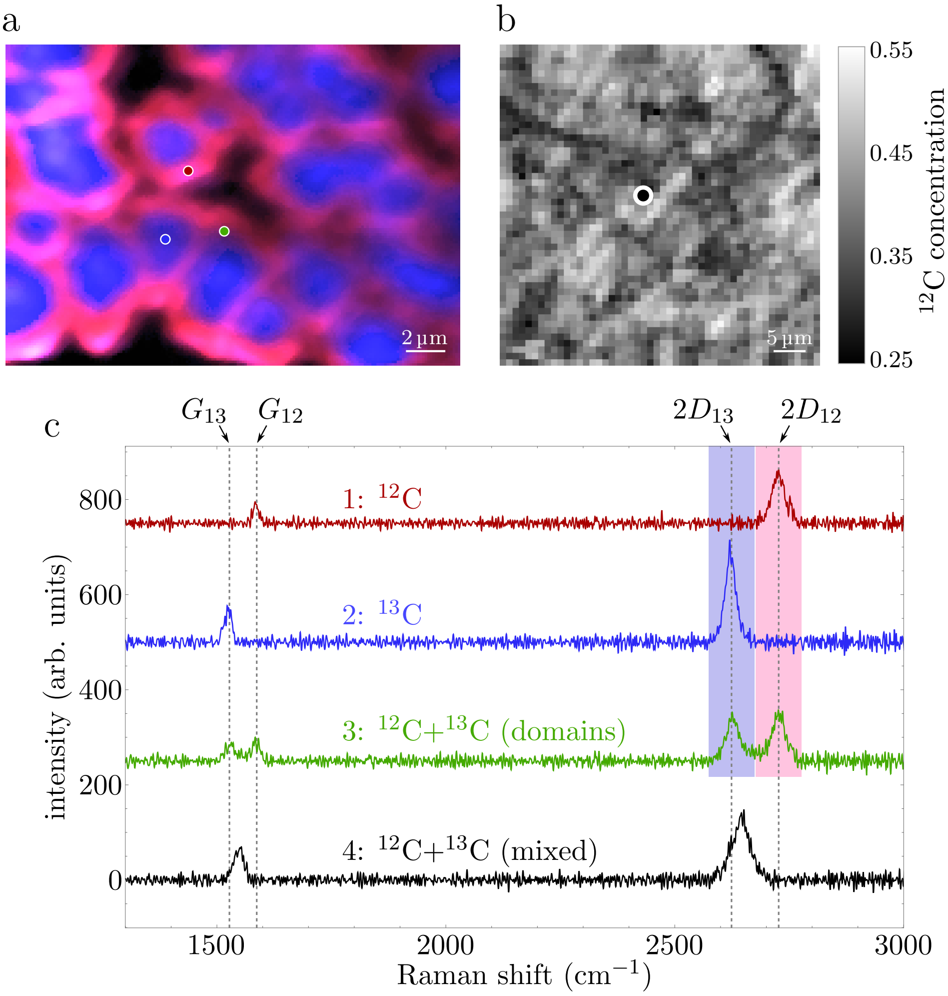

Figure 4.20: (a) Composite Raman map of a graphene sample consisting of separated domains of ^{12}C and ^{13}C graphene. The red and the blue channels are obtained by integrating the signal under the spectra in a 100 cm^{-1} wide range centered at the position of the ^{12}C and of the ^{13}C $2D$ peak, respectively. The black regions correspond to areas not covered by graphene. (b) Local ^{12}C concentration map of an isotopically well mixed continuous monolayer of graphene, based on the position of the G line. (c) Raman spectra from three selected locations marked in (a) and one location marked in (b) (the color of each spectrum matches the color of the mark in the maps). The shaded areas show the two integration ranges used to obtain the map in (a). The gray dashed lines are drawn as a guide to the eye to mark the positions of the G and $2D$ peaks for the pure ^{12}C and ^{13}C graphene.

Spectra 3 and 4 are similar in the sense that they both reveal the presence of ^{12}C and ^{13}C atoms in the lattice but they clearly reflect two different local arrangements of isotopes. This shows that although the spatial resolution of Raman spectroscopy is limited by the diffraction limit of light, it is sometimes possible to get a deeper insight into the structure of the sample on a much shorter length scale. Nevertheless, because of the nature of phonons which are collective vibrations of the lattice, Raman spectroscopy will inevitably fail to distinguish isotopes on the atomic scale.

4.3.2 STEM experiments

The theory and the calculations presented in section 4.2 serve as valuable guidance to plan the actual atomic-scale isotope mapping experiment. As discussed, the goal of this experiment is to discern between atoms of ^{12}C and ^{13}C in a graphene lattice by detecting the tiny shifts in energy losses for electrons being elastically scattered by either of the two isotopes. Depending on the actual solid angle subtended by the detector, the energy losses of electrons scattered by either ^{12}C or ^{13}C differ by only a few meV (see fig. 4.17). However, the EELS detector cannot be calibrated to such a high precision, since the nominal energy resolution of our microscope is 300 meV. This means that the identification of either one of the two isotopes based on absolute EELS measurements is not a viable approach. Rather, a simultaneous measurement of a group of atoms containing both isotopes, followed by a relative comparison of the energy losses is a more effective approach. For this reason, the sample of choice for this experiment consisted of a homogeneous, atomically mixed ^{12}C–^{13}C graphene crystal, similar to the second of the two samples studied in section 4.3.1. This kind of sample ensures that EELS signal originating from both isotopes can be measured in one single STEM scan, thus avoiding inaccuracies in the energy measurement due for instance to fluctuations of the high voltage or to drift in the energy calibration of the EELS unit.

As discussed in section 4.2, it is crucial to limit the primary beam to a single atom and to work below the knock-on damage energy threshold. With our STEM these two conditions can be achieved easily. However, other parameters have to be carefully selected to produce useful measurements. In a typical STEM experiment the user can set three basic parameters to define the scanning mode of the electron beam: the field of view (FOV), the resolution (i.e. the number of pixels per frame) and the scanning speed, defined by the dwell time (i.e. the time spent by the beam on each pixel). Table 4.1 summarizes some of the key points that have to be simultaneously met for the measurements alongside corresponding ideal STEM settings. Even at a first glance, it clearly appears that the STEM settings are contradictory and therefore a compromise has to be found. Fortunately, a trick allows to partially circumvent the problem and to collect an indefinitely large signal without suffering from sample drift. The same area can be scanned multiple times at

Target	**Requires**	**STEM settings**
atomic resolution	large resolution/FOV ratio	high resolution small FOV
sufficient statistics	signal from large number of atoms	large FOV
avoid sample drift	short frame time	low resolution fast scanning speed
maximize signal collection	large e^- dose/atom	small FOV slow scanning speed

Table 4.1: The table summarizes some of the issues to consider while selecting suitable scanning parameters in the experiment. The first column indicates the specific targets to achieve, the second column lists the corresponding requirements to meet the targets and the third column translates such requirements into actual scanning settings.

fast scanning speed, thus minimizing sample drift during the acquisition of an individual frame and then, after careful post-acquisition alignment of the lattice through the whole series, the EELS signal is added pixel-wise. Using this technique, reasonable parameters for data acquisition were found to be $\sim$1 nm^2 FOV, 32×32 pixels frame size and $\sim$5 ms dwell time.

Fig. 4.21a shows an exposure of the EELS camera, recorded at 60 kV acceleration voltage. The characteristic pattern of the custom aperture described in section 3.3, although highly distorted, is well visible and the BF disk is hidden behind the central beam stopper. The image of the aperture looks distorted because of the large energy dispersion. In this mode, the horizontal axis corresponds to the energy-dispersive direction, while along the vertical axis a one-dimensional information on the scattering angle is preserved. To calibrate the energy dispersion, a 5 V offset is added to the microscope's high voltage, resulting in a lateral shift of the EELS signal. The two exposures, with and without offset, are shown in fig. 4.21b in pink and in blue, respectively. The plot in 4.21c is the intensity profile along the yellow line of panel b, showing that the voltage offset produces a $\sim$60 pixel shift on the camera. The resulting energy calibration is thus $\sim$83 meV/pixel, close to the largest possible allowed by our setup. This means that the expected shift of the signal when the primary beam moves from one isotope to the other is as small as 1/10 of a pixel or less. Given the small magnitude of this shift, the whole experiment might at first appear hopeless. Nevertheless, the problem can be tackled by recalling that the peak position of a Gaussian distribution can be determined with a precision that only depends on the number of counts (equation 4.7) and can be thus significantly better than the pixel size. In our case, even if the recorded signal is not Gaussian-shaped, the same argument can be used to address the problem. In fact, the large intensity variations and sharp features created by

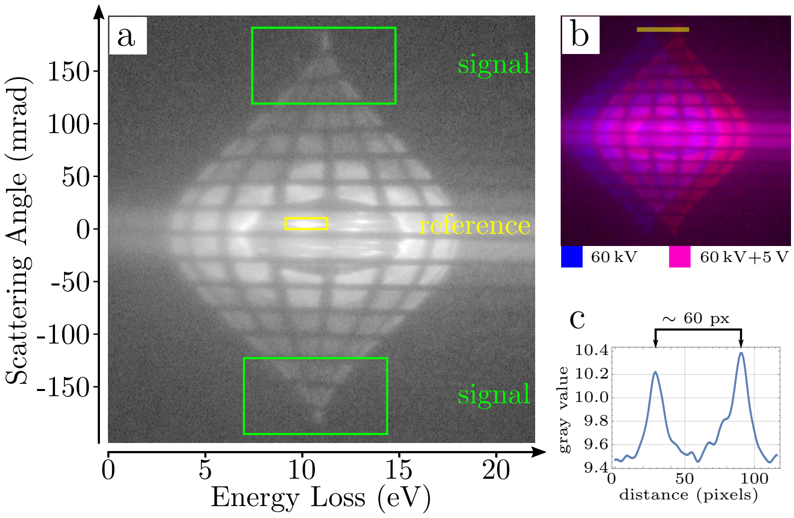

Figure 4.21: (a) Individual exposure of the EELS camera (exposure time ~2 seconds). The green and the yellow boxes indicate, respectively, the portions of the signal used as signal and as reference. (b) EELS exposure at 60 000 eV (in blue) and at 60 005 eV (in pink) beam energy. (c) Intensity profile along the yellow line in (b). From the positions of the two peaks, the energy calibration is found to be 83 meV/pixel.

the grid bars of the custom EELS aperture are, in this case, very helpful to detect small lateral shifts of the recorded signal. Without the aperture, it would be much more difficult to accurately measure the displacement of the broad illumination of the DF disk with sub-pixel precision.

The actual displacement detection of the experimental 4D dataset was measured as follows. The series of signal images were scaled ("stretched") along the energy-dispersed direction by a factor of 100 using linear interpolation, changing the effective energy calibration to 0.83 meV/pixel. This way, the expected shift of the signal is in the few pixels range. As a positive, unexpected side effect, the copper disk of the custom aperture seems to have a few tiny holes, possibly caused by inhomogeneities in the metal deposition. A small fraction of the BF disk can transmit through these holes, which appear as bright features in fig. 4.21a. The region in the yellow box, containing one such bright feature, was taken as small angle reference to account for variations in the high voltage. The shift at large scattering angles, carrying the information on the isotopes, was measured in the green boxes shown in the same figure. A model image was then created by summing all the acquired exposures. The shifts of both the reference and the signal were obtained by a cross correlation algorithm that computes the optimal lateral shift of each image to match the model image. Finally, the map of the difference between reference shift and signal shift is computed. Ideally, this map should show a contrast difference between ^{12}C and ^{13}C atoms.

For the experiment, a $0.6\times0.6\,\mathrm{nm}^2$ area of the graphene lattice was scanned multiple times, totaling 180 frames each 32×32 pixels in size. The recorded 4D dataset consists thus of $32 \times 32 \times 180 = 184320$ individual exposures. The frames series was split into two sets, each containing 90 frames, and each of the two sets was analyzed separately. This way, by comparing the results from each set, it should be possible to confirm the isotopic nature of each individual atom from two independent datasets. Fig. 4.22 shows the results of the analysis. In panel a, an ADF image of the considered area, including eight atoms, is shown. The size of the image is considerably smaller than the size of each individual frame because after the lattice alignment through the whole frame series the analysis is done in the overlapping region only. Fig. 4.22b and c show the EELS maps of the considered region from sets 1 and 2, respectively. The maps show very strong pixel to pixel intensity variation but a weak contrast originating from the lattice is visible. The lattice appears slightly brighter than the background, confirming that the electrons loose a tiny fraction of their energy upon interaction with the nuclei. In Fig. 4.22d and e the same EELS maps are averaged over the pixels (or fractions of pixels) contributing to the same atom, while the background (vacuum) is set to zero. The graph of fig. 4.22f is extracted from the two averaged maps and it plots the electron energy loss for each of the eight considered atoms for the two sets. Considering the scattering angles where the measurement is made (~120–180 mrad), and recalling that for Rutherford scattering the signal is dominated by the lower angles in the range, the predicted energy loss for both ^{12}C and ^{13}C is in the ~30–40 meV range.

The measured values are in average somewhat smaller than expected but considering the large uncertainties on the the actual scattering angles and the contribution of aberrations in the EELS spectrometer, the agreement can be considered satisfying. The match between experiment and theory becomes problematic when looking at the distribution of the data points in the graph. Ideally, all points should accumulate around two values, one for each isotope. Additionally, for a given atom, the measurements of the two sets should coincide within a precision that is smaller than the energy separation of the two atoms (~3 meV). Clearly, this scenario is in contradiction with what observed experimentally. The points in fig. 4.22f do not show any tendency to accumulate around any specific energy value. Even more importantly, for a given atom, the energy separation between the two measurements is always larger than 3 meV, with atom 8 being the only exception.

Based on these observations, I concluded that the unambiguous identification of carbon isotopes on the atomic scale could not be achieved at this stage. Noise variation in the EELS camera, insufficient statistics, effects of the probe tails and inaccuracies in the shift detection of the scattered beam are some of the potential reasons which could explain the unsuccessful outcome of

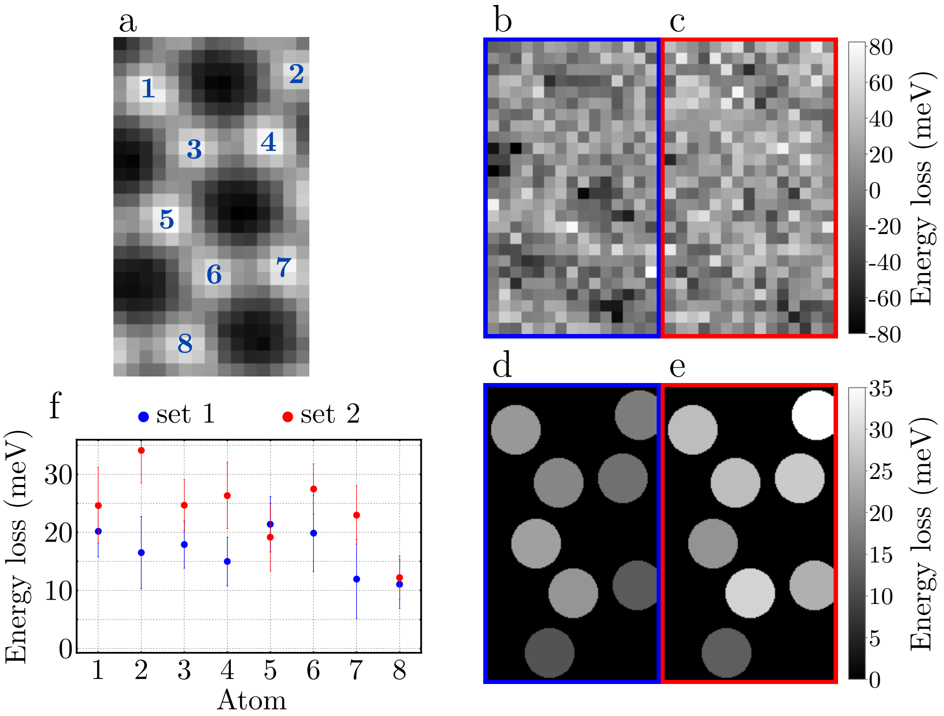

Figure 4.22: (a) ADF image of a small region of the graphene lattice obtained by assigning to each pixel the integrated DF signal acquired at each beam position. The positions of eight carbon atoms are indicated in the overlay. (b,c) EELS maps of the same area of (a) obtained from frames 1–90 and 91–180, respectively. (d,e) EELS maps derived from (b,c) where the values were averaged over the pixels corresponding to the same atom. The background, corresponding to vacuum, was set to 0. (f) Scatter plot obtained from (d,e) showing the energy loss measured at each atomic position for the two sets.

the experiment. Nevertheless, the various attempts demonstrated that the experiment is not limited by fundamental reasons. Graphene showed a superior structural stability at 60 kV: with doses exceeding $10^{12}\, e^-/\mathrm{nm}^2$, not a single vacancy or defect was ever observed in any of the many experiments. Also, the STEM sample stage proved to be very stable, allowing precise tracking of the same few atoms over hours of irradiation. It seems therefore reasonable to imagine that with further development of the hardware the isotope mapping will eventually succeed. In this regard, a monochromated beam would certainly be beneficial. The energy resolution would improve dramatically from the current 300 meV to below 10 meV [101], matching the energy range for isotope separation. The detection system also offers additional room for improvement: cameras with direct electron detection capability would maximize the efficiency of signal collection and would not suffer from light spread within the scintillator, thus achieving a better localization of the detected signal.

4.4 Isotope analysis by knock-on damage in the TEM

The content of this section is based on entry 2 of the List of publications.

In this section I will present an experimental study which aims to differentiate between carbon isotopes in the STEM by quantifying how likely the energetic electrons are to eject atoms from a graphene lattice. This work can be intended as an alternative route towards the identification of carbon isotopes on the atomic scale respect to what presented in sections 4.2 and 4.3. However, it is important to keep in mind that the two proposed methods completely differ in terms of the physical principles that are exploited.

4.4.1 Introduction and basic principles

As discussed in section 4.2.1, in a TEM electrons can transfer a significant amount of energy and momentum to the atomic nuclei in the sample. The maximal amount of kinetic energy is transferred in the case of an interaction with impact parameter $b = 0$ (head-on collision), where the electron is backscattered. If the electron energy is sufficiently large, the target nucleus can be ejected from the lattice, thus creating a vacancy. This effect is commonly known as knock-on damage. Importantly, the transferred kinetic energy E_t is inversely proportional to the mass of the nucleus M, $E_t \propto \frac{1}{M}$, while the binding energy of the target atom to the lattice is identical for the two isotopes. Therefore, for a given electron energy, the likelihood to eject a ^{12}C atom in graphene is larger than for a ^{13}C atom, allowing to map the local isotope concentration by measuring the dose required for the ejection of multiple atoms in a nanometer-sized area. The intrinsic capability of STEM for imaging further allows to map the isotope concentration in selected nanoscale areas of a mixed sample, demonstrating the spatial resolution of this technique.

4.4.2 Experimental methods

For the experiments three different graphene samples were considered: one commercially available (Graphenea), one with 99% pure ^{13}C and one mixed sample consisting of joined grains of ^{12}C and ^{13}C graphene. All three samples were transferred on QF TEM grids. For each of them several time series were recorded at room temperature using the NION UltraSTEM 100 microscope, where each atom, or its loss, was visible in every frame. Small fields of view ($\sim 1 \times 1\,\mathrm{nm}^2$) and short dwell times ($8\,\mu\mathrm{s}$) were chosen to avoid missing the refilling of vacancies.

4.4.3 Experiments on pure ^{12}C and ^{13}C samples

In the first set of the experiments, graphene samples consisting of either ^{12}C or ^{13}C were used. An example data series is presented in fig 4.23(c–g), where five consecutive STEM frames are shown (top row is raw data, middle row is Gaussian filtered, bottom row is double Gaussian filtered). In the fourth frame one individual carbon atom is missing, while in the fifth frame the vacancy has already been refilled. This example shows how fast scanning speed and small field of view are crucial for this experiment. Without these precautions, an ejection event could be easily missed. From each experimental dataset within which a clear displacement was observed, the accumulated electron dose until the frame where the defect appeared (or a fraction of the frame if it appeared in the first one) was calculated. The distribution of doses corresponds to a Poisson process whose expected value was found by log-likelihood minimization, directly yielding the probability of creating a vacancy. Fig. 4.24 displays the corresponding displacement cross sections measured at voltages of 80, 85, 90, 95 and 100 kV for normal (1.107% ^{13}C) and heavy graphene (∼99% ^{13}C), alongside values measured earlier using a high-resolution transmission electron microscope (HRTEM) [102].

4.4.4 Comparing experiment and theory

In addition to the experiment, calculations for the cross section were also performed. For the calculations, the motion of the nuclei was included via a Gaussian distribution of atomic out-of-plane velocities characterized by the DFT-calculated mean square velocity $\overline{V_z^2}$, similar to the approach followed in section 4.2. In contrast to what done previously, where $\overline{V_z^2}$ was estimated using a Debye approximation for the out-of-plane phonon density of states, here the calculation of $\overline{V_z^2}$ is based on the phonon density of states calculated with DFT. The theoretical total cross sections $\sigma_d(T, E_e)$, as plotted in fig. 4.24 by solid lines, are calculated with the McKinley-Feshbach approximation [102, 103], taking into account the lattice vibrations as described in section 4.2.1. A common displacement threshold energy (T_d) was fitted to the dataset by minimizing the variance-weighted mean square error (the 100 kV HRTEM point was omitted from the fitting, since it was underestimated probably due to the undetected refilling of vacancies, also seen in fig. 4.23). The optimal T_d value was found to be 21.14 eV, resulting in a good description of all the measured cross sections. Notably, this is lower than the value calculated by DFT ($Td \in [21.25, 21.375]$ eV), and 2.29 eV lower than the earlier fit to HRTEM data [102].

Despite DFT overestimating the displacement threshold energy, it can be seen from the good fit to the normal and heavy graphene datasets that the theory accurately describes the contribution of vibrations. Further, the HRTEM data and the STEM data are equally well described by the theory despite

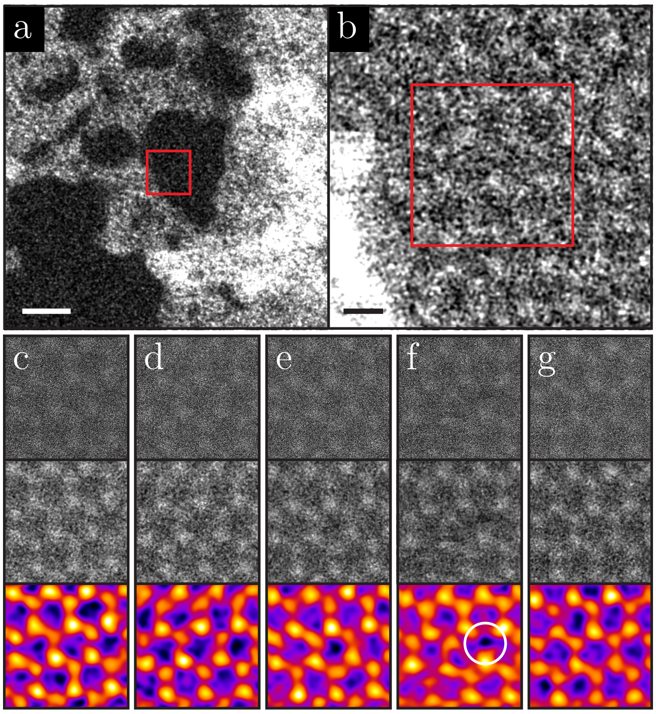

Figure 4.23: Example of the STEM displacement measurements. The micrographs are MAADF images recorded at 95 kV. (a) A spot on the graphene membrane, containing clean monolayer graphene areas (dark) and overlying contamination (bright). The scale bar is 2 nm. (b) A closer view of the area marked by the red rectangle in (a), with the irradiated area of the following panels similarly denoted. The scale bar is 2 Å. (c–g) Five consecutive STEM frames ($\sim 1 \times 1\,\text{nm}^2$, 512×512 pixels (px), 2.2 s per frame) recorded at a clean monolayer area of graphene. A single carbon atom has been ejected in the fourth frame (f, white circle), but the vacancy is filled already in the next frame (g). The top row of (c–g) contains the unprocessed images, the middle row has been treated by a Gaussian blur with a radius of 2 px, and the colored bottom row has been filtered with a double Gaussian procedure [37] ($\sigma_1 = 5$ px, $\sigma_2 = 2$ px, weight = 0.16).

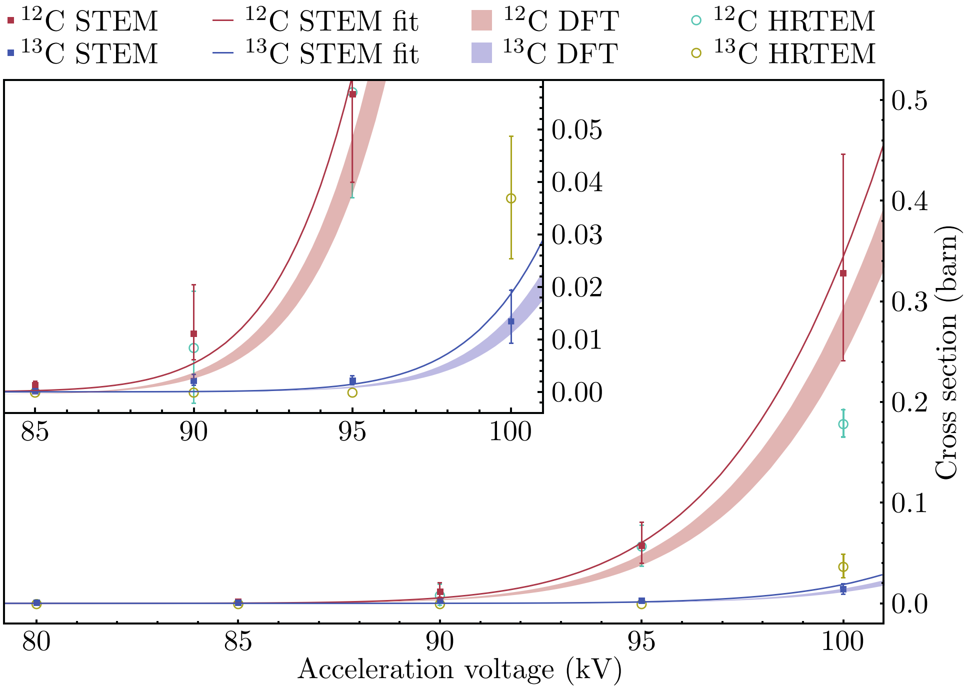

Figure 4.24: Displacement cross sections of ^{12}C and ^{13}C measured at different acceleration voltages. The STEM data is marked with squares, and earlier HRTEM data [102] with circles. The error bars correspond to the 95% confidence intervals of the Poisson means (STEM data) or to previously reported estimates of statistical variation (HRTEM data [102]). The solid curves are derived from the proposed theoretical model with an error-weighted least-squares best-fit displacement threshold energy of 21.14 eV. The shaded areas correspond to the same model using the lowest DFT threshold $Td \in [21.25, 21.375]$ eV. The inset is a closer view of the low cross section region.

having several orders of magnitude different irradiation dose rates. These results thus show that multiple excitations do not contribute to the knock-on damage in graphene. Each impact is, effectively, an individual perturbation of the equilibrium state.

4.4.5 Local mapping of isotope concentration

To test the spatial resolution of the method, the third sample, consisting of joined grains of ^{12}C and ^{13}C graphene, was finally studied. This sample is similar to the first of the two samples discussed in section 4.3.1. Working at 100 kV, 43 regions containing areas of clean graphene were selected, each only a few tens of nanometers in size (an example of such region is shown in fig. 4.23a). The regions are marked in fig. 4.25a as white circles. For each region 4–15 (mean 7.8) fields of view were irradiated, each $1\times1\,\mathrm{nm}^2$ in size, until the first displacement occurred (fig. 4.23f). The mean of the locally measured electron doses that led to an ejection event was then fitted with a linear combination of doses generated by Poisson processes corresponding to ^{12}C and ^{13}C graphene, using the theoretical cross section values. Comparing the mean of the measured doses to the generated data, the isotope concentration responsible for such a dose can be estimated. The result of this analysis is shown in fig. 4.25b, where, for each region, the estimated ^{12}C concentration is indicated by a colored circle. Although each dose results from a stochastic process, the expected doses for ^{12}C and ^{13}C are sufficiently different that measuring several displacements decreases the errors of their means well below the expected separation (see horizontal colored bands in fig. 4.25c). To estimate the expected statistical variation for a certain number of measured doses, a large number of sets of n Poisson doses was generated, and their means and standard errors were calculated as a function of the number of doses in each set. The calculated relative errors scale as $1/n$ and correspond to the precision of the measurement, which is better than 20% for as few as five measured doses in the ideal case. Although the accuracy of this method is difficult to gauge precisely, by comparing the errors of the cross sections measured for isotopically pure samples to the fitted curve (fig. 4.24), an estimate of roughly 5% can be inferred.

4.4.6 Discussion

Prior to the STEM experiment, a large portion of the TEM grid was mapped by Raman spectroscopy. Fig. 4.25b shows a tiny fraction of the Raman map corresponding to the same QF hole area used in the irradiation experiments. Each square of the map represent one Raman measurement location, labeled in the figure as 1–36. As discussed in section 4.3.1, Raman spectroscopy allows for identification of carbon isotopes based on the shift of the characteristic peaks. Fig. 4.25d shows an example of the measured Raman spectrum for location 28, cropped around the $2D$ peak position. Clearly, the spectrum does not correspond to either fully ^{12}C or ^{13}C graphene, indicating isotope mixing within the Raman coherence length. A double Lorentzian fit, indicated by the solid green lines, was performed to accurately determine the positions of both $2D$ peaks. The solid red line shows the sum of the two fitting curves. To assign a single value to the ^{12}C concentration for the overlay of fig. 4.25b, both the shifts of the peaks (to estimate the nominal concentration for each of the two peaks) and their areas (to estimate their relative abundances) were taken into account as follows:

$$\begin{aligned} c_{12}^{total} &= c_{12}^{A}\frac{A}{A+B} + c_{12}^{B}\frac{B}{A+B} = \\ &= \left(1 - \frac{\omega_{12}-\omega_A}{\omega_{12}-\omega_{13}}\right)\frac{A}{A+B} + \frac{\omega_B-\omega_{13}}{\omega_{12}-\omega_{13}}\frac{B}{A+B} \end{aligned} \tag{4.10}$$

where $c_{12}^{A,B}$ are the nominal concentrations of ^{12}C determined from the measured shift of the higher and lower $2D$ Raman peak positions, $\omega_{A,B}$ are the measured peak centers of the higher and lower $2D$ signals, and A and B are their integrated intensities. In other words, c_{12}^{total} is the sum of the concentrations of the ^{12}C nature concealed in the higher and lower peaks, weighted by their relative intensities. The peak positions of fully ^{12}C and ^{13}C graphene ($\omega_{12,13}$) were taken from the highest and lowest $2D$ peak positions in the entire mapped area (covering several dozens of QF holes), giving ω_{12} =2690 cm^{-1} and ω_{13} =2600 cm^{-1}.

A general trend from ^{12}C-rich to ^{13}C-rich regions is captured by both irradiation and Raman methods (Fig. 3b), but a significant local variation in the measured doses is detectable (fig. 4.25c). This variation indicates that the interfaces formed in a sequential CVD growth process may be far from atomically sharp [104], instead spanning a region of hundreds of nanometers, within which the carbon isotopes from the two precursors are mixed together.

4.4.7 Conclusions

I have shown how the Ångstrom-sized electron probe of a STEM can be used to estimate isotope concentrations via the displacement of single atoms. Several displacement events are needed to obtain a statistically meaningful estimate of the local isotope concentration. The sampled areas were in total less than 340 nm^2 in size, containing ∼6600 carbon atoms of which 337 were ejected. Thus, while the nominal mass required for the complete analysis was already extremely small (131 zg = 131×10^{-21} g), the displacement of only five atoms is required to distinguish a concentration difference of less than twenty per cent.

Although these results were achieved with graphene, this technique should work for any low-dimensional material, including hexagonal boron nitride and transition metal dichalcogenides such as MoS_2. This could potentially extend to van der Waals heterostructures of a few layers or other thin crystalline materials, provided a difference in the displacement probability of an atomic species can be uniquely determined. Neither is the technique limited to STEM: the parallel illumination of a TEM with atomic resolution would also work, although scanning has the advantage of not averaging the image contrast over the field of view.

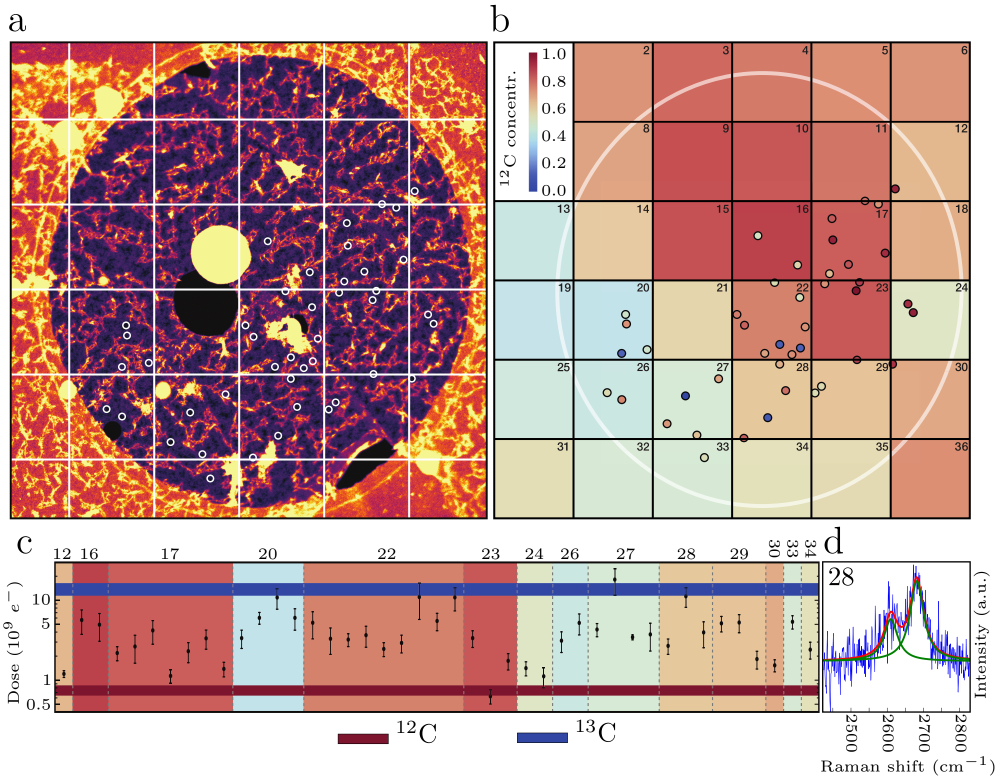

Figure 4.25: Local isotope analysis. (a) A STEM micrograph of a hole in the carbon support film (1.3 µm in diameter), covered by a monolayer of graphene. In each of the overlaid spots, 4–15 fields of view were irradiated. The dimensions of the overlaid grid correspond to the pixel size of a Raman map recorded over this area. (b) Isotope concentration map, where the colors of the grid squares denote the ^{12}C concentration based on the fitting of the Raman $2D$ band response and according to equation 4.10. The overlaid spots correspond to (a), with colors denoting the concentration of ^{12}C estimated from the mean of the measured doses. (c) Locally measured mean doses and their standard errors plotted on a log scale for each grid square. The horizontal colored bands show the means (± standard error) of doses simulated for the theoretical ^{12}C and ^{13}C cross sections. Note that a greater variation in the experimental doses is expected for areas containing a mix of both carbon isotopes. The background color for each section of the plot indicates the estimated ^{12}C concentration based on Raman analysis. (d) Example Raman spectrum acquired at grid square 28, cropped in the vicinity of the $2D$ peak. The measured spectrum is shown in blue, the fitted peaks in green, and their sum in red.

Chapter 5

Summary

This thesis has explored the possibilities of STEM beyond traditional imaging, proving that new types of information can be extracted from materials. Currently, ADF detectors fail in capturing in great detail the scattering dynamics between the electron beam and the sample. In this work, I have designed and implemented a novel detection setup in the STEM capable of recording the intensity of the scattered electron beam as a function of probe position. A self-made EELS aperture was used to block the very intense BF disk and the DF signal was acquired with the EELS camera. This setup allows to use the detector with or without energy dispersion in the EELS unit. In the first case, the developed setup enables EELS measurements at very low energy losses, in a range that is normally not accessible because all the features are hidden by the ZLP. In the second case, without energy dispersion, the setup can be employed as a direction-sensitive detector of the scattered beam, to gain insights into the local 3D arrangement of atoms.

In the first part of the results chapter, I studied a suspended vdW heterostructure consisting of an aligned bilayer of graphene and hBN. I showed that AB stacked regions are consistently larger in size than AA and AB' regions, a behavior that was unexpected according to simulations based on a rigid graphene/hBN model. I employed the developed detector to monitor how the scattered intensity of the electron beam changes as the probe moves across differently stacked regions, and I analyzed the obtained 4D dataset by evaluating the ACOM of each recored image. This technique is extremely sensitive to small local tilts of the heterostructure and to strain in any of the two lattices, thus providing details on the local stacking geometry of the atoms. A relaxed graphene/hBN model was computed using an energy minimization approach based on DFT calculations, predicting that the heterostructure should distort in the out-of-plane direction. Simulated STEM images based on the relaxed model fully agree with the experimental data, proving that the studied bilayer has a buckled structure. The total amplitude of this out-of-plane distortion is nearly 1 nm and its periodicity matches the moiré wavelength.

Further analysis shows that the local strain in each of the two layers tends to maximize the lateral extension of the AB stacked region, which is predicted to be the energetically most favorable stacking type. This work has shown how the strength of the vdW interaction between graphene and hBN is modulated locally, causing the membrane to distort in the out-of-plane direction.

I then moved to another topic, investigating theoretically the possibility of detecting individual atomic masses by elastic scattering of electrons to large angles. This work was motivated by the unprecedented insights that mass-resolved atomic-scale mapping in a STEM could provide. For instance, distinguishing between the two stable isotopes of carbon, ^{12}C and ^{13}C, would open the doors to isotope labeled chemistry combined with the inherent atomic resolution of the STEM. To this end, I studied the angle-dependent Rutherford scattering process and I calculated the energy losses for electrons being scattered by H, Au, ^{12}C and ^{13}C nuclei. For a more realistic description of the process, I also included the atomic motion in the calculations, and I simulated the EELS spectra for each of the considered species as a function of the detected angle. For angles normally accessible in existing STEMs, the EELS peak positions for ^{12}C and ^{13}C are predicted to only differ by a few meV, while their FWHM spread over several hundreds meV. Nevertheless, if the primary beam can be focused on a single atom, only the shift of a single peak, rather than the positions of two convoluted peaks, has to be detected. As a proof of principle, gold and carbon were experimentally separated based on a signal that only depends on the masses, rather than on their atomic numbers.

As a natural next step, I then attempted experimentally to differentiate between ^{12}C and ^{13}C atoms in a graphene sample consisting of an homogeneous mixture of the two isotopes. The same detection setup used for the vdW heterostructure study was also employed here, with the difference that a high energy dispersion was used in this case. Despite intense dedication and careful procedures, the ultimate goal of atomic-scale isotope mapping was not achieved. Nevertheless, I showed that the limitations are only related to the energy resolution of the EELS and possibly to the camera, while the sample was proven to sustain electron doses in excess of $10^{12}\, e^-/\mathrm{nm}^2$ and single-atom tracking was not an issue. Therefore, the experiment is likely to eventually succeed with better instrumentation.

Finally, I studied the isotopic composition of graphene samples by probing the local probability of atomic ejections caused by knock-on damage. Working at acceleration voltages in the 85–100 kV range, small portions of the graphene samples were continuously irradiated until a vacancy was created. The ejection probability averaged over a large number of independent events, allowed to measure the cross sections for both ^{12}C and ^{13}C graphene samples. The results of this analysis were then employed to measure the local concentration of ^{12}C and ^{13}C in a sample that contained both isotopes arranged in separated domains. This experiment showed that the interface between the domains is far from being atomically sharp, a result that could not have been achieved by other isotope-sensitive techniques such as Raman spectroscopy.

Appendix A

2D amorphous carbon films

During the final period of my Ph.D. I worked on the synthesis and characterization of 2D amorphous carbon (a-C) films. Most of the work was done after the completion of the first draft of the thesis and therefore this study will be presented here in the form of appendix. This work has been recently presented as a contributed talk at the "NT17" international conference, held in June 2017 in Belo Horizonte, Brazil.

A.1 Introduction

The study presented here has been inspired by a 40 years old publication by Isaacson and colleagues [105] (see also the review from 2012 [106]). In this work, the authors reported on the characterization of ultra-thin ($\sim 1\,\mathrm{nm}$) carbon films by scanning transmission electron microscopy. These films were produced by vacuum arc discharge evaporation of graphite rods onto cleaved NaCl crystals and were then utilized as support for TEM samples. Given their small scattering power, these films provided an ideal support for heavy samples, allowing high contrast imaging of individual metallic atoms (see for instance the two individual Au atoms in fig. A.1a). Beside serving as an excellent support, the authors soon realized that the carbon film itself was a sample of great interest. The profile along the yellow dashed line of fig. A.1b, shown in fig. A.1c, indicates that the intensity of the ADF STEM image varies in discrete steps, proving that the film has a layered structure. Monolayer areas, as the one marked by the dashed red circle in fig. A.1b, were identified within the film, and based on a quantitative measurement of the scattered signal, the authors calculated that the thinnest regions corresponded to a projected atomic density of $0.3\,\mathrm{atoms/\mathring{A}^2}$. Considering that the atomic density of a single layer of graphite is $0.305\,\mathrm{atoms/\mathring{A}^2}$, they concluded that the regions they observed were "consistent with individual graphite-like layers". A remarkable result, considering that graphene would have only been discovered 25 years later. Unfortunately, back in 1979, Isaacson's electron microscope only had a

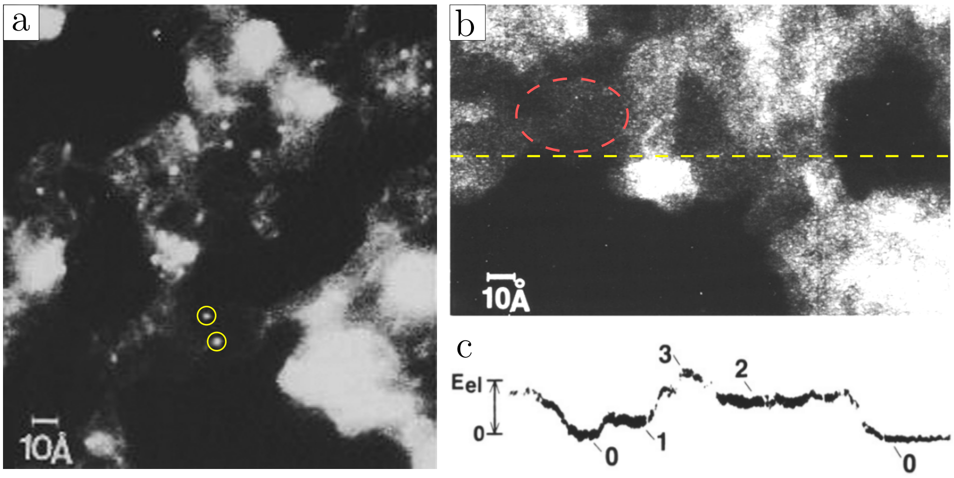

Figure A.1: Figures adapted from ref. [106]. (a) ADF image of the carbon film used as TEM support. Two individual Au atoms are marked by the yellow circles. (b) ADF image of another carbon film. The intensity profile along the dashed yellow line is shown below (c). The dashed red oval indicates a monolayer region.

lateral resolution of 2.4 Å and therefore the atomic structure of the monolayer regions remained unsolved.

Thrilled by this study and with an incomparably better STEM, I reproduced the synthesis of the thin a-C films following Isaacson's recipe to finally unveil their atomic structure.

A.2 Sample preparation

The thin films were produced in a deposition chamber (Mantis HEX system) with a base pressure of $\sim 10^{-6}$ mbar at room temperature. Fig. A.2a shows a schematic of the deposition setup. Carbon was thermally evaporated by passing a short AC high current pulse through a carbon fiber (fig. A.2b), which was previously degased in vacuum to desorb possible contaminants. The substrate of choice was a freshly cleaved NaCl single crystal (fig. A.2c). For STEM inspection, the thin film was transferred to a TEM grid by simply laying the grid onto the carbon coated salt crystal and by dissolving the latter in deionized water.

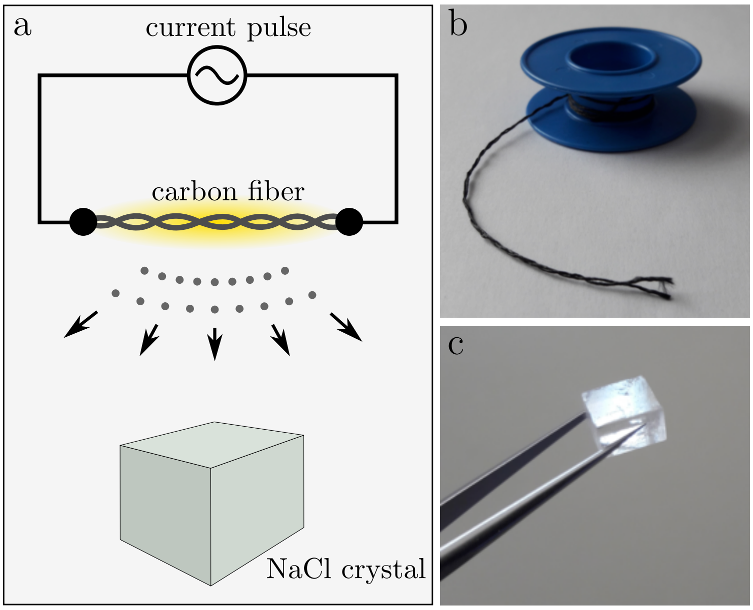

Figure A.2: (a) Schematic of the deposition setup. Panels (b) and (c) show photographs of the carbon fiber and of the cleaved NaCl crystal used in the experiment, respectively.

A.3 STEM imaging

The carbon deposition produces a homogeneous, continuous film with constant thickness, with few isolated cracks after transfer to TEM grids. Fig. A.3a shows one QF hole fully covered by the carbon membrane. At higher magnification the a-C film shows local variations in thickness and occasionally some holes. The intensity profile along the red line in fig. A.3b, plotted in fig. A.3c, shows abrupt changes in thickness, in agreement with what found by Isaacson. In particular, a layered structure with up to three layers is typically observed here. Brighter areas, as the one marked by the yellow circle in fig. A.3b, are identified as contaminants and are extrinsic to the layered structure.

I then focused on the monolayer regions. Atomically resolved images, as the one shown in fig. A.4a, indeed confirm that the thinnest areas consist of a 2D network of sp^2 bonded carbon atoms. Unlike graphene, these areas have such a high density of defects that they can be effectively considered as 2D amorphous structures. Fig. A.4b shows a magnified view of the area in the red box of panel a. Differently sized polygons, indicated by the overlay in fig. A.4c, are identified within the atomic structure. Ring statistics shows that for this area hexagons are the most abundant type of polygon (59.8%), followed by pentagons (26.5%), heptagons (11.7%) and finally octagons (1.9%). I analyzed tens of monolayer areas and found that this distribution does not vary significantly with the position. Indeed, this specific distribution is typical for

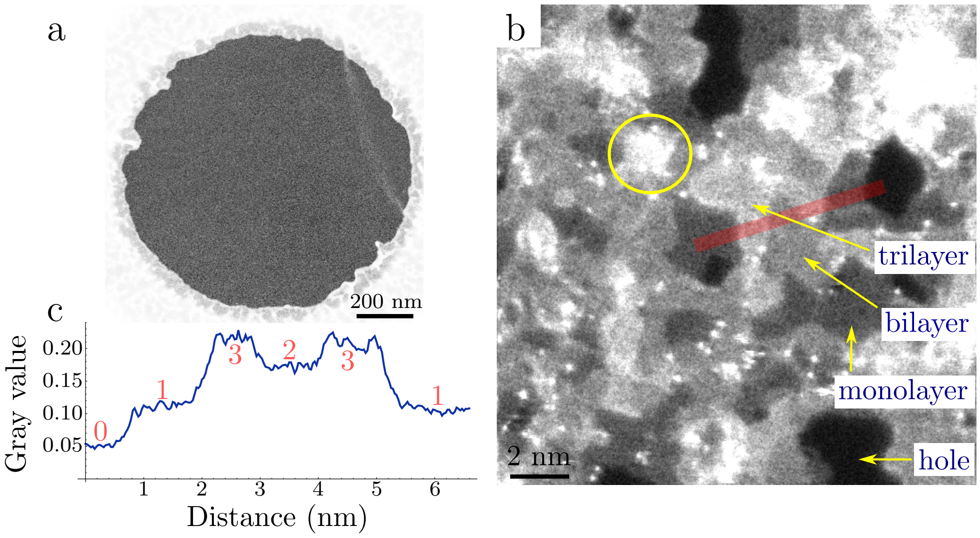

Figure A.3: (a) MAADF image of the a-C film suspended on a QF hole. The film is shown at higher magnification in (b). In (b), examples of mono-, bi- and trilayer regions are indicated as well as one hole. The bright feature marked by the yellow circle is an accumulation of contaminants. The intensity profile along the red line is shown in (c), where the number of layers is specified by the numbers in red.

2D amorphous materials as explained in the following. In general, amorphous structures are characterized by having no long-range ordering. However, in the special case of a 2D structure, where the system is constrained to a planar geometry, polygons are not placed in a random order, but they are arranged to obey a short-range ordering pattern. It was found that it is possible to predict the average size of the neighboring rings based on the central polygon [107, 108]. This empirical relation is expressed by the Aboav-Weaire law and it does not only apply to atomic structures but to a much more vast set of 2D amorphous networks, ranging from macroscopic rock formations like the Giant's Causeway in Northern Ireland to cell networks studied by optical microscopy [109, 110].

For the case of 2D carbon structures, the transition from a perfect crystal to a fully amorphous network is far from being abrupt, as recently shown by electron irradiation experiments on graphene [111]. Since intermediate states exist, to evaluate quantitatively the degree of crystallinity of the a-C films, the parameter C (crystallinity) is introduced and defined as:

$$C = \frac{N_6}{\sum_{i=4}^{9} Ni}$$

where N_6 is the number of hexagons and the denominator is the total number of rings. In other words, C is the fraction of hexagons in the network. For the

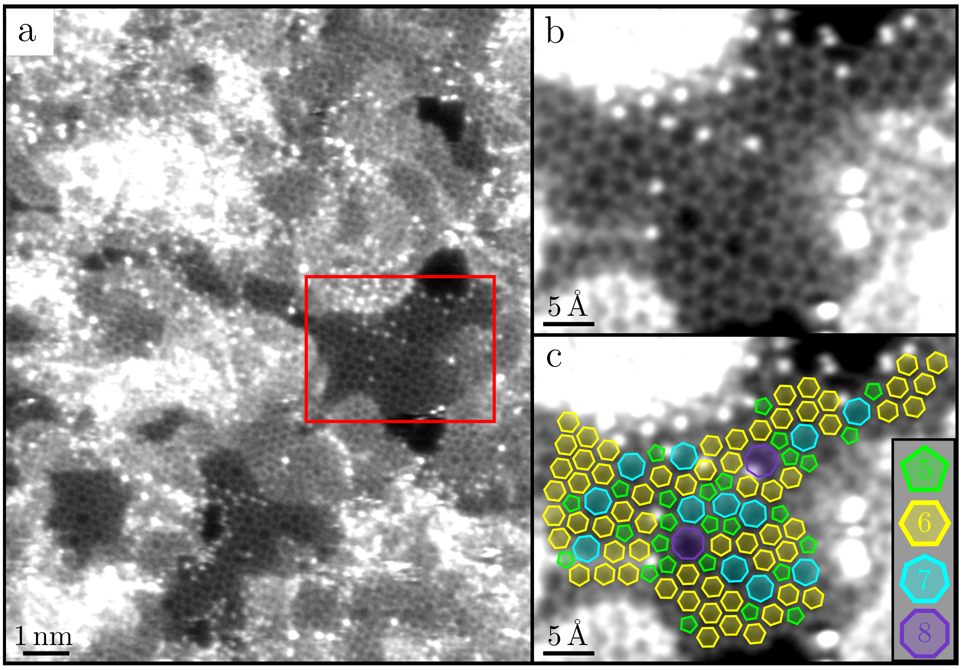

Figure A.4: (a) Atomically resolved MAADF image, showing an area of the a-C films with several monolayer regions. The area inside the red box is shown at higher magnification in (b). (c) Same as in (b), superimposed with a model that shows the various polygons identified within the structure.

observed a-C monolayer regions, I found $C = 0.6 \pm 0.1$. To put this value in context, it is instructive to compare it to what found for other 2D amorphous systems. 2D silica has $C = 0.4$, both when grown on a metallic substrate [112] and when supported by graphene [113]. The crystallinity of graphene irradiated by electrons at 100 kV, depending on the dose, can be continuously tuned between 1 and 0.5 [111], whereas for ion bombarded graphene (Ga^+ ions at 35 kV) a value of $C = 0.63$ was found [114]. This places the a-C films in a range that is typical for irradiated graphene. However, note that irradiation experiments are time-consuming and that amorphous carbon structures can only be obtained locally whereas a-C films are intrinsically amorphous over the whole sample area. Finally, it is worth noting that the definition of crystallinity given here implies that for a totally amorphous structure the value C does not go to zero. Indeed, a structure with $C = 0$ would be completely depleted of hexagons and therefore not random. Following the famous Zachariasen model of a 2D glass [115], Schackelford and Brown have designed an algorithm to build a random 2D network starting from three-fold coordinated building blocks [116]. As the algorithm progressively assembles the elements in a fully random manner, the resulting structure can be safely considered as a completely amorphous 2D network. Ring statistics shows that this structure has $C = 0.4$. This value, that incidentally coincides to what found for the silica samples, must therefore be considered as the “zero” in the crystallinity scale.

A.4 Results and discussion

Next, I observed how the atomic structure of an a-C monolayer region changes during continuous irradiation in the STEM at 60 kV. Fig. A.5a shows eight selected frames taken from a MAADF series acquired over ∼18 minutes. A four-pixel Gaussian blur filter was used here to reduce the noise. Frame 1 shows the initial structure: most of the atoms are randomly arranged while only a minority of them form a small graphene-like crystallite (indicated by the yellow dashed circle). In the following frames the atoms gradually rearrange and the initial crystallite grows in dimension. Finally, in frame 8, most of the atoms indicated by the yellow dashed circle have arranged to form a relatively large crystallite. Interestingly, an other smaller crystallite has also appeared (orange dashed circle) and a grain boundary is forming between the two domains (indicated approximately by the two blue arrows). This trend is confirmed by the graph of fig. A.5b, which plots the crystallinity as a function of electron dose and irradiation time. The crystallinity increases from ∼0.5 to almost 0.8. Such a high value of crystallinity is never observed for the as-grown a-C films, and it must be certainly ascribed to the prolonged exposure to the electron beam. At 60 kV graphene is known to be stable, both in TEM [102] and in STEM [61]. On the contrary, the frame series of fig. A.5a clearly proves that 2D a-C monolayers are not. Therefore, it is reasonable to imagine that the structure receives enough energy from the impinging electron beam to move around atoms (but not to eject them) and to rotate bonds, continuously changing the local topology of the system. This process continues until, by coincidence, some atoms happen to arrange in a hexagonal lattice, possibly contributing to the growth of an existing crystallite. At this point, the atoms are locked into the crystalline structure, which, as mentioned, is stable at 60 kV and therefore does not change anymore. The process can be seen as a combination of two mechanisms: a random rearrangement of atoms between metastable amorphous states and a "freezing" event in which the total energy of the system is lowered. The latter gives directionality to the process, driving the system to an increasingly crystalline structure. Note that the role of the electron beam is of crucial importance here, as it provides the energy needed to change the topology of the structure.

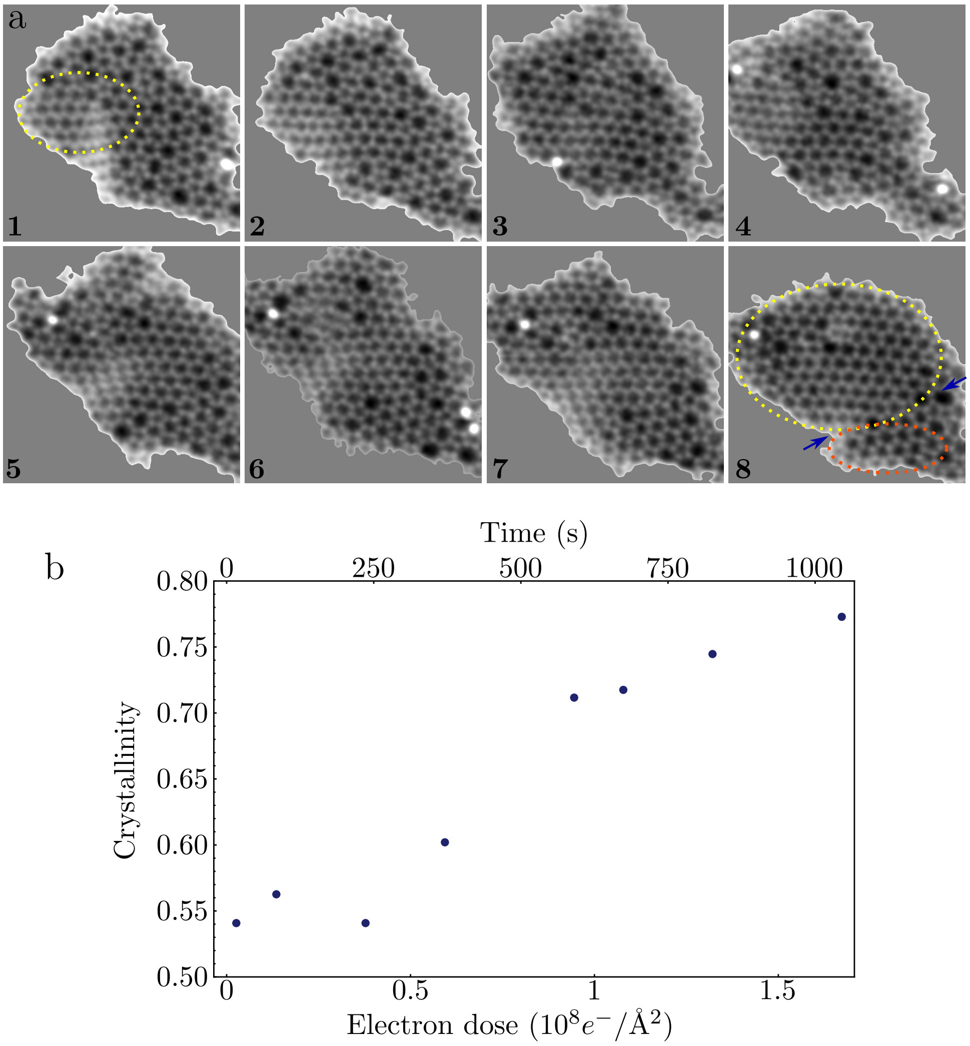

Figure A.5: (a) Eight frames from a MAADF series showing the structural modifications of an a-C monolayer region during electron beam irradiation. The yellow dashed ovals in frame 1 and 8 indicate the approximate dimensions of a crystallite of graphene embedded in the amorphous network at the beginning and at the end of the experiment, respectively. The orange dashed oval in frame 8 shows an additional smaller graphene crystallite that has formed. The blue arrows mark the position of the grain boundary separating the two domains. All FOVs are $4 \times 4\,\text{nm}^2$. A four-pixel Gaussian filter was applied to the raw images. (b) Crystallinity of the structure shown in (a) plotted as a function of electron dose and time.

A.5 Conclusions and outlook

Over the last fifteen years scientific research on 2D materials has grown enormously. While almost the entire existing literature focuses on 2D crystals, there are only a few experimental studies on 2D amorphous structures [111–114]. 2D amorphous materials are unique systems to study the structural and chemical properties at the atomic level. Determining the atomic structure of 3D amorphous materials is an extremely challenging task, if possible at all, since the commonly used microscopy techniques are either only sensitive to the very first atomic layers (e.g. STM) or they reveal the complex 2D projection of the structure (TEM, STEM). In two dimensions, the structure becomes accessible and the atomic positions can be determined in real space with high accuracy.

Among 2D amorphous materials, the 2D a-C films presented here are of particular interest because they can be considered as the amorphous counterpart of graphene. The properties of these films, such as electrical conductance, mechanical strength and stiffness, optical behavior and so on, can be tested against the analogous properties of graphene. This will allow to get an insight on whether these properties depend on the 2D carbon nature of the materials or rather on their degree of crystallinity. Also, in this work I have shown that the crystallinity of the a-C films can be increased in a controlled way by electron irradiation at 60 kV, while it can be decreased at 100 kV [111]. Combining these two results indicates that in principle it is possible to observe at the atomic level a continuous, reversible transition of a 2D carbon sheet between crystalline and amorphous states, by simply regulating the high voltage knob of the microscope.

List of publications

The following list includes all peer-reviewed scientific publications that I coauthored during the course of my Ph.D., ordered by publication date. My contributions are listed for each of them. For publications 1, 2 and 7 my contribution was crucial and it is elaborated in greater detail in the results chapter of this thesis.

1. **Unraveling the 3D Atomic Structure of a Suspended Graphene/hBN van der Waals Heterostructure**

   Giacomo Argentero, Andreas Mittelberger, Mohammad Reza Ahmadpour Monazam, Yang Cao, Timothy J. Pennycook, Clemens Mangler, Christian Kramberger, Jani Kotakoski, André K. Geim, Jannik C. Meyer

   Nano Letters, 17 (3), 1409–1416 (2017)

   Author contributions: G.A. carried out all TEM and STEM experiments, analyzed the data and wrote the manuscript. **G.A.** and A.M. performed the STEM simulations. M.R.A.M. computed the relaxed model. Y.C. fabricated the sample. C.K. wrote a program to automatize the data analysis. T.J.P. and C.M. supervised the STEM experiments. J.K., A.K.G. and J.C.M. actively supervised the work and guided the study. All authors contributed to the manuscript.

2. **Isotope analysis in the transmission electron microscope**

   Toma Susi, Christoph Hofer, **Giacomo Argentero**, Gregor L. Leuthner, Timothy J. Pennycook, Clemens Mangler, Jannik C. Meyer, Jani Kotakoski

   Nature Communications, 7, 13040 (2016)

   Author contributions: T.S. performed theoretical and statistical analyses and DFT simulations, participated in STEM experiments and their analysis, and drafted the manuscript. C.H. performed sample synthesis, and participated in STEM experiments, their analysis, and the Raman analysis. **G.A.** participated in sample synthesis and the Raman analysis. G.T.L. participated in STEM experiments and their analysis. C.M. and T.J.P. prepared special alignments for the STEM instrument with J.K., who supervised the theoretical and statistical analyses and STEM experiments. J.K. and J.C.M. conceived and supervised the study.

3. **Visualising the strain distribution in suspended two-dimensional materials under local deformation**

   Kenan Elibol, Bernhard C. Bayer, Stefan Hummel, Jani Kotakoski, **Giacomo Argentero**, Jannik C. Meyer

   Scientific Reports, 6, 28485 (2016)

   Author contributions: K.E., B.C.B. and J.C.M. conceived the study and wrote the paper. K.E. and B.C.B. performed experiments and undertook data analysis. S.H. contributed to the sample fabrication, J.K. and **G.A.** contributed to the data analysis. All authors discussed the results and commented on the manuscript.

4. **Potassium intercalated multiwalled carbon nanotubes**

   Julio C. Chacón-Torres, Sami Dzsaber, Sofía M. Vega-Daz, Johanna Akbarzadeh, Herwig Peterlik, Jani Kotakoski, **Giacomo Argentero**, Jannik C. Meyer, Thomas Pichler, Ferenc Simon, Mauricio Terrones, Stephanie Reich

   Carbon, 105, 90–95 (2016)

   Author contributions: Together with J.K. and J.C.M., **G.A** recorded and analyzed the TEM data. The other authors conducted the rest of the study.

5. **Size and Purity Control of HPHT Nanodiamonds down to 1 nm**

   Stepan Stehlik, Marian Varga, Martin Ledinsky, Vit Jirasek, Anna Artemenko, Halyna Kozak, Lukas Ondic, Viera Skakalova, **Giacomo Argentero**, Timothy Pennycook, Jannik C. Meyer, Antonin Fejfar, Alexander Kromka, Bohuslav Rezek

   The Journal of Physical Chemistry C, 119, 27708–27720 (2015)

   Author contributions: **G.A.** prepared the sample for the TEM study and, together with V.S., T.J.P. and J.C.M., acquired and interpreted the STEM data. The other authors conducted the rest of the study.

6. **Dimensional crossover in the quantum transport behaviour of the natural topological insulator Aleksite**

   Pascal Gehring, Kristina Vaklinova, Alexander Hoyer, Hadj M. Benia, Viera Skakalova, **Giacomo Argentero**, Franz Eder, Jannik C. Meyer, Marko Burghard, Klaus Kern

   Scientific Reports, 5, 11691 (2015)

   Author contributions: P.G. and M.B. designed the experiments. P.G., K.V. and A.H. performed the magnetotransport, AFM and Raman measurements, and evaluated the corresponding data. H.M.B. carried out the ARPES experiments and analyzed the data. The TEM data were collected and interpreted by V.S., **G.A.**, F.E. and J.C.M. M.B. and K.K. supervised the project. The manuscript was written by P.G. and M.B., who obtained input from all other authors.

7. **Towards weighing individual atoms by high-angle scattering of electrons**

   Giacomo Argentero, Clemens Mangler, Jani Kotakoski, Franz Eder, Jannik C. Meyer

   Ultramicroscopy, 151, 23–30 (2015)

   Author contributions: G.A., J.K., F.E. and J.C.M. developed the theory for electron-nucleus interaction. **G.A.** performed the calculations and simulated the EELS spectra and, together with J.C.M., wrote the manuscript. C.M. and J.C.M. performed the STEM experiments. J.C.M. conceived and supervised the study.

Submitted:

- **Atomic structure of intrinsic and electron-irradiation-induced defects in $MoTe_2$**

  Kenan Elibol, **Giacomo Argentero**, Toma Susi, Mohammad Reza Ahmadpour Monazam, Timothy J. Pennycook, Jannik C. Meyer, Jani Kotakoski

In preparation:

- **Synthesis and characterization of two-dimensional amorphous carbon films**

Contributions to scientific events

Participation in international conferences:

Date & Venue	**Conference**	**Type**	**Title of contribution**
June 24–28, 2013 Helsinky, Finland	NT13 Science and Applications of Nanotubes and Low-dimensional Materials	-	-
March 8–15, 2014 Kirchberg, Austria	XXVIIIth Int. Winterschool on Electronic Properties of Novel Materials	Poster	Dark field TEM imaging of grains in graphene flakes
July 4–7, 2014 Daresbury, UK	Advanced Topics in Aberration-Corrected STEM (Summer School)	Poster	STEM on graphene
April 19–23, 2015 Kasteel Vaalsbroek, The Netherlands	PICO 2015 3rd Conference on Frontiers of Aberration Corrected Electron Microscopy	Poster	Towards weighing individual atoms by high-angle scattering of electrons
April 19–22, 2016 Genoa, Italy	Graphene 2016	Poster	Analysis of graphene-hBN heterostructures by high-resolution scanning transmission electron microscopy with direction-sensitive detection of scattered electrons
August 7–13, 2016 Vienna, Austria	NT16 Science and Applications of Nanotubes and Low-dimensional Materials	Oral	Analysis of graphene-hBN heterostructures by high-resolution scanning transmission electron microscopy with direction-sensitive detection of scattered electrons
March 04–11, 2017 Kirchberg, Austria	XXXIst Int. Winterschool on Electronic Properties of Novel Materials	Poster	Unraveling the 3D atomic structure of a suspended graphene/hBN vdW heterostructure
June 25–30, 2017 Belo Horizonte, Brazil	NT17 Science and Applications of Nanotubes and Low-dimensional Materials	Oral	Synthesis and characterization of two-dimensional amorphous carbon films

Other oral presentations:

- May 2, 2013. Seminar ”Micro- and Nanomaterials”, Vienna:
  ”Scanning Tunneling Microscopy Study of the Fe3O4(001) Surface”
- June 1, 2016. Seminar ”Micro- and Nanomaterials”, Vienna:
  ”Analysis of Graphene/hBN Heterostructures”
- June 30, 2016. Highlight Lecture at the Faculty Open Presentations, Vienna:
  ”Analysis of Graphene/hBN Heterostructures: a TEM/STEM study”

Bibliography

1. Peierls, R. Quelques proprits typiques des corps solides. fre. *Annales de l'institut Henri Poincar* **5,** 177–222 (1935).
2. Landau, L. D. Zur Theorie der phasenumwandlungen II. *Phys. Z. Sowjetunion* **11,** 26–35 (1937).
3. Geim, A. K. & Novoselov, K. S. The rise of graphene. *Nature materials* **6,** 183–191 (2007).
4. ScienceWatch. *Interview with Konstantin Novoselov* - Last visited on 2017-07-26. <`http://archive.sciencewatch.com/ana/st/graphene/09febSTGraNovo/`> (2009).
5. GrapheneFlagship. *In conversation with Prof Sir Kostya Novoselov at The University of Manchester, UK* - Last visited on 2017-07-26. <`http://www.graphene.manchester.ac.uk/discover/video-gallery/interviews-and-lectures/kostya-novoselov-interview/`> (2015).
6. Novoselov, K. S. *et al.* Electric field effect in atomically thin carbon films. *Science* **306,** 666–669 (2004).
7. Geim, A. K. Nobel Lecture: Random walk to graphene. *Rev. Mod. Phys.* **83,** 851–862 (2011).
8. *The Royal Swedish Academy of Science: Press Release* <`http://www.nobelprize.org/nobel_prizes/physics/laureates/2010/press.html`> (2010).
9. Novoselov, K. S. *et al.* Two-dimensional atomic crystals. *Proceedings Of The National Academy Of Sciences Of The United States Of America* **102,** 10451–10453 (2005).
10. Lalmi, B. *et al.* Epitaxial growth of a silicene sheet. *Applied Physics Letters* **97,** 223109 (2010).
11. Dávila, M. E., Xian, L., Cahangirov, S., Rubio, A. & Le Lay, G. Germanene: A novel two-dimensional germanium allotrope akin to graphene and silicene. *New Journal of Physics* **16,** 095002 (2014).
12. Li, L. *et al.* Black Phosphorus Field-effect Transistors Black phosphorus field-effect transistors. *Nature Nanotechnology* **9,** 1–17 (2014).

13. Geim, A. K. & Grigorieva, I. V. Van der Waals heterostructures. *Nature* **499,** 419–425 (2013).
14. Geim, A. K. Graphene: status and prospects. *Science* **324,** 1530–1534 (2009).
15. Wallace, P. R. The band theory of graphite. *Physical Review* **71,** 622 (1947).
16. Castro Neto, A. H., Guinea, F., Peres, N. M. R., Novoselov, K. S. & Geim, A. K. The electronic properties of graphene. *Rev. Mod. Phys* **81,** 109 (2009).
17. Bolotin, K. I. *et al.* Ultrahigh electron mobility in suspended graphene. *Solid State Communications* **146,** 351–355 (2008).
18. Novoselov, K. S. *et al.* Two-dimensional gas of massless Dirac fermions in graphene. *Nature* **438,** 197–200 (2005).
19. Balandin, A. a. *et al.* Superior Thermal Conductivity of Single-Layer Graphene. *Nano Letters* **8,** 902–907 (2008).
20. Lee, C., Wei, X., Kysar, J. W. & Hone, J. Measurement of the elastic properties and intrinsic strength of monolayer graphene. *Science* **321,** 385–388 (2008).
21. Massicotte, M *et al.* Picosecond photoresponse in van der Waals heterostructures. *Nature nanotechnology* **11,** 1–6 (2015).
22. Huang, P. Y., Meyer, J. C. & Muller, D. a. From atoms to grains: Transmission electron microscopy of graphene. *MRS Bulletin* **37,** 1214–1221 (2012).
23. Robertson, A. W. & Warner, J. H. Atomic resolution imaging of graphene by transmission electron microscopy. *Nanoscale* **5,** 4079–93 (2013).
24. Bachmatiuk, A. *et al.* Low Voltage Transmission Electron Microscopy of Graphene. *Small* **11,** 515–542 (2015).
25. Idrobo, J. C. & Zhou, W. A short story of imaging and spectroscopy of two-dimensional materials by scanning transmission electron microscopy. *Ultramicroscopy* **180.** Ondrej Krivanek: A research life in EELS and aberration corrected STEM, 156 –162 (2017).
26. Meyer, J. C. *et al.* The structure of suspended graphene sheets. *Nature* **446,** 60–63 (2007).
27. Thomson, J. J. XL. Cathode Rays. *Philosophical Magazine Series 5* **44,** 293–316 (1897).
28. De Broglie, L. Recherches sur la thorie des Quanta. *PhD Thesis* (1924).
29. Scherzer, O. Über einige Fehler von Elektronenlinsen. *Zeitschrift für Physik* **101,** 593–603 (1936).

30. Scherzer, O. Sphärische und chromatische Korrektur von Elektronen-Linsen. *Optik* **2,** 114–132 (1947).
31. Haider, M *et al.* Electron microscopy image enhanced. *Nature* **392,** 768–769 (1998).
32. Krivanek, O., Delby, N., Spence, A., Camps, R. & Brown, L. Aberration correction in the STEM. *Inst. Phys. Conf. Ser. 153 (Proceedings EMAG meeting, Cambridge 1997),* 35–40 (1997).
33. Lin, Y. C., Teng, P. Y., Chiu, P. W. & Suenaga, K. Exploring the Single Atom Spin State by Electron Spectroscopy. *Physical Review Letters* **115,** 1–5 (2015).
34. Tan, H., Turner, S., Yücelen, E., Verbeeck, J. & Van Tendeloo, G. 2D Atomic Mapping of Oxidation States in Transition Metal Oxides by Scanning Transmission Electron Microscopy and Electron Energy-Loss Spectroscopy. *Physical Review Letters* **107,** 107602 (2011).
35. Ramasse, Q. M. *et al.* Probing the Bonding and Electronic Structure of Single Atom Dopants in Graphene with Electron Energy Loss Spectroscopy. *Nano letters* **13,** 4989–4995 (2013).
36. Krivanek, O. L. *et al.* An electron microscope for the aberration-corrected era. *Ultramicroscopy* **108,** 179–195 (2008).
37. Krivanek, O. L. *et al.* Atom-by-atom structural and chemical analysis by annular dark-field electron microscopy. *Nature* **464,** 571–574 (2010).
38. Blake, P *et al.* Making graphene visible. *Applied Physics Letters* **91,** 63124 (2007).
39. Bae, S. *et al.* Roll-to-roll production of 30-inch graphene films for transparent electrodes. *Nature Nanotechnology* **5,** 574–578 (2010).
40. Xiao, X., Li, Y. & Liu, Z. Graphene Commercialization. *Nature Materials* **15,** 697–698 (2016).
41. Ferrari, A. C. *et al.* Science and technology roadmap for graphene, related two-dimensional crystals, and hybrid systems. *Nanoscale* **7,** 4598–4810 (2015).
42. Meyer, J. C., Girit, C. O., Crommie, M. F. & Zettl, A. Hydrocarbon lithography on graphene membranes. *Applied Physics Letters* **92,** 123110 (2008).
43. Regan, W. *et al.* A direct transfer of layer-area graphene. *Applied Physics Letters* **96,** 113102 (2010).
44. Ophus, C., Ercius, P., Sarahan, M., Czarnik, C. & Ciston, J. Recording and Using 4D-STEM Datasets in Materials Science. *Microscopy and Microanalysis* **20,** 6263 (2014).

45. Jesse, S. *et al.* Big Data Analytics for Scanning Transmission Electron Microscopy Ptychography. *Scientific Reports* **6,** 26348 (2016).

46. Pennycook, T. J. *et al.* Efficient phase contrast imaging in STEM using a pixelated detector. Part 1: Experimental demonstration at atomic resolution. *Ultramicroscopy* **151,** 160–167 (2015).

47. Nellist, P. & Rodenburg, J. Beyond the conventional information limit: the relevant coherence function. *Ultramicroscopy* **54,** 61–74 (1994).

48. Rodenburg, J., McCallum, B. & Nellist, P. Experimental tests on double-resolution coherent imaging via STEM. *Ultramicroscopy* **48,** 304–314 (1993).

49. Dekkers, N. H. & de Lang, H. Differential phase contrast in a STEM. *Optik* **4,** 452–456 (1974).

50. Chapman, J., Batson, P., Waddell, E. & Ferrier, R. The direct determination of magnetic domain wall profiles by differential phase contrast electron microscopy. *Ultramicroscopy* **3,** 203 –214 (1978).

51. Rose, H. Nonstandard imaging methods in electron microscopy. *Ultramicroscopy* **2,** 251–267 (1976).

52. Chapman, J. N., McFadyen, I. R. & McVitie, S. Modified differential phase contrast Lorentz microscopy for improved imaging of magnetic structures. *IEEE Transactions on Magnetics* **26,** 1506–1511 (1990).

53. Tate, M. W. *et al.* High Dynamic Range Pixel Array Detector for Scanning Transmission Electron Microscopy. *Microscopy and Microanalysis* **22,** 237249 (2016).

54. Koch, C. Determination of core structure periodicity and point defect density along dislocations. *PhD thesis* (2002).

55. Dean, C. R. *et al.* Boron nitride substrates for high-quality graphene electronics. *Nature nanotechnology* **5,** 722–726 (2010).

56. Decker, R. *et al.* Local electronic properties of graphene on a BN substrate via scanning tunneling microscopy. *Nano letters* **11,** 2291–2295 (2011).

57. Xue, J. *et al.* Scanning tunnelling microscopy and spectroscopy of ultra-flat graphene on hexagonal boron nitride. *Nature materials* **10,** 282–285 (2011).

58. Gannett, W *et al.* Boron nitride substrates for high mobility chemical vapor deposited graphene. *Applied Physics Letters* **98,** 242105 (2011).

59. Kim, E., Yu, T., Song, E. S. & Yu, B. Chemical vapor deposition-assembled graphene field-effect transistor on hexagonal boron nitride. *Applied Physics Letters* **98,** 262103 (2011).

60. Woods, C. R. *et al.* Commensurate-incommensurate transition in graphene on hexagonal boron nitride. *Nature Physics* **10,** 451–456 (2014).
61. Susi, T. *et al.* Isotope analysis in the transmission electron microscope. *Nature Communications* **7,** 13040 (2016).
62. Kretinin, A. V. *et al.* Electronic properties of graphene encapsulated with different two-dimensional atomic crystals. *Nano Letters* **14,** 3270–3276 (2014).
63. Longchamp, J.-N., Escher, C. & Fink, H.-W. Ultraclean freestanding graphene by platinum-metal catalysis. *Journal of Vacuum Science & Technology B: Microelectronics and Nanometer Structures* **31,** 020605 (2013).
64. Meyer, J. C. *et al.* On the roughness of single- and bi-layer graphene membranes. *Solid State Communications* **143,** 101–109 (2007).
65. Yankowitz, M. *et al.* Emergence of superlattice Dirac points in graphene on hexagonal boron nitride. *Nature Physics* **8,** 382–386 (2012).
66. Tang, S. *et al.* Precisely aligned graphene grown on hexagonal boron nitride by catalyst free chemical vapor deposition. *Scientific reports* **3,** 2666 (2013).
67. Wang, D. *et al.* Thermally Induced Graphene Rotation on Hexagonal Boron Nitride. *Physical Review Letters* **116,** 126101 (2016).
68. Hermann, K. Periodic overlayers and moiré patterns: theoretical studies of geometric properties. *Journal of Physics: Condensed Matter* **24,** 314210 (2012).
69. Haigh, S. J. *et al.* Cross-sectional imaging of individual layers and buried interfaces of graphene-based heterostructures and superlattices. *Nature Materials* **11,** 9–12 (2012).
70. Pennycook, S. J. & Nellist, P. D. *Scanning Transmission Electron Microscopy: Imaging and Analysis* (Springer, 2011).
71. Zhou, S., Han, J., Dai, S., Sun, J. & Srolovitz, D. J. Van der Waals bilayer energetics: Generalized stacking-fault energy of graphene, boron nitride, and graphene/boron nitride bilayers. *Physical Review B* **92,** 155438 (2015).
72. Klimes, J., Bowler, D. R. & Michaelides, A. Van der Waals density functionals applied to solids. *Physical Review B* **83,** 195131 (2011).
73. Thonhauser, T *et al.* Van der Waals density functional: Self-consistent potential and the nature of the van der Waals bond. *Physical Review B* **76,** 125112 (2007).
74. Sachs, B., Wehling, T. O., Katsnelson, M. I. & Lichtenstein, A. I. Adhesion and electronic structure of graphene on hexagonal boron nitride substrates. *Physical Review B* **84,** 195414 (2011).

75. Los, J. H. & Fasolino, a. Intrinsic long-range bond-order potential for carbon: Performance in Monte Carlo simulations of graphitization. *Physical Review B* **68,** 24107 (2003).

76. Tersoff, J. New empirical approach for the structure and energy of covalent systems. *Physical Review B* **37,** 12 (1988).

77. Tersoff, J. Modeling solid-state chemistry: Interatomic potentials for multicomponent systems. *Physical Review B* **39,** 8 (1989).

78. Plimpton, S. Fast Parallel Algorithms for Short-Range Molecular Dynamics. *Journ. Comp. Phys.* **117,** 1–19 (1995).

79. Plimpton, S. J. & Thompson, A. P. Computational aspects of many-body potentials. *MRS Bulletin* **37,** 513–521 (2012).

80. Leven, I., Maaravi, T., Azuri, I., Kronik, L. & Hod, O. Interlayer Potential for Graphene/h-BN Heterostructures. *Journal of Chemical Theory and Computation* **12,** 2896–2905 (2016).

81. Cai, W. *et al.* Synthesis and solid-state NMR structural characterization of ^{13}C-labeled graphite oxide. *Science* **321,** 1815–1817 (2008).

82. Li, X., Cai, W., Colombo, L. & Ruoff, R. S. Evolution of graphene growth on Ni and Cu by carbon isotope labeling. *Nano letters* **9,** 4268–4272 (2009).

83. Li, Z. *et al.* Low-temperature growth of graphene by chemical vapor deposition using solid and liquid carbon sources. *ACS nano* **5,** 3385–3390 (2011).

84. Vos, M. Observing atom motion by electron-atom Compton scattering. *Physical Review A* **65,** 1–5 (2001).

85. Sinnemann, T., Job, R. & Rosenberg, M. Reduction of the zero-phonon ^{57}Fe Mössbauer fraction just above T_c in the $(\mathrm{Bi,Pb})_2\mathrm{Sr_2Ca_2Cu_3O_{10}}$ superconductor. *Phys. Rev. B* **45,** 4941–4944 (1992).

86. Boothroyd, C. B. Why don't high-resolution simulations and images match? *Journal of Microscopy* **190,** 99–108 (1998).

87. Kittel. *Introduction to Solid State Physics* (Wiley, 2007).

88. Tewary, V & Yang, B. Singular behavior of the Debye-Waller factor of graphene. *Physical Review B* **79,** 125416 (2009).

89. Wei, Y, Wang, R & Wang, W. Soft phonons and phase transition in amorphous carbon. *Physical Review B* **72,** 12203 (2005).

90. Went, M. R. & Vos, M. Rutherford backscattering using electrons as projectiles: Underlying principles and possible applications. *Nuclear Instruments and Methods in Physics Research Section B: Beam Interactions with Materials and Atoms* **266,** 998–1011 (2008).

91. Cooper, G, Hitchcock, A & Chatzidimitriou-Dreismann, C. Anomalous Quasielastic Electron Scattering from Single H2, D2, and HD Molecules at Large Momentum Transfer: Indications of Nuclear Spin Effects. *Physical Review Letters* **100,** 43204 (2008).

92. Vos, M & Went, M. R. Elastic electron scattering from hydrogen molecules at high-momentum transfer. *Journal of Physics B: Atomic, Molecular and Optical Physics* **42,** 65204 (2009).

93. Lovejoy, T. *et al.* Energy-Filtered High-Angle Dark Field Mapping of Ultra-Light Elements. *Microscopy and Microanalysis* **20,** 558–559 (2014).

94. Taylor, J. R. *An Introduction to Error Analysis: The Study of Uncertainties in Physical Measurements* 327 (University Science Books, 1997).

95. Egerton, R. F., McLeod, R, Wang, F & Malac, M. Basic questions related to electron-induced sputtering in the TEM. *Ultramicroscopy* **110,** 991–997 (2010).

96. Kaiser, U *et al.* Transmission electron microscopy at 20kV for imaging and spectroscopy. *Ultramicroscopy* **111,** 1239–1246 (2011).

97. Rose, H. H. Future trends in aberration-corrected electron microscopy. *Philosophical Transactions of the Royal Society of London A: Mathematical, Physical and Engineering Sciences* **367,** 3809–3823 (2009).

98. Uhlemann, S & Rose, H. Acceptance of imaging energy filters. *Ultramicroscopy* **63,** 161–167 (1996).

99. Frank, O, Kavan, L & Kalbac, M. Carbon isotope labelling in graphene research. *Nanoscale* **6,** 6363–6370 (2014).

100. Whiteway, E., Yang, W., Yu, V. & Hilke, M. Time evolution of the growth of single graphene crystals and high resolution isotope labeling. *Carbon* **111,** 173–181 (2017).

101. Krivanek, O. L. *et al.* Vibrational spectroscopy in the electron microscope. *Nature* **514,** 209–212 (2014).

102. Meyer, J. C. *et al.* Accurate Measurement of Electron Beam Induced Displacement Cross Sections for Single-Layer Graphene. *Physical Review Letters* **108,** 196102 (2012).

103. McKinley, W & Feshbach, H. The Coulomb Scattering of Relativistic Electrons by Nuclei. *Physical Review* **74,** 1759–1763 (1948).

104. Liu, L. *et al.* Heteroepitaxial Growth of Two-Dimensional Hexagonal Boron Nitride Templated by Graphene Edges. *Science* **343,** 163–167 (2014).

105. Isaacson, M, Ohtsuki, M & Utlaut, M. Can we determine the structure of thin amorphous film using scanning transmission electron microscopy? *Proceeding of the 37th Annual EMSA Meeting,* 498 (1979).

106. Isaacson, M. S. Seeing single atoms. *Ultramicroscopy* **123,** 3–12 (2012).

107. Aboav, D. A. Arrangement of grains in a polycristal. *Metallography* **13,** 383–390 (1970).

108. Aboav, D. A. The Arrangement of Cells in a Net. II. *Metallography* **16,** 265–273 (1983).

109. Buechner, C. *et al.* Building block analysis of 2D amorphous networks reveals medium range correlation. *Journal of Non-Crystalline Solids* **435,** 40–47 (2016).

110. Buechner, C. *et al.* Topological investigation of two-dimensional amorphous materials. *Zeitschrift fur Physikalische Chemie* **228,** 587–607 (2014).

111. Eder, F. R., Kotakoski, J., Kaiser, U. & Meyer, J. C. A journey from order to disorder - atom by atom transformation from graphene to a 2D carbon glass. *Scientific reports* **4,** 4060 (2014).

112. Lichtenstein, L *et al.* The atomic structure of a metal-supported vitreous thin silica film. *Angewandte Chemie (International ed. in English)* **51,** 404–407 (2012).

113. Huang, P. Y. *et al.* Direct Imaging of a Two-Dimensional Silica Glass on Graphene. *Nano Letters* **12,** 1081–1086 (2012).

114. Kotakoski, J. *et al.* Toward Two-Dimensional All-Carbon Heterostructures via Ion Beam Patterning of Single-Layer Graphene. *Nano Letters* **15,** 5944–5949 (2015).

115. Zachariasen, W. H. The Atomic Arrangement in Glass. *Journ. Am. Chem. Soc* **54,** 3841–3851 (1932).

116. Shackelford, J & Brown, B. D. The Lognormal Distribution in the Random Network Structure. *Journal of Non-Crystalline Solids* **44,** 379–382 (1981).